Modeling of Eddy Current Separation

Selahattin Baris Yazgan

Dissertation submitted to the faculty of the Virginia Polytechnic Institute and State University in partial fulfillment of the requirements for the degree of

Doctor of Philosophy
In
Mining Engineering

Gerald H. Luttrell
Roe-Hoan Yoon
Michael J. Mankosa
Gregory T. Adel
Nino S. Ripepi

12/14/2017
Blacksburg, VA

Keywords: Recycling, Eddy Current Separation, Magnetic Force, Dynamic Force Balance, Modeling

Modeling of Eddy Current Separation

Selahattin Baris Yazgan

ABSTRACT

Eddy current separation aims to recover non-ferrous metals from non-metals utilizing electromagnetic interactions. In order to describe the separation process, a representative model is needed that can accurately calculate the induced forces. Such a model can be used to optimize the efficiency of current equipment as well as designing ones that can offer new capabilities. Models proposed so far for the separation process, using traditional approaches to calculate forces, had limited success due to complex nature of electromagnetic interactions.

In this dissertation, a novel method for calculating the magnetic force acting on non-ferrous metal particles was developed. By this method, force calculations can be carried out accurately using intrinsic parameters of particles such as size and shape, as well as its orientation within the field. The method also takes into account the operating parameters of the equipment such as the rotational speed of the magnetic element and the speed of the belt. In order to verify this method and collect empirical data, a novel data acquisition and interpretation approach was developed.

A computer simulator was also developed that can calculate trajectories of particles based on operating parameters of the eddy current separator and characteristics of the material being processed. The accuracy of the simulator was verified using empirical data obtained by the novel data acquisition method.

This contribution provides a viable option for reducing the cost of analyzing; optimizing and designing eddy current separators.

Modeling of Eddy Current Separation

Selahattin Baris Yazgan

GENERAL AUDIENCE ABSTRACT

As technological advances in chemistry, material science, engineering and manufacturing lead to building of items with smaller parts and complex components, recycling them is becoming more challenging. Production of raw materials, especially metals, from fresh ores in mining has become a challenge due to rising costs and depletion of high grade deposits. Thus, in order to sustain growth of the economy and advances in technology, recycling is of utmost importance.

Iron and iron containing metal alloys such as steel can easily be separated with magnets. In order to separate metals that do not contain iron, such as aluminum, copper, brass, lead and zinc, eddy current separators are used.

Until now, it was not possible to define the separation process as a whole fundamentally based on the characteristics of particles and operating parameters of eddy current separators. In this research, new methods to analyze the separation process as well as a new technique to calculate the magnetic force acting on metal particles were developed. These will provide great help to optimize current equipment and raise the efficiencies of operations and at the same time serve as a tool to design new and better equipment to increase overall recycling performance.

Dedication

This work is dedicated to all, who has endured the painful process of creating something new and to all the heroes, who sacrificed their lives to provide the safe environment for such creations…

Acknowledgements

I would like to express my sincere gratitude and appreciation to Dr. Gerald Luttrell, Dr. Roe-Hoan Yoon and Dr. Michael J. Mankosa for all the help and guidance they have provided me during my studies. It has been a great honor to be a part of their excellent research team. With his excellent crash-course in VBA, help of Dr. Aaron Noble is much appreciated. I also would like to thank Dr. Gregory T. Adel and Dr. Nino Ripepi for serving in my committee.

I am deeply indebted to Mr. Richard Merwin and Mr. Tim Shuttleworth for their keen interest, trusting support and for their kind permission to benefit from their resources and facilities for my research activities.

I cannot thank Mr. Mike Ross enough for providing me with the tools, putting up with my crazy ideas and sharing his experiences in the vast field of electromagnetics. His friendship is and will always be greatly appreciated.

The members of the outstanding team at Eriez Manufacturing's Wager Road Facility in Erie, PA deserve a special mention, especially Mr. Everett Hull, Mr. Jim Irons, Mr. Mike Shattuck and Mrs. Barbara Wright, who went out of their way to help me whenever I needed it.

I am grateful for the friendship and motivation provided by Mr. Eric Yan and Mr. Andrew Hobert whom I look forward to working with as a team.

I would like to thank my best friend Dr. Andrew Ferhat Yildirim for listening me talk about my struggles in my studies for countless hours, offering the best of his help, encouraging me to finish my studies up and proofreading my work.

Most important and above all, I want to thank my wife, Fatoş "Julie" Yazgan, whose unconditional love helped me the most in this challenging endeavor. Without her, none of this would have been possible at such short time.

TABLE OF CONTENTS

1. INTRODUCTION

General information about recycling and eddy current separation will be presented in this chapter. The aim of using eddy current separators in recycling will also be introduced. Finally, importance and objective of the research will be given.

1.1. Background

Recycling can be termed as resource recovery from scrap material. Mineral processing aims at upgrading the valuable material content recovered from a resource by employing physical separation techniques, which corresponds well with the aim of recycling. Thus, recycling can be viewed as an industry that can benefit from mineral processing approaches. However, implementing techniques akin to mineral processing to recycling comes with a challenge. This challenge lies in the fact that recycling requires methods to successfully separate different types of materials whereas in mineral processing the main focus is only on one material type, rock.

1.1.1. Recycling

Recycling became known to general public during World War II era during which, governments asked for the scrap materials like paper, cloth and metals in order keep up with the high demand of the war industry. Collected material was required urgently to be converted into bandages, vehicles, ammunition, etc.

Post World War II, increasing consumption levels and with the start of depletion of high grade ore deposits; rising concerns for environmental protection coupled with decreasing profit margins led entrepreneurs and researchers to look into new sources of raw materials that are satisfactory in both quality and quantity.

Once again, recycling became important. Companies started paying for valuable materials by the weight so offering customers some sort of compensation for the separation effort that they are undertaking in hand-picking and sorting through their own waste. However, these efforts were quite small, when compared to the valuable material discarded to waste dumps [1].

The need to process greater quantities of scrap called for specialized approaches to the problem. Funded primarily through U.S. Bureau of Mines, early techniques for valuables recovery employed mineral processing methods such as size reduction, screening for liberation, followed by air separation to create light and heavy fractions. The light fraction usually consisted of the type of materials like paper and wood whereas the heavy fraction included the metals. The ferrous metals were taken off the stream using magnets, remaining non-ferrous metals were sent to one or multiple stages of dense media separation.

The need for another separation technique other than the ones stated above was needed since the effectiveness of separation was hindered as selection property suffered lack of uniqueness [2]. Research focused on in this field by Vanderbilt University [3] showed promising results and companies started in investing to explore the eddy current separation phenomena further.

1.1.2. Eddy Currents

Although eddy currents or their associated effects are experienced every day, awareness of general public of this is seldom. Whenever going through a metal detector, buying a can of soda from a machine or simply flipping the electric switch one would be making use of eddy currents or combating their ill effects.

The discovery of the eddy currents date back to late 19th century, when most of the inventions in the field of electricity and magnetism were taking place. Researchers like Hans-Christian Oersted, André-Marie Ampère and Dominique-François Arago did pioneering work to open up a new field which can be termed as electromagnetism. It was Michael Faraday's persistent research that led to the discovery of the electromagnetic induction and started a revolution. Heinrich Lenz, during his studies observed induced currents and their relation to the source that generates them, this relation later on called as Lenz's Law, which will be explained in the proceeding sections. Following these scientific advances, James Clerk Maxwell was able to build the connection between magnetism and electricity in which he was able to explain all the relations with, now well-known, equations [4].

Although previously observed by some of the researchers named above in their studies, the discovery of eddy currents is credited to Lèon Foucault, thus, eddy currents are also called after him as Foucault Currents. Evident from the introduction part of his research article [5], Professor Hughes points to earlier observations made by Arago and Faraday, which he built upon to construct an induction balance that he used to identify metals, taking the first step in non-destructive testing of materials. This can be termed as the first application of eddy currents.

Eddy currents are small loops of currents that are created on, and to some extent, inside a conducting metal due to a change in magnetic flux; in other words magnetic field intensity. The source of the magnetic field could be either electricity or materials that are magnetized such as permanent magnets. If the source of the magnetic field is electricity then in order for eddy currents to be observed, the current should be changing like as in the case of alternating current.

As electricity itself has a magnetic field, eddy currents also form a magnetic field, when they are created. This field will oppose the magnetic field that creates eddy currents in accordance with Lenz's Law. This principle is used in metal detectors and in non-destructive testing. Since every metal has different internal resistance, the current density and thus the magnetic field produced will be different too. This property is used in identification of metals.

In the case of electricity distribution, eddy currents have a negative impact, causing losses in the form of heat. Various methods are employed to limit the formation of eddy currents to overcome this.

In medical imaging where magnets and/or magnetic fields are involved, eddy currents are also produced and they cause noise in images causing distortion, which are usually overcome by employing software to correct for it.

1.1.3. Use of Eddy Currents in Recycling

Recycling industry makes use of eddy currents, when removing non-ferrous metals from other materials is aimed. A typical flowsheet will start with a shredder to reduce the size of objects from cars to small pieces, which then are passed through very strong magnets to extract the

ferrous metals from the stream. This stream is then sent to *eddy current separators (ECS)* that employ permanent magnets that are spun at speeds in excess of 2000 rpm in order to generate an alternating magnetic field. This field is used to induce eddy currents on non-ferrous metals so that they are removed by ejection from the stream at the end of the belt conveyor. This way, a mixed concentrate of non-ferrous metals called Zorba is obtained. Zorba is an important input to the metal industry since it is both cheaper and environmentally friendly to recycle scrap.

The recovery and grade of the Zorba depends directly on the performance of the eddy current separators so it is very important to understand the operating parameters of this equipment. However, due to its complex nature of operation, it is not very easy to interpret results obtained by pure experimentation and thus a research in basic principles is needed to effectively simulate the process.

1.2. Eddy Current Separation Equipment Used Today

The types of machines that are employed in the recycling industry today are termed as rotary drum or pulley type eddy current separators. Rotary drum term came into use since permanent magnets are placed on a cylindrical shell (drum) that is rotated to create an oscillating magnetic field. The term pulley type is a result of placement of the magnetic element inside the end pulley of the belt conveyor used in the machine.

The belt conveyor used in the machine is driven by an electric motor at the pulley where material feeding takes place. Belt conveyor serves two main purposes. First and main purpose of the conveyor is to introduce the material to the oscillating magnetic field created by the magnetic element. Its second purpose is to keep the orientation of the particles similar; exposing their largest surface area to the magnetic field. The importance of the orientation will be discussed in next chapters.

Material fed onto the belt conveyor travels toward the magnetic field generated by the rotating permanent magnets. The magnets are placed on a cylindrical drum and this assembly (magnetic element) is then inserted into the pulley of the belt, which is usually made up of stainless steel or fiberglass. The placement of magnets is carried out in an alternating manner in order to obtain

favorable magnetic field density distributions. The magnetic element is rotated with an electric motor separate from the belt conveyor drive mechanism. If the magnetic magnetic element is overlapping totally with inside of the belt pulley, this is called a *concentric type* ECS whereas if the rotor is considerably smaller than the shell, it is called as an eccentric ECS. Better differentiation is possible by examining the Figure 1.

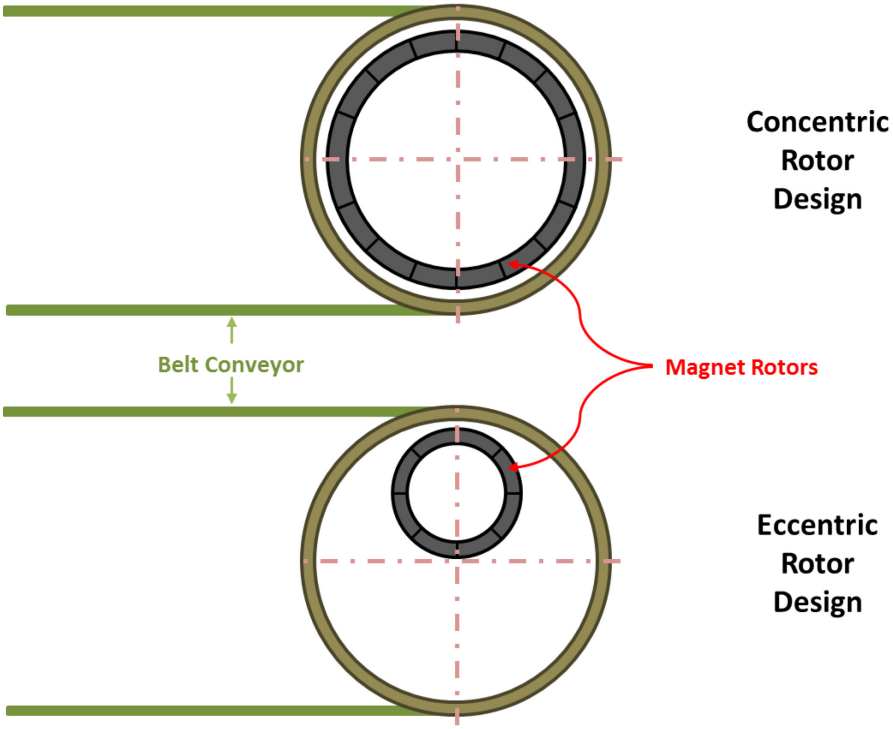

Figure 1. Illustrations showing different ECS rotor designs

During industrial operations a splitter is also used. Splitters are usually made up of location adjustable stainless steel plates or additional parts placed on them based on the type of separation. Position of the splitter plays an important role based on the trajectory differences of particles that need to be recovered from the stream. A splitter setting closer the magnetic rotor is practiced for weakly responding particles to increase recoveries. However, such increased recoveries result in loss of grade, quite similar to what one would observe in mineral processing operations.

1.3. Importance and Objective of the Research

The main objective of this work was to overcome the problem stated above by developing equations and novel techniques to successfully identify the role of each variable and their interactions with each other in the separation process quantitatively. Apart from this objective, another task was creating a simulator that can precisely predict the trajectories of particles based on their characteristics and operating parameters of the equipment.

Accomplishing these tasks will provide tools necessary to improve how existing equipment are operated so that higher efficiencies can be attained. Another positive contribution will be in the area of research and development as new designs can be tested without actually building the machines meaning savings can be realized in costs and time.

2. LITERATURE REVIEW

In this chapter, previous work on modeling of eddy current separators and the separation process will be examined. Although all of the researchers attempted to predict trajectories by modeling the motion of non-ferrous particles, the construction of equipment used in their model and experiments conducted are different from one researcher to another. This brings the limitation in reporting a collective work in terms of contributions since the nature of the problem changes from case to case as the characteristics of the magnetic field inducing eddy currents on the non-ferrous particles change. In addition, for one case, an electromagnet was used to create the changing magnetic field rather than permanent magnets. Thus, attempts made to model the trajectories for different equipment designs (or different approaches on the same design) will be handled separately in sub-sections in a chronological order.

2.1. Designs Prior to Rotary Drum

The earlier designs of eddy current separators are examined. While trying to model the process of separation, researchers used the method that treats particles as made up of loops of current. With this approximation, it was possible to predict the trajectories of particles with limited success in obtaining a general formula valid for all particle shapes and sizes.

2.1.1. Single Angled Slide

The first involved attempt to model the process for a separation equipment employing eddy currents induced by permanent magnet arrangements was carried out by Schloemann in 1975, in a series of two research articles[6],[7]. The theory behind the mechanism of separation is examined and given through a series of equations making use of the principles of electromagnetism. The equipment used for experiments is basically a slide that has permanent magnets arranged in alternating polarity on its sub-surface. Magnets are arranged at an angle of 45 degrees from the material flow direction. Material is fed to the system by gravity. The axis notation is taken as such: x-axis shows the slide surface parallel to material flow direction, y-axis again on the slide surface plane perpendicular to x-axis and z-axis perpendicular to the surface plane of the slide. This design is presented in Figure 2.

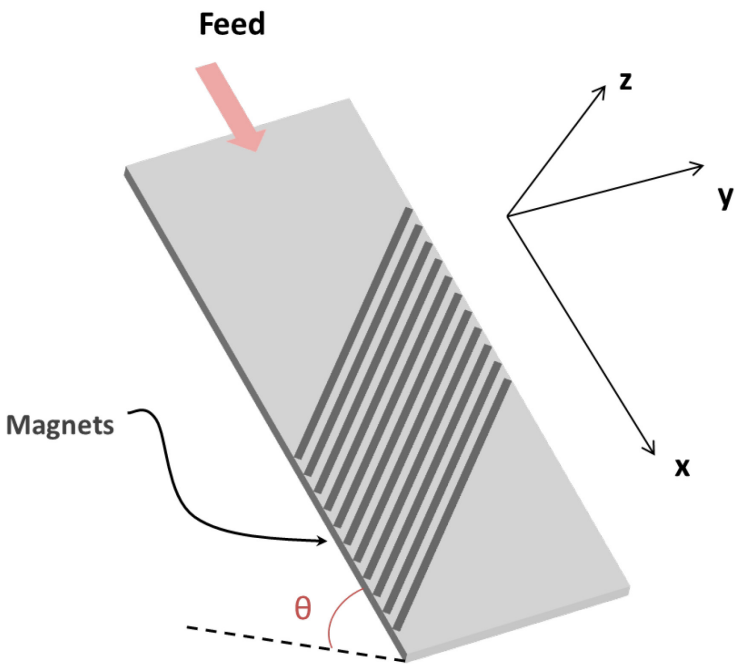

Figure 2. Eddy Current Separator design by Schloemann

The author starts with the simple case of a small thin ring, assuming it as a single loop, which carries the eddy current induced by the changing magnetic field; as the material passes the alternating poles of magnets. From force calculations, an equipment (magnetic field) and material (particle) specific term, α, is reached showing the importance of conductivity, size, mass density and the magnetic flux density given below:

$$\alpha = \frac{1}{4}\frac{\sigma}{\rho}r^2\left(\frac{\partial B_z}{\partial x}\right)^2$$

where σ is the conductivity, ρ is the mass density, r is the radius and B_z is the flux density.

The force, for the simplest case is thus:

$$F_y = m\alpha\vartheta_x$$

where F_y is the force that deflects particle in y-direction, m is the mass of the particle and ϑ_x is the velocity of the particle in x-direction. It should be noted here that this is the resultant force acting on the particle in y-direction.

Using geometric relations and ignoring the effect of friction, Schloemann derives a trajectory formula for a particle that slides down from rest, as follows:

$$y(x) = \frac{\sqrt{2}}{3}\frac{\alpha x^{3/2}}{(g\,sin\theta)^{1/2}}\left[\left(1-2\frac{x_o}{x}\right)\left(1+\frac{x_o}{x}\right)^{1/2}+2\left(\frac{x_o}{x}\right)^{3/2}\right]$$

Here, g is the gravitational acceleration; θ is the angle of the slide from the horizontal, x_o is the distance covered by the particle that reaches the velocity of ϑ_o starting from rest.

From the simple theory, Schloemann builds up to a more complex model by introducing the effect of friction as well as the geometry and size of particles. Calculations are carried out for a long-thin strip of metal as well as a thin disk, showing how the geometry plays an important role on the magnitude of parameters contributing to α term.

Also calculated is the magnetic flux density near the ramp surface so that the influence of the type of magnets (introduced in the form of Intensity of Magnetization) that are chosen is also taken into account. Magnetic flux density is defined as a period function represented by a Fourier series. Evaluated over x, the average flux density is given by:

$$\left\langle\left(\frac{\partial B_z}{\partial x}\right)^2\right\rangle = \frac{2{I_o}^2}{\lambda}\left(\frac{1}{\sinh(4\pi z/\lambda)}-\frac{2}{\sinh[4\pi\,(z+d)/\lambda]}+\frac{1}{\sinh[4\pi\,(z+2d)/\lambda]}\right)$$

where I_o is the intensity of magnetization of the magnets, d is the thickness of the magnets, z is the distance from the face of slide and λ is the period of magnet array. It is important to note that, the effect of backplate on the extent of magnetic field is taken into account with the last term by introducing $(z + 2d)$.

It is very important to note that during his derivations and calculations, Schloemann assumed that the particle size to be small, when compared to the magnet period (twice the magnet width) and that magnetic flux density is taken as an average value. Also to be noted is the fact that, due to the construction and working principle of the apparatus, the particles are bound to the x-y plane and are not lifted up from the surface so calculations are carried out in two dimensions.

Based on the derived equations, Schloemann reaches to the conclusion that deflection is proportional to the conductivity and mass density of the particle, intensity of magnetization of magnets and the inclination of the apparatus. It is also discussed in the closing part that air drag is not accounted for in the calculation for simplicity, but if taken into account at higher particle velocities where a pronounced effect is expected, will work against the deflective force due to eddy currents so that the trajectory reaches to a straight line.

Though mentioning the skin effect for the case of particles that have the thickness (during all his calculations, he assumed thin structures) he neglects its effect assuming that the change due to it would be negligible. However such generalization leads to the over estimation of currents produced, especially for bigger sizes of particles for which author mentions no success.

Another shortcoming is realized due to the approach taken to calculate the trajectory of the particle. In order to carry out such a calculation one needs to work with the resultant force. However, it is not possible to express the true characteristics of motion through a force field through a definition of resultant force omitting the varying characteristic of the magnetic field in the construction of the equipment.

2.1.2. Stacked Vertical Slide and Stacked Rotational Discs

Published in 1986, the article on the modeling of the separation process of an eddy current separator by Van der Valk et al. [8] shows the calculations for two different types of apparatus. Both of the separators are similar in the sense that they employed permanent magnets but show difference in their magnetic field setting (which is a closed setting), when compared to the work carried out by Schloemann in 1975.

The first equipment is very similar in construction to Schloemann's design of the permanent magnet slide with alternating polarities. However, this design introduced by Dalmijn et al.[9], adds a similar slide to the opposing side and tilt the whole setup to a vertical layout so that particles, theoretically, do not touch the surface of the walls but flow down the channel formed. This apparatus is called as Vertical Eddy Current Separator or VECS in short. The major axes are defined as x-axis being perpendicular to the long axis of magnets and tangent to their surfaces, y-axis being parallel to the boundary of each magnet and again tangent to the magnet surfaces and z-axis being perpendicular to the face of the magnets (walls). An illustration is given in Figure 3.

Second equipment is similar to first one in terms of material feeding into the channel formed by magnets facing each other with opposing poles but this time magnets are placed on discs that rotate simultaneously (Figure 4). This apparatus is called as Rotating Disc Separator or RDS in short.

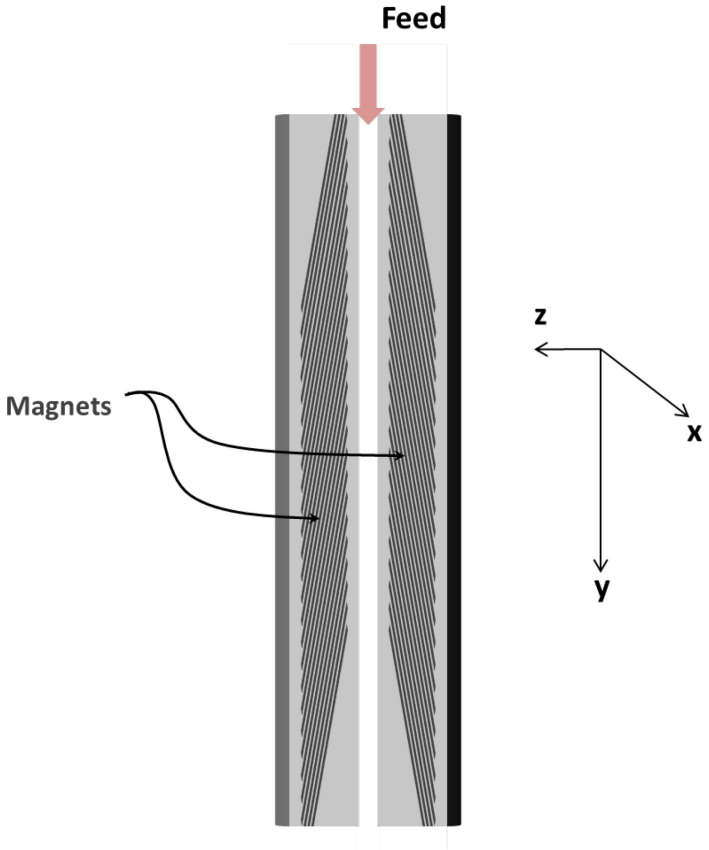

Figure 3. VECS designed by Dalmijn et al., used in calculations by Van der Valk et al.

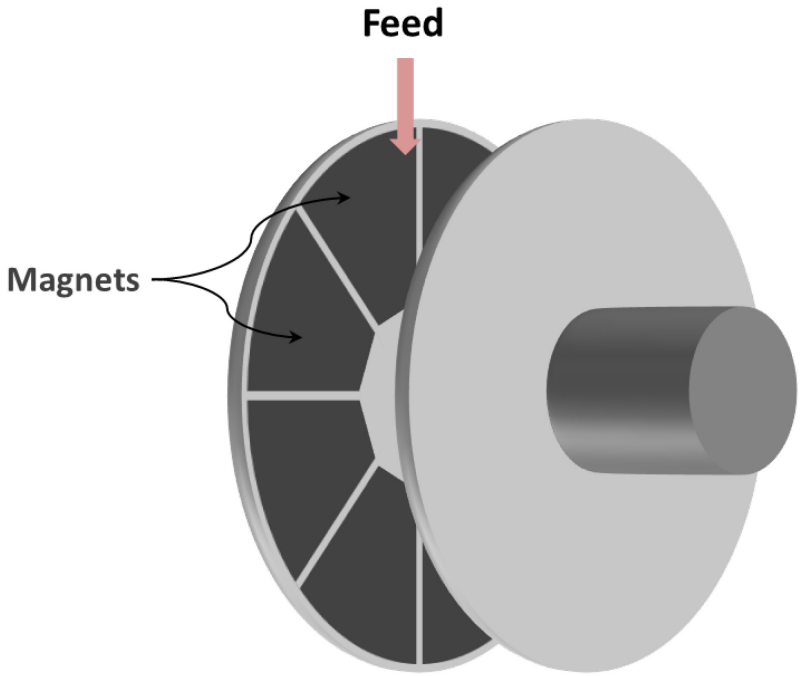

Figure 4. RDS designed by Van der Valk et al.

In order to find the magnetic flux density, Van der Valk et al. refers to the work done by Schloemann in 1975. Schloemann employed Fourier transforms and expanded them to define the corresponding flux density for a single axis since his case was a two dimensional problem. For the case considered here though, a three dimensional approach is needed.

For calculating the force that is observed by particles falling through the channel, assumption is made that particles are small with respect to the period of magnetization (which is twice the magnet width), block shaped and the edges are either parallel or perpendicular to the magnetic strips or walls. Employing the principle of Faraday's Induction and Maxwell's derivations, force is given as:

$$F_x = -m\alpha_{xx}\vartheta_x + m\alpha_{xz}\vartheta_z$$

$$F_z = m\alpha_{xz}\vartheta_x - m\alpha_{zz}\vartheta_z$$

$$F_y = 0$$

The reason behind having no force in y-direction is due to the fact that y-axis chosen to be the boundary between magnet strips. In the above equations, *m* is for the mass of the particle, *α*'s are for the damping coefficients and ϑ's for the velocity in the respective directions.
The damping coefficients α_{xx}, α_{xz} and α_{zz} are given by the following equations:

$$\alpha_{xx} = \frac{1}{2}\frac{\sigma}{\rho}\left\{a^2 D\left(\frac{a}{b}\right)\left(\frac{\partial B_z}{\partial x}\right)^2 + c^2 D\left(\frac{c}{b}\right)\left(\frac{\partial B_x}{\partial x}\right)^2\right\}$$

$$\alpha_{xz} = \frac{1}{2}\frac{\sigma}{\rho}\left\{a^2 D\left(\frac{a}{b}\right) - c^2 D\left(\frac{c}{b}\right)\right\}\frac{\partial B_x}{\partial x}\frac{\partial B_z}{\partial x}$$

$$\alpha_{zz} = \frac{1}{2}\frac{\sigma}{\rho}\left\{a^2 D\left(\frac{a}{b}\right)\left(\frac{\partial B_x}{\partial x}\right)^2 + c^2 D\left(\frac{c}{b}\right)\left(\frac{\partial B_z}{\partial x}\right)^2\right\}$$

Here, the function of *D(p)* is given as:

$$D(p) = \left(\frac{2}{\pi}\right)^4 \sum_{n=1}^{\infty} \sin^2\left(\frac{\pi n}{2}\right)\frac{1}{n^4}\left\{1 - \frac{2p}{\pi n}\tanh\left(\frac{\pi n}{2p}\right)\right\}$$

The variables for the above equations are *σ* is conductivity; *ρ* is the specific gravity, *a* is the edge dimension of particle in x-direction, *b* is the edge dimension in the y-direction, *c* is the edge dimension in z-direction, *p* is the ratio of the respective edges (so it is either *a/b* or *c/b*). These equations are valid for small values of *a* and *c*.

Van der Valk et al. derive a new dimensionless term, Quality Factor (Q) based on the assumption that contributions of force in the z-axis direction can be neglected for simplification since particles will have to be restricted to the walls of the channel. Thus, the only effective force is observed from the x-direction and the periodic average is taken as an approximation. It is should be noted that carrying out the calculations at center of the channel where *z = 0* during this

derivation, the intensity of magnetization term drops out since a symmetrical field is observed. This also requires no particle rotation, no collisions, no air drag and perfect feeding of material to the center of the channel. The equation for Q is given as:

$$Q = \left(\frac{4d_s}{\lambda}\right)^2 \sum_{m=1}^{\infty} \left[\frac{m}{\sinh\left\{\frac{2\pi}{\lambda}(md_w - 2d_m)\right\}} + \frac{m}{\sinh\left\{\frac{2\pi}{\lambda}(md_w + 2d_m)\right\}} - \frac{2m}{\sinh\left(\frac{2\pi}{\lambda} md_w\right)} \right]$$

where d_s is the channel gap width, d_w is the distance between walls, d_m is the thickness of the magnets and λ is the period of magnets or twice the width of magnets.

In order to calculate the trajectory, the authors calculate the deflection by repulsive forces. Adapting a new axis notation in which *k*-axis shows the direction of gravity pull and the *u*-axis shows the direction perpendicular to gravity (but parallel to walls), deflection Δu is given as:

$$\Delta u = \frac{1}{\beta^2} g \sin\phi \cos\phi \left\{\frac{1}{2}\beta^2 t^2 - \beta t + 1 - \exp(-\beta t)\right\} + \frac{1}{\beta}\left(\vartheta_{o_k} \cos\phi - \vartheta_{o_u} \sin\phi\right) \sin\phi \left\{\beta t - 1 + \exp(-\beta t)\right\}$$

where ϕ is the angle between the direction of gravity and the longitudinal side of magnets, t is the time and ϑ_{ok} and ϑ_{ou} are the initial velocities in k and u directions, respectively. Here the term β in fact stands for the average damping factor (α_{xx}) in the direction of gravity. In its expanded form:

$$\beta = \frac{1}{2}\frac{\sigma}{\rho} a^2 D \left(\frac{a}{b}\right) \left(\frac{I}{d_s}\right)^2 Q$$

For calculating the repulsive for in the Rotating Disc Separator (RDS), the factor derived, Q, is employed since it is assumed that the difference of layout of boundaries of magnets does not

interfere with the repulsive forces. In the calculations of the force, both rotation of the discs and the particles are taken into account by modifying the force equation as follows:

$$F_t = m\beta(R)(2\pi\nu R - \vartheta_t)$$

In this approximation for tangential force, R is the radius of the RDS, ν is the frequency of the rotation of the disc of the separator and ϑ_t is tangential velocity of the particle.

Calculation for the trajectory of the particles pushed out by the RDS is carried out numerically since analytical solutions are not possible as it was done for the VECS.

The authors conclude that the separation efficiency is mainly dependent on the size of the particles introduced to the separators and suggest that it may be possible to sort out the different non-ferrous metals based on the differences of the respective σ/ρ values as long as their sizes are similar to each other. Also mentioned is the effect of using magnets with different intensity of magnetizations (I), pointing out to the fact the term has a power of 2 so any change will have a more pronounced effect.

2.1.3. An Electromagnet to Create Magnetic Field

In a series of papers[10], [11], [12], Fletcher et al. attempt to define the variables and relations to determine the force induced on non-ferrous particles due to eddy currents in order to model the separation process. The main difference, when compared to the previous work in the field, authors employ a single magnet pole pair in a closed circuit arrangement in which they generate the magnetic field with an electromagnet instead of using a permanent magnet.

The particle stream to be separated is sent to the electromagnet pole gap at an angle to the boundary and the axes are defined as x-axis parallel to the boundary and y-axis perpendicular to this boundary and parallel to the magnet poles. It is important to note that the magnetic field generated is uniform and constant meaning that it does not change with either location or time. So, the magnetic field outside the pole gap is taken as zero whereas between the poles it is considered as B_z.

Initially, for modelling and validation purposes, the particles chosen were of frame nature. Authors employed rectangular and annulus frames of different sized metals. This choice also helps in calculations of the force, which the authors take as Lorentz Force. Thus, after necessary derivations and simplifications, the force as the frames enter the field in the y-direction is given by the equations below for a rectangular and an annular frame, respectively:

$$F_y = -B_z^2 b^2 \vartheta_y \sigma \tau \omega / (2a + 2b)$$

$$F_y = -4B_z^2 \vartheta_y \sigma \tau \omega (y - y^2/(2R))/\pi$$

where B_z is flux density, a is the edge length of rectangular frame parallel to y-axis, b is edge length of the rectangular frame parallel to x-axis, R is the radius of the annular frame, ϑ_y is velocity of the particle in y-direction, σ is electrical conductivity, τ is the thickness and ω is the width of the frame.

Observed during experiments, it was realized that based on their material (electrical conductivity and density) and geometric properties (shape and size) the extent that particles penetrate the magnetic field varies.

Neglecting the effect of friction and self-inductance the formula depth of penetration, y_L, for rectangular is follows:

$$y_L = \frac{\vartheta_{o_y} m(2a + 2b)}{B_z^2 b^2 \sigma \tau \omega}$$

The case of circular filaments is more involved and the equation is given as:

$$y_L = R \mp 2R \cos(60 + (\psi/3))$$

In this equation, the sign change and the expression for ψ are taken differently according to the value of the following:

$$\psi = \cos^{-1}\left(1 - \frac{3V_{o_y}\pi m}{2R^2}\right) \quad \text{when} \quad \left(\frac{3V_{o_y}\pi m}{2R^2}\right) < 1 \quad \text{and the sign should be taken as (-)}$$

$$\psi = \cos^{-1}\left(\frac{3V_{o_y}\pi m}{2R^2} - 1\right) \quad \text{when} \quad \left(\frac{3V_{o_y}\pi m}{2R^2}\right) \geq 1 \quad \text{and the sign should be taken as (+)}$$

Employing equations of motion to calculate the trajectory, authors consider a single step magnetic flux change in their primary publication. The measurements taken later and presented though show a gradual increase nearing the boundary of the magnetic field so a stepped model is chosen to define the B_z. This is also needed, as it was found out, to successfully define the behavior of particles, when their shapes change from frames to more solid structures.

It should be noted that the effect of induced fields are neglected and particle sizes used for experimental validations are quite small, when compared to real practices. Although considerable improvement is achieved adopting a "staircase" type of magnetic flux change at the boundary, the model is not complete in successfully addressing the behavior at low and high velocities.

2.2. Rotary Drum Design

This is the machine design currently used in the industry, construction and operational details of which were given in the first chapter. Research conducted starting from 1990's until the present day employs this machine. Prior to the novel approach created in this dissertation, in order to calculate the force due to magnetic interactions, particles were treated as magnetic dipoles (i.e. magnets). Such an approach is only applicable to small size ranges as the properties attributed to the particle change considerably when large. In cases where size is larger than the width of the magnets, the effect of magnetic fields on the particle changes too thus simplifications no longer work and validity of the model diminishes. Lastly, with the dipole model, it is quite hard to define irregular shapes of particles and researchers tried to tackle this by introducing empirical terms to account for shape factor.

2.2.1. Introduction of Magnetic Dipole Model

Rem et al. in the work published during the years 1997[13] and 1998[14] in two papers attempt to model the separation mechanism of eddy current separators of rotary drum type. The main assumption made is that particles are much smaller than the wavelength of the magnet poles, in other words the width of two adjacent opposite poles, so that the field generated by the magnets completely penetrates and saturates the volume of particles subject to separation. Another important point in this assumption is that the field penetrating the particles stays constant inside the volume of the particles.

The force on the non-ferrous particles that causes their separation by making them follow different trajectories from the non-metallic ones is calculated by the authors by employing the magnetic dipole approach. This approach requires two magnetic bodies so that the interaction between their fields and magnetic moments can be combined for calculation of the force and torque. Through observations from experiments, Rem et al. foresee the need to account for both the translational and rotational changes particle demonstrates going through the field and they adopt a coordinate system to simplify the calculations. This coordinate system is fixed on the particle and a relation is built using a coordinate transformation matrix.

$$U(t) \cdot B^{a}(t) = \mathbf{B^a}(r(t), t)$$

where U(t) is the transformation matrix, B^a magnetic field observed by the particle in its own coordinate frame and $\mathbf{B^a}$ is the field generated by magnets, which is given as a function of distance between the particle and the origin of the xyz coordinates.

To calculate the value of the magnetic field due to magnets and considering its change over time, authors treat the fluctuations as a harmonic function and define the following set of Fourier transform equations using a cylindrical coordinate system around magnets:

$$\mathbf{B_r^a} = \sum_{n=0}^{\infty} b_n (r/R_{drum})^{-(2n+1)k-1} \times \sin[(2n+1)k(\phi - \omega_{drum} t)]$$

$$\mathbf{B}_{\boldsymbol{\phi}}^{\mathbf{a}} = \sum_{n=0}^{\infty} -b_n (r/R_{drum})^{-(2n+1)k-1} \times \cos[(2n+1)k(\phi - \omega_{drum} t)]$$

In the above equations, b_n are the Fourier coefficients, k is the number of magnet pole pairs and ω_{drum} is the angular velocity of the rotor containing magnets. Attempts to solve these equations analytically using software, the authors found out that values obtained did not correlate well with measured values with a gauss meter. Thus, they adopted a method of measuring values for either B^a_r or B^a_ϕ so that coefficients can be deduced to be used in further calculations.

Based on above assumptions, Rem et al., as needed in calculations, derive the magnetic moment from approximations to reach to the following equations based on the assumptions made before that the field is changing in a harmonic manner with time:

$$M(t) = M_\omega e^{i\omega t} = N_\omega B_\omega^a e^{i\omega t}$$

The N_ω term depends on the particle geometry and size as well as conductivity together with the frequency.

Although not explicitly stated, it is understood that a force balance is used to calculate the trajectory of individual particles. In the first paper published in 1997, simple case of free falling particles is examined neglecting effects of forces other than the magnetic interactions. Second paper published in 1998 explores the effects of friction from belt and air drag.

High speed camera recordings are examined and used to plot the location of particles in time so that theoretical results can be compared to check for the validity of the model. It was found out that good correlation can be obtained with acceptable levels of experimental error for only the case of cylindrical shapes. For the case of disk and sphere shaped particles, it was observed by Rem et al. that experimental error is beyond acceptable limits to quantify as successful prediction.

Since the authors confined their concentration on modeling the behavior of particles in the range of small sizes, important factors such as initial velocity and geometrical orientation are left out of the model, which caused shortcomings, when these parameters became dominant as in the case of disk shaped particles. For the case of dropping particles to induce a free fall, it is obvious that shape will play an important factor on the speed of entrance to magnetic field and how the particle will be oriented due to air drag. Orientation is quite important since it is the change of flux that induces eddy currents inside the particles. This flux change is a result of both the magnetic field difference over time as well as the area exposed this flux change. Thus, a disk surface oriented normal to the flux lines will observe the greatest change, and of course deflective force, whereas all other orientations would result in effects of lesser degrees.

2.2.2. Introduction of Another Magnetic Roll

Zhang et al. published series of papers[15], [16], [17] in 1999 in which they mainly examine the mechanism of eddy current separation based on the forces acting on particles with the use of a new machine they invented. The machine is called High Force Eddy Current Separator (HFECS) and it employs an eccentric design incorporating 2 rolls of magnets that are spun in opposite directions. Authors claim this improves the separation of fine fraction in the feed.

In the first paper forces are introduced and their importance in separation is discussed. The forces acting on a particle are defined as gravitational, centrifugal, frictional, inter-particle, air drag and the magnetic deflective force. Equations are given on how to calculate each though most of them are either ignored or assumed to have negligible effects. These omitted forces are frictional force, inter-particle force and drag force. It is interesting to note that if friction is neglected, it is not possible to talk about the centrifugal force since particles dropping on to the shell will either bounce or will not be affected from the rotational motion of the surface to gain any acceleration (thus no force).

Zhang et al. adapt the use of magnetic dipole model proposed by Rem et al. in 1998 and proceed with theory presenting calculations accordingly though reaching to the conclusion that these are quite complicated and could be simplified using approximations to reach the following equation:

$$F_d = KB_e^2 fm\frac{\sigma}{\rho}p$$

where F_d is the magnetic deflective force, K is defined as a complex coefficient based on the machine magnet setup, B_e is the effective magnetic induction, f is the frequency of the oscillations of the magnetic field all of which are related to the machine design. Other parameters are based on the particle; m is the mass, σ is the conductivity and ρ is the mass density of the particle whereas p is related to the shape and orientation of the particle inside the magnetic field termed as the "complex particle factor". Unfortunately, the methods for obtaining the values of K and p are not explicitly defined.

Authors reach to the obvious conclusion in this first article that, in order to observe a trajectory for non-ferrous metal particles present in the stream with the non-metallics, the magnetic deflective force should be greater that all the other forces combined. This is simply a force balance approach and is pretty similar in the logic to what was proposed by Rem et al. in earlier work. Observations from experiments and the conclusions reached also strongly suggest a qualitative work rather than a quantitative one.

In the second article they published, more detail is presented but the model is still the same; magnetic dipole as proposed earlier. A quantitative approach is undertaken as can be clearly seen from the complex equations that were derived to define the magnetic field observed by particle, the magnetic moment and the resulting force. Here authors come up with the concept that eddy currents induced on the particle due to change of the magnetic field from the magnets need to decay because of the internal resistance of the particles. It is suggested that in that duration of decay of currents the force is observed due to magnetic field interaction. Zhang et al. further elaborate that this reaction field consists of two components, a parallel and a perpendicular one both with respect to the field of the magnets. Thus, based on these components, the reactive magnetic fields are given as:

$$B_{\perp}^{i} = \frac{(k\omega_{drum} + \Omega)\tau}{1 + (k\omega_{drum} + \Omega)^2\tau^2} B^a$$

$$B_{//}^{i} = -\frac{(k\omega_{drum} + \Omega)^2\tau^2}{1 + (k\omega_{drum} + \Omega)^2\tau^2} B^a$$

and for magnetic moments:

$$M_{\perp} = -\frac{sV}{\mu_o}\frac{(k\omega_{drum} + \Omega)\tau}{1 + (k\omega_{drum} + \Omega)^2\tau^2} B^a$$

$$M_{//} = -\frac{sV}{\mu_o}\frac{(k\omega_{drum} + \Omega)^2\tau^2}{1 + (k\omega_{drum} + \Omega)^2\tau^2} B^a$$

In the above equations, k is the number of pairs of opposite pole magnets, ω_{drum} is the angular velocity of the magnet rotors, Ω is the rotational velocity of the particle in response to rotating magnetic field, τ is the decay time for the eddy currents (termed as the "memory of particles" by the authors), s is the particle shape factor and V is the volume of the particles and μ_o as the constant that equals $4\pi \times 10^{-7}$ Tm/A.

Combining the above equations and the main equation of $F = M \times \nabla B$, the following are obtained by Zhang et al. giving the tangential and radial components:

$$F_{tan} = M_{\perp}\frac{2\pi B_{\perp}^{i}}{w} = \frac{2\pi sV}{\mu_o w}\frac{(k\omega_{drum} + \Omega)\tau}{1 + (k\omega_{drum} + \Omega)^2\tau^2}(B^a)^2$$

$$F_{rad} = M_{//}\frac{2\pi B_{//}^{i}}{w} = \frac{2\pi sV}{\mu_o w}\frac{(k\omega_{drum} + \Omega)^2\tau^2}{1 + (k\omega_{drum} + \Omega)^2\tau^2}(B^a)^2$$

Also, the formula for torque is given as:

$$T = M_{\perp} \times B^a = \frac{sV}{\mu_o}\frac{(k\omega_{drum} + \Omega)\tau}{1 + (k\omega_{drum} + \Omega)^2\tau^2}(B^a)^2$$

Zhang et al. also express the term τ, decay time, in terms of particle properties as follows:

$$\tau = s'\mu_o\sigma R^2$$

where *s'* is another shape factor, σ is the conductivity of particle and *R* is defined as the characteristic size.

Unfortunately, details how to calculate or estimate is given for the terms *s*, *s'* or *R* though it is said that the shape factors incorporate the important influencing parameters such as particle orientation, particle size and of course particle shape. Also not taken into account (or details of which are not shared) is effect of belt speed or the shell speed (not the magnet rotors), distance of magnetic field to particles as well as the position of the magnet rotors. Another important point worth mentioning is that the particle sizes that were tested or simulated are too large to have the skin effect neglected. Thus, it is again hard to treat the improved model as a complete and a quantitative one.

2.2.3. Magnus Effect in Aqueous Medium

In the work published by Fraunholcz et al in 2002[18], Magnus effect is attempted to be introduced into eddy current separation as a novel approach and the medium used is air instead of water. The separation process is modeled using magnetic dipole approach undertaken by many others (Rem et al., Zhang et al.) in years prior to their work. Although the operation of the machine is different, the separation mechanism is similar as the main trajectory of the non-ferrous metals is tried to be modified using magnetic interactions between a rotor of magnets with alternating poles and particles passing through the vicinity of the oscillating magnetic field created by the spinning of these magnets. So it is not surprising that the authors used the much of the theory from previous work as building blocks for their proposed model.

While the notation is a bit different, the calculation principle of magnetic induction term is basically the same as before. What is different is the magnetic dipole moment term, M, which is given by Fraunholcz et al. as follows:

$$M = -\frac{V}{\mu_o}\left[R(\xi)\begin{pmatrix}B_r\\B_\varphi\end{pmatrix} + I(\xi)\begin{pmatrix}B_\varphi\\-B_r\end{pmatrix}\right]$$

Here V is the volume of particle, μ_o is the magnetic permeability of vacuum, functions of R and I are approximation of rational functions and ξ is a term that stands for:

$$\xi = \mu_o \omega_B \sigma d^2$$

where σ is the conductivity of the particle and d is a set of parameters that depend on the shape and orientation of the particle. ω_B defined as the apparent angular velocity given by:

$$\omega_B = -k\left(U_\varphi / r - \omega_m\right) + \Omega$$

consisting of the terms, k as the number of magnets with north pole on the rotor, U_ϕ is the linear velocity of the rotor at distance r from its origin, ω_m is the rotor speed in rad/s and Ω is the angular velocity of the particle.

For calculating the trajectory of the particles, authors use a force balance approach and take into account the effects of forces due to magnetic interactions (F_m), gravity (F_g), drag (F_D) and lift (F_L) as well as the torque terms which are results of effects from magnetic field and air drag.

Numerous experiments were conducted to validate the model and actual behavior of particles and it is claimed that the results correlate well with predictions from simulations. However it is also noted that this is true for a definite size, shape and type of particle and it cannot be extended to reach to a general model.

2.2.4. Introduction of Collision Probability

Published in 2004[19], the work of Maraspin et al. mainly focuses on modeling how the particle trajectories would be for non-ferrous particles based on the magnetic dipole model first proposed by Rem et al. in 1997. This model was modified over the years by many groups of researchers in order to account for different particle related properties observed during the separation process

such as the geometry and orientation, which are found to have a great impact. The last model proposed by Fraunholcz et al. in 2002 is taken as the foundation in this work by the authors and an addition is made by introducing the interactions between particles in the form of collision probabilities.

Discussed by Maraspin et al., any non-ferrous particle that is influenced by the magnetic field of the magnets will acquire some acceleration, when compared to the non-metal particles that are traveling on the belt with a constant speed, i.e. the belt speed. Thus, a collision is expected between the non-ferrous metal particles and non-metals and this collision is taken as elastic binary collision in their simple model, the velocity gained by the non-metal particle can be estimated using the following formula:

$$\Delta v = \frac{2v}{1 + m'/m}(a \pm b)$$

where *v* is the relative velocity of the non-ferrous particle with respect to the non-metal particle, *m* and *m'* are the masses of the non-ferrous and non-metal particles respectively. The terms *a* and *b* are said to depend on the characteristics of the colliding particles.

By further analysis of the actual conditions during the separation process, the authors decide it is important to estimate the number of collision between particles. Deriving two separate equations for non-metals and non-ferrous metals, they build a relationship between the number of non-ferrous particles and projected area of the non-metals on the belt, introducing also Gaussian distribution terms for the velocity of the particles in question.

While modeling the force due to magnetic interactions, authors give details about a term *D*, which simplifies the irregular shape of particles to an equivalent circle of largest diameter that can be fit inside the irregular shape in question. However, it is known that the area that is subject to the magnetic field interactions is quite important in the force generated and such a loss of area, unless account by introduction of other terms or modification of existing ones, is expected to give erroneous results.

The authors conclude that the experiments they ran with particles alone and mixtures of particles provide the notion that the collisions play an important role in the effective separation of non-ferrous from non-metals and that better separation can be obtained moving to a lower collection zone since distance between the thrown non-ferrous and falling non-metal trajectories is more pronounced.

2.2.5. Modified Dipole Model with Ring Method

In a series of two papers[20], [21], Ruan and Xu bring a new approach to the calculation of force due to magnetic interactions between magnets and non-ferrous metal particles in an eddy current separator and employ these calculations for simulating the behavior of particle trajectories to reach to a formula that gives the separation distance between the metals and non-metals. Authors build their model on the basis of treating the non-ferrous metal particles (aluminum flakes for their case) as induced magnetic poles.

In their first article published in 2011, Ruan and Xu build a model on the basis of treating the non-ferrous metal particles (aluminum flakes for their case) as induced magnetic poles in order to calculate the magnetic force. The steps they take to calculate this force is as follows:

i) Calculation of eddy current densities in particles
ii) Calculation of magnetic flux in particles due to eddy currents
iii) Calculating the force due to interactions between the magnetic flux of particles and magnets

Ruan and Xu start with characterization of the type of particles present in their feed stream, which consists of crushed toner cartridges with respect to their shapes. Particle shapes are grouped into three as circular, rectangular and triangular. As a next step, in order to calculate the magnetic flux density of the magnets, they adopt the model proposed by Rem et al. for oscillating magnetic fields, given in circular coordinate system as Fourier series. Simplification is made by the assumption that due to the sparse setting of poles the flux lines penetrate the particle at right angles (90^o). Determining the Fourier coefficients by measurements as was

suggested by Rem et al. originally, Ruan and Xu reach to the following equation for magnetic flux density:

$$B_r = 0.135(r/R)^{-10} + 0.095(r/R)^{-28}$$

where r is the distance between the particle and the magnet rotor center, R is the radius of the magnet rotor. This is a machine design specific term.

For calculation of eddy currents in particles, authors derive equations for the three different shape groups from first principles and employing Faraday's Law of Induction, Ohm's Law. These are given below starting with circular shape followed by rectangular and triangular shapes, respectively.

$$J^C = \frac{B_r k(\omega_m R - v)\gamma T}{4\pi R} R_p^2$$

$$J^R = \frac{B_r k(\omega_m R - v)\gamma T L W^2}{8\pi R W((L/W) + 1)}$$

$$J^T = \frac{B_r k(\omega_m R - v)\gamma T W L^2}{8\pi R C}$$

It can be seen from the above equations that common terms are present among them, the parameters that are different are directly related to the shape and geometry of the particle in question. Above, k is the number of magnet poles, ω_m is the angular velocity of the magnet rotor, v is belt speed or particle feeding speed, γ is the conductivity of the particle, T is the thickness of the particle, R_p is the diameter of circular shaped particles, W is the width of the rectangular or triangular particle, L is the length of the rectangular particular and at the same time it is used for the height of the triangular particle, C is the circumference of the triangular particle.

Employing the Biot-savart Law, authors calculate the induced magnetic flux for each particle shape, based on the below equations:

$$B_p = \mu_o J \quad and \quad \phi_p = B_p S_p$$

where B_p is the induced magnetic field of the particle, μ_o is the magnetic permeability of the vacuum (4π x 10-7 Tm/A), J is the eddy current density, Φ_p is the magnetic flux induced in particle and S_p is the largest cross sectional area of the particle projected to horizontal.

So combining all the derived equation for eddy current density and induced magnetic fields and induced magnetic fluxes, the following are obtained for each shape type, where V is the volume of the particle:

$$\Phi^C = \frac{B_r k(\omega_m R - v)\gamma V S_p \mu_o}{4\pi^2 R}$$

$$\Phi^R = \frac{B_r k(\omega_m R - v)\gamma V S_p \mu_o}{4\pi R} \frac{W}{2(L+W)}$$

$$\Phi^T = \frac{B_r k(\omega_m R - v)\gamma V S_p \mu_o}{4\pi R} \frac{L}{C}$$

An interesting approach for calculation of the repulsive force is undertaken by the authors, employing an equation pretty similar to Coulomb's Law. It is understandable that since they assumed the interactions are between two magnetic poles, this kind of approach seems plausible. So, the general force equation is given as:

$$F_r = \frac{\Phi_p \Phi_m}{4\mu_o \pi h^2}$$

In this formula, h is defined as the radial distance between the particle and the magnet surface, which can also be expressed based on geometric relations:

$$h = \frac{R}{\cos \alpha_o} - R$$

Substituting this to the force equation given above, formula for the repulsive for could be written as:

$$F_r = \frac{\Phi_p \Phi_m}{4\mu_o \pi R^2} \frac{1}{(\sec \alpha_o - 1)^2}$$

where Φ_m is the magnetic flux due to the magnets and α_o is the angle between the vertical (y-axis) and the line connecting the particle to the center of the magnet rotor (origin of the coordinate axis). As done before, for different shapes, respective expressions for force could be obtained by substituting the derived terms above.

Experiments carried out by Ruan and Xu show good correlation in terms of predicting the separation angle where the lift off particles is observed from camera captures and α_o calculated from the equations.

As a next step, in their article published in 2012, authors examine the separation efficiency of the equipment and reach to the conclusion that of all the influential parameters, the ones that can be easily manipulated were identified and employed to calculate "separation distance". Separation distance is defined as the distance between non-ferrous metal particles and non-metallic ones after ejection from the belt (so any effect of magnetic fields would be diminished) at a given vertical distance down from the center of the magnet roll. Ruan and Xu chose belt speed (or as they call it feeding speed) *v*, difference between the belt speed and the magnet rotor speed *v'* (i.e. ωR-*v*) as well as the collection position of the particles (the vertical distance from the center of the roll down). All these parameters are incorporated in an orthogonal experimental design for studying the extent of their effects on the separation distance.

Assuming no drag and using a constant belt speed of 0.4m/s, two different magnet rotor speeds were chosen as 400rpm and 800rpm in order to calculate the trajectories of different shaped particles (circular, rectangular and triangular) of different sizes. Employing the repulsive force

equations and combining them with basic laws of motion authors calculate both the vertical and horizontal throw of not only non-ferrous particles (aluminum) but also non-metals (plastic) too. It was found out that efficiency increases with particle size and speed of the magnet rotor. Noted also is the effect of geometry of the particles and Ruan and Xu suggest that circular particles would perform the best.

3. ANALYSIS AND DATA ACQUISITION USING HIGH SPEED IMAGERY

In order to measure the success of any developed model, one would need to confirm its validity for obtaining qualitative results through experiments. This chapter focuses on the explanation of the novel methods developed to analyze the behavior of particles during the separation process in ECS, which were later used in validating the novel approach taken to develop formulas and the new particle trajectory simulator.

Details will be presented on these newly designed experiments, which were conducted to analyze the separation process and the method of data collection employing high speed imagery. Materials used, procedures followed and results obtained will be presented in the subsequent sections.

3.1. Introduction

Eddy current separators are being used in the recycling industry successfully for decades to separate the non-ferrous metals from non-metals. In the very basic sense, a mix of materials is fed as monolayer to a belt conveyor, which introduces the mixed material to an oscillating magnetic field created by the rotation of permanent magnets inside the pulley at the discharge end of the conveyor. The magnetic interactions between permanent magnets and non-ferrous metals induce a projectile motion for the metal pieces whereas non-metals, since unaffected by the magnetic interactions, follow a natural discharge path at the end of the conveyor.

Although achieving an efficient separation is complex and depends on many parameters, the basic goal is to have the maximum spacing (vertical, horizontal or both) between metals and non-metals such that they can be collected in separate regions. Traditionally, in order to assess the performance of separation, landing points past the belt on the same horizontal plane were compared. Unfortunately, this approach offers limited information to explain the mechanics behind, as discussed below.

Considering the case of firing a cannon ball where the range of a trajectory depends on its initial velocity and the angle at which it starts its motion, exactly same range values could be obtained

for different combinations of initial velocity and angles, meaning that it is not possible to identify a specific trajectory. As trajectories are essential in determining the nature of net force acting on the body, they should be investigated further in detail.

Investigation of trajectories for assessing the performance of an eddy current separator is a challenging task due to the following facts:

- Interference in operation of electronic equipment due to magnetic fields
- Rotational motion of particles preventing automatic tracking
- Inability to confine whole motion from a single vantage point
- Speed of particles
- Non-contact operation

In order to overcome above stated problems, a high speed camera was employed capturing videos at 10,000 frames per second placed directly above the eddy current separator. The videos were later examined to analyze the motion and to construct plots of trajectories.

3.2. Materials

Materials and equipment used will be described in detail in the following sub-sections.

3.2.1. Eddy Current Separators

Two types of eddy current separator were used during the tests, based on their design of magnetic rotor: a concentric and an eccentric. Although the eccentric eddy current separator design offers the ability to adjust the position of the magnet rotor as mentioned before in introductory chapter, during the experiments, in order to have sound comparison with the concentric design, the rotor was kept in an upright, neutral position.

3.2.2. Metal Samples

Non-ferrous metal samples used during the experiments were prepared by punching out round discs of 5 different diameters (0.5, 0.875, 1, 1.125 and 1.5 inches) from sheets of different thicknesses (0.125 and 0.0625 inches) of 6061 aluminum alloy, to have 10 separate discs in total.

Round discs were employed for experiments to eliminate any discrepancy that could arise from orientation differences.

Discs were later hand sanded wet, using 80, 120 and 220 grit 3M Pro Grade Precision series sandpaper sheets to remove burrs. To prevent brilliance problem during video shoots, all discs were glass beaded to create matte surfaces. Upon completion of preparation steps, all samples were checked for their dimensions with a caliper. A red dot label with permanent adhesive was placed centered on only one face of each disc to aid in tracking.

3.2.3. High Speed Camera and Lens

Initially an earlier model high speed color camera, Vision Research Phantom Miro eX1, with a maximum speed of 1000 frames per second (fps) at a resolution of 640 x 480 pixels was used to conduct experiments. Although results obtained showed consistency, when repeated, the error level (~10%) in time measurements did not provide high accuracy. Thus, another high speed color camera, Photron SA5 1300K-C2, with a maximum speed of 10000 fps at a resolution of 896 x 848 pixels was employed to decrease the error to negligible levels (~1%). The camera was coupled with a lens from Sigma, model 24-70mm f2.8 EX DG.

3.2.4. Lighting

During digital image recording process, in order for an object to be clearly visible, adequate amount of light should be reflected from it and pass through the lens to hit the sensor of the camera. Basically, once the speed of capturing images is increased (frame rate), the amount of light that can pass through the lens is decreased (at same focal opening). Thus, at high frame rates such as 10000 fps, auxiliary lighting is needed.

Apart from the amount of light needed, another consideration is the presence of flicker, which is fluctuation of light intensity over time. Although not visible to the naked eye, all light sources, when powered through alternating current (AC), produce flicker since line frequency is 60 Hz. To prevent flickering problems light emitting diode (LED) type lighting are feasible when operated on direct current (DC) or used with an adapter to convert AC power to DC.

Two separate LED lights were used to illuminate the area of interest. A spot light from Nila (model Zaila) was used at 100% power (no dimming due to flicker) in a no lens setting for area specific illumination. For the purpose of flood lighting, a light bar designed for use on road vehicles, manufactured by Traveller was used. It was powered by DC through a 12V car battery.

3.2.5. Belt Conveyors

An area of one meter long (in travel direction of belt) and 10 cm wide on the belt conveyor (both machines) was marked with fluorescent green label dots with permanent adhesive to create two artificial paths to provide guidance for feeding the discs, as well as serving the purpose of calibration within the software for distance. Label dots were evenly spaced 10 cm apart to create 10 squares within the area. This layout can be seen clearly in the left picture of Figure 5.

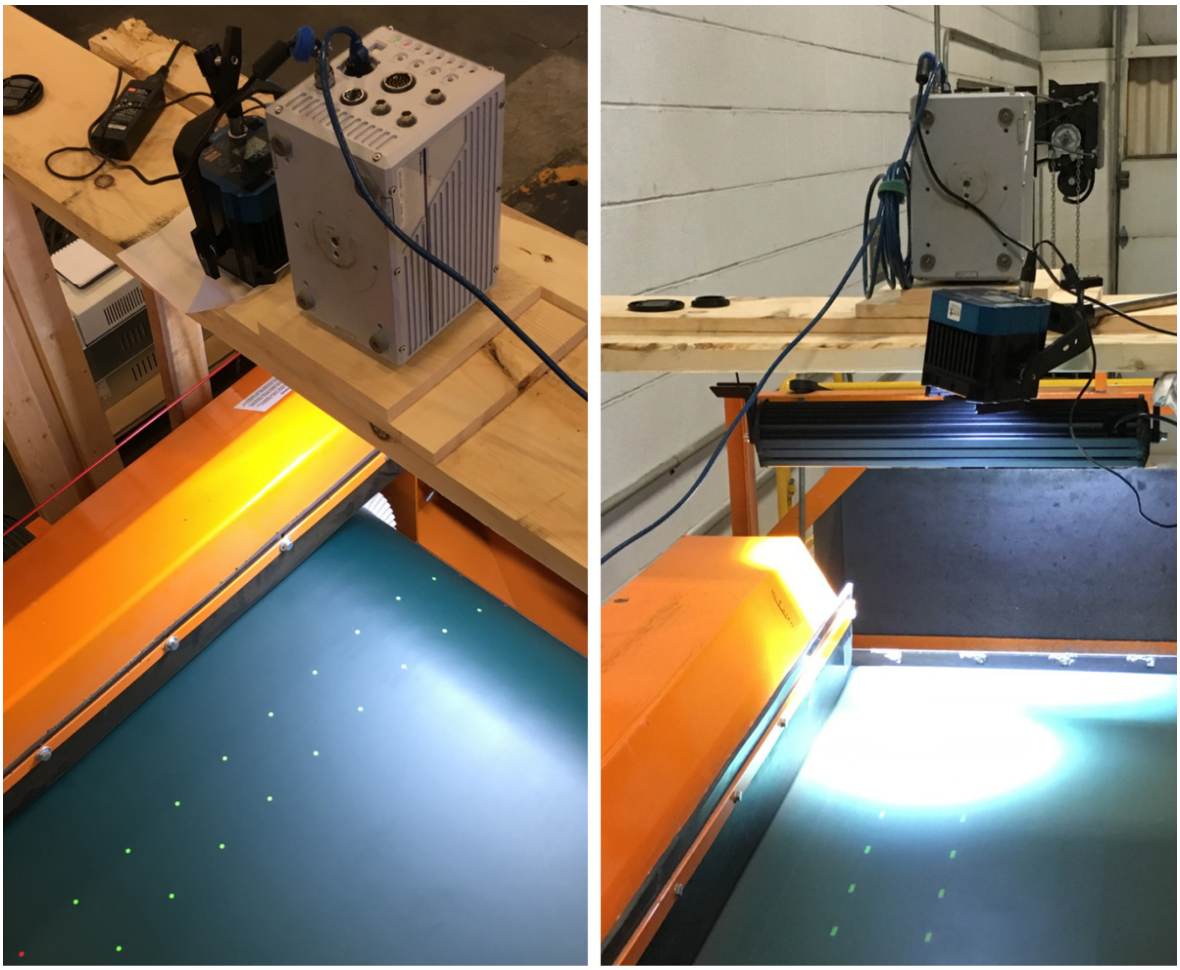

Figure 5. Experimental setup showing locations of camera and lights on different types of eddy current separator; eccentric (left) and concentric (right)

3.2.6. Other Equipment

High speed camera was controlled by a laptop connected via the LAN port. Videos were recorded onto Western Digital external solid state drives. Variable frequency drives (VFD) manufactured by ABB were used to manipulate the magnetic rotor speed (ACS800-U11-0030-5) and belt speed (ACS550-U1-015A-4) for the eccentric type eddy current separator. Concentric type had a programmable logic control (PLC) center where the magnetic rotor speed and belt speed could be modified.

3.3. Procedure

Tests were run to collect individual videos of the behavior of differently sized aluminum discs when subject to different rotational speed of magnetic rotor on two different types of machines. Belt speed was kept constant at 1 m/s for both machines in all tests.

The rotational speed of the magnetic rotor and belt speed adjustments for the eccentric type machine were accomplished via use of variable frequency drives. Before start of experiments, all speeds were verified using a mechanical tachometer and corresponding frequencies were noted. For the concentric type machine, magnetic rotor speed was varied using the permanent control unit. The frequencies used the VFD and corresponding magnetic rotor speeds are given in Appendix A.

The high speed camera was placed on a dedicated wooden frame that is free of any contact with any other equipment to prevent any adverse effects due to vibration. Exact positioning was accomplished by running trial tests to determine the most favorable setting for capturing the region of interest where magnetic interactions are taking place.

Both LED lights were positioned to illuminate the viewing area in the best possible way. For the light bar, separate wooden frame was constructed. Spot light was placed on the frame carrying the camera (Figure 5).

Steps followed to acquire and analyze the high speed videos are described in detail in the following sub-sections separately.

3.3.1. Data Collection

Sample discs were manually fed on to the belt to be situated between the fluorescent green dots present on belt's surface, in a manner that the disc face without the red dot was directly in contact with the belt.

Tests were started with the highest magnetic rotor speed possible for each machine and later were decreased next designated speed successively. In order to have the most consistent results, discs of all sizes and thicknesses were run through the machine before the rotational speed of the magnetic rotor was manipulated.

Triggering for the videos was accomplished from inside the software manually; no automatic triggers or separate mechanical triggering systems were employed. Upon capture of the video, it was trimmed to show the full motion of the disc in the field of view before the file was saved. Same procedure was repeated for all tests.

3.3.2. Data Analysis

Photron Fastcam Viewer (PFV) software was used in the viewing mode during the data analysis. Zoom level was adjusted to match an identical value for all videos. Brightness was modified as needed via software to work with sharpest images.

3.3.2.1. Time Measurements

During time measurement analysis, grid was created with MB-Ruler with 13 horizontal marker lines equally separated from each other to create 12 regions, as shown in Figure 6 and illustrated in Figure 4. Vertical lines of the grid were not employed for any measurement but were rather used to investigate path deviations, which were non-existent. After initial design and creation, no modifications were made to the grid between videos or between different test conditions.

PFV was calibrated using the fluorescent green dots placed on the belt (Figure 6). The distance between the marker lines was measured and found to be constant, though being different for the eccentric and concentric machines since the distance of the camera to the belt surface was not the same.

Verification of constant belt speed was carried out by measuring the number of frames for the center of a fluorescent green dot to cross two adjacent marker lines. Results confirmed constant belt speed for both machines.

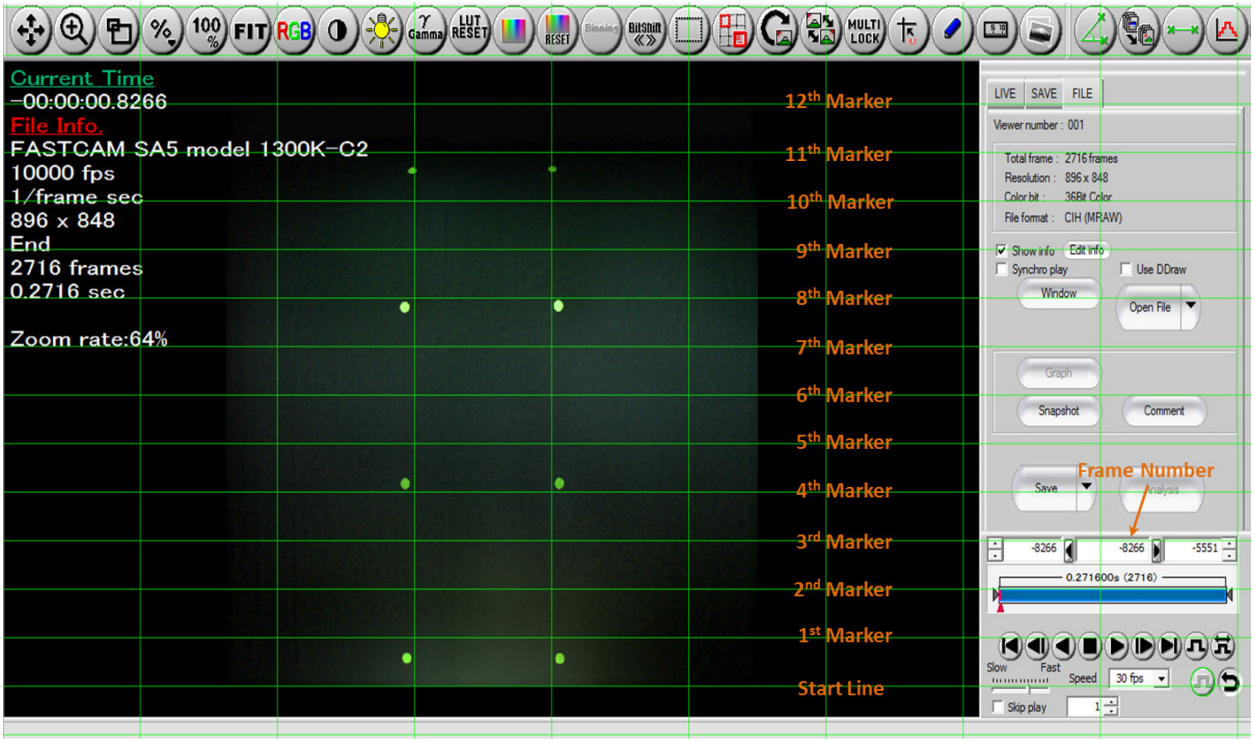

Figure 6. Interface of PFV and MB-Ruler grid overlay used for time analysis

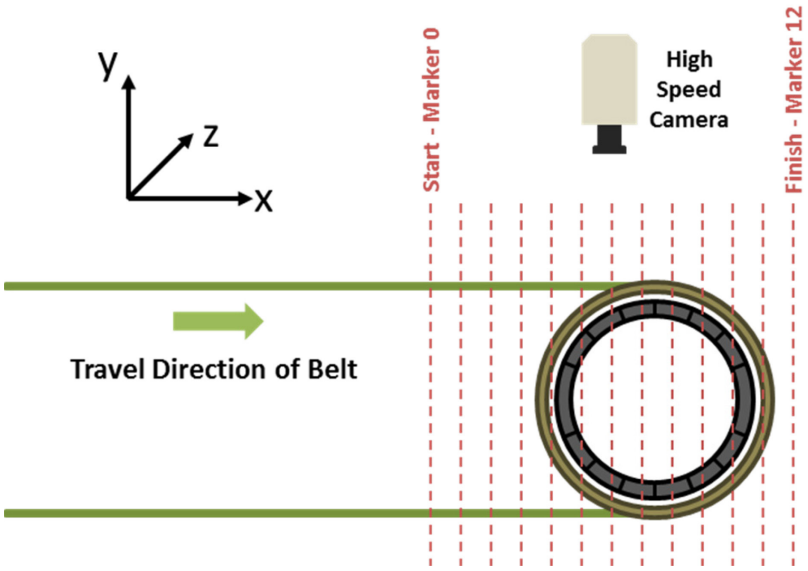

Figure 7. Illustration of coordinate system, camera location and markers used for time analysis

Time elapsed for the disc to cross the region between two adjacent marker lines was determined by subtracting the initial frame number from the final one. When visible, red dot label placed on the disc was used as the point denoting the center of gravity but, when it was not visible due to rotation, axis of rotation was chosen to be the reference point. An example of such a measurement is presented in Figure 8 where the disc is seen crossing the 7^{th} marker at frame 6403.

3.3.2.2. Size Measurements

In order to plot the trajectories of the discs, position of the discs in the vertical direction is needed. Although other methods for tracking were considered such as Light Detection and Ranging (LIDAR), precision of such systems compared to the method applied here is considered inferior due to the lack of speed of data acquisition.

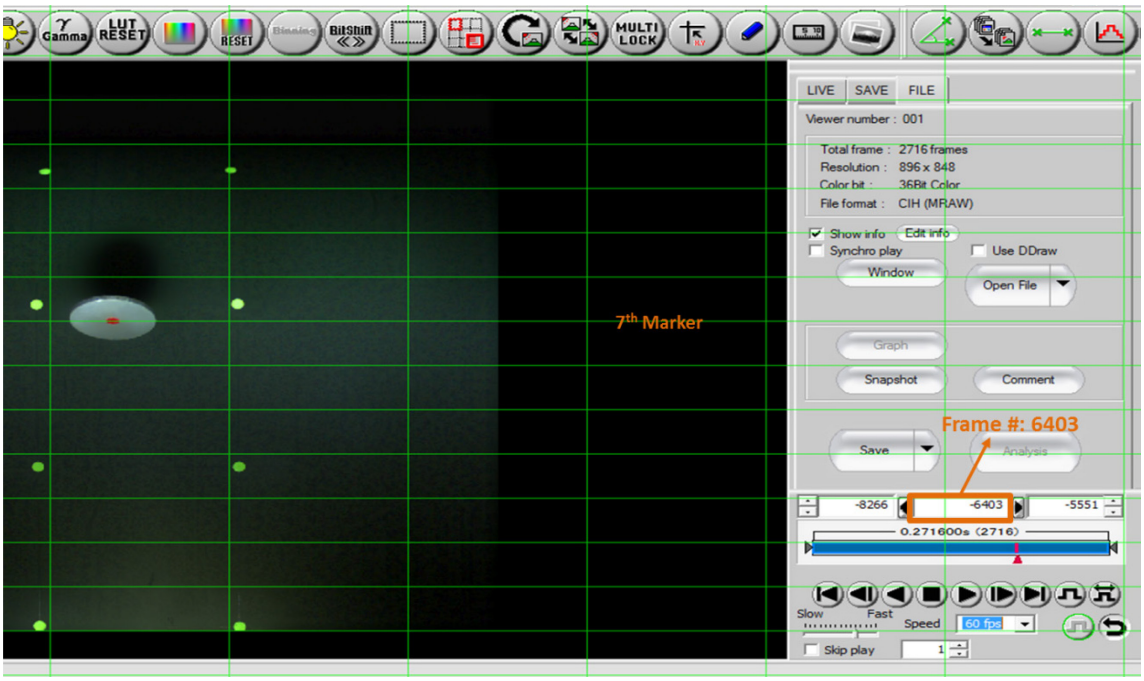

Figure 8. Example of time measurement (Frame number at 7th marker determined)

To determine the position of the discs, the change in size was employed based on the simple fact that an object will appear larger in size if moved closer to the camera than its original position. Measurements were carried out using the distance measurement tool within the software for each experiment as shown in Figure 9. Before each measurement, calibration was done using the fluorescent green dots on the belt to get the dimensions correct.

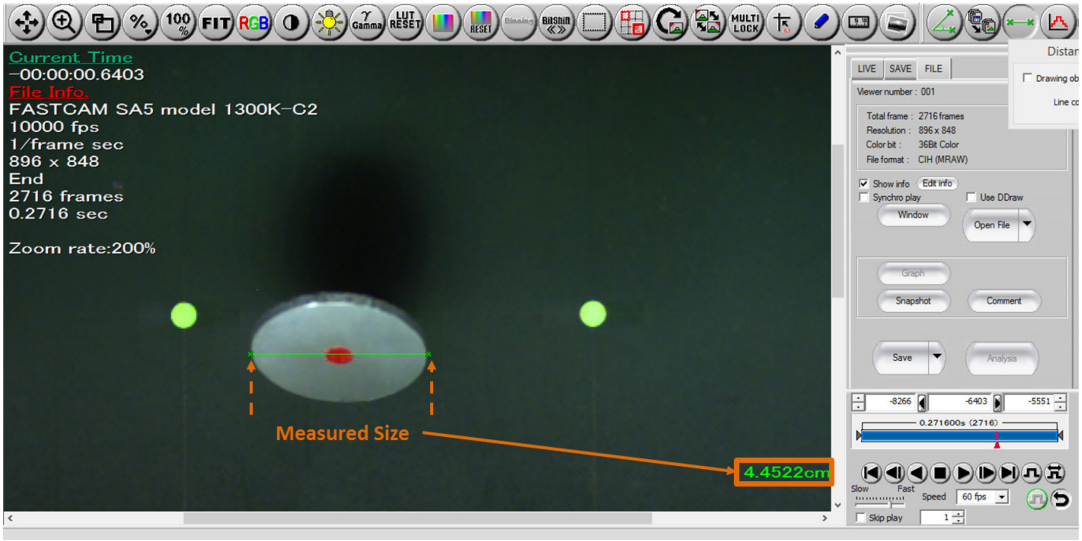

Figure 9. Example of size measurement

3.3.2.3. Conversion of Measured Sizes into Height

As the distance between the viewer and an object is increased, the perceived size of the object gets smaller and vice versa. A relation can be built in order to correlate the change in size to the distance. Such a relation is paramount for determining the trajectory of the particles as observed from the camera.

The problem is presented in Figure 10 below. When the particle is on the surface of the belt, its perceived size is equal to its true size in z-direction since calibration is carried out via the software. Once the particle starts moving in y-direction (i.e. is airborne) its perceived size increases in both x and z-directions while the shape of the particle gets distorted in x-direction since the angle it is being viewed at now is different. Thus, in order to carry out calculations accurately to reflect the height of the particle, the dimension in z-direction should be monitored at all times.

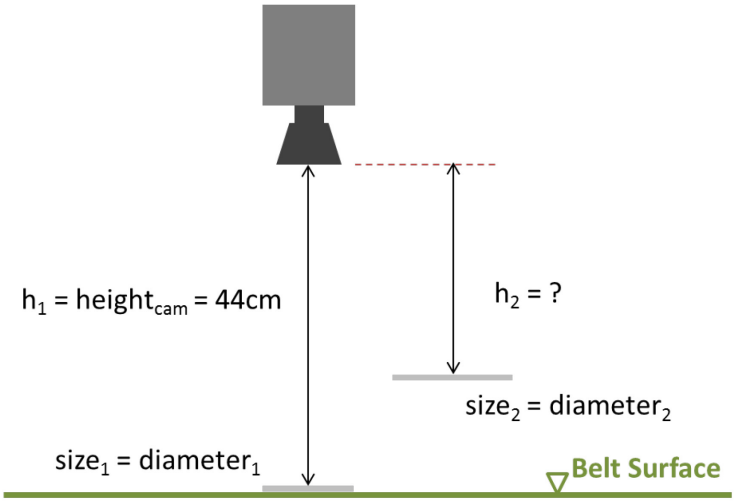

Figure 10. Distance Determination Problem

The perceived size of the particle and its distance from the camera are inversely related; as the particle gets closer to the camera its size increases. A relation can be built defining the initial and final condition to calculate the distance of the object from the camera such as:

$$h_1 * size_1 = h_2 * size_2$$

Rearranging this to find h_2, the following is obtained:

$$h_2 = \frac{h_1 * size_1}{size_2}$$

In the equations above, h_1 is the distance of the particle from the camera when on belt, h_2 is the distance of the particle from the camera when airborne; $size_1$ is the actual size of the particle when on belt and $size_2$ is the measured size of the particle when airborne. Once the value h_2 is determined, in order to find the height of the particle from the belt surface, it is subtracted from h_1.

3.4. Results of Time Measurements

Data obtained from travel time analysis are presented in Figure 11 for the concentric type eddy current separator and in Figure 12 for the eccentric eddy current separator. In both graphs, the horizontal axis shows the rotational speed of the magnetic element and the vertical axis gives the total amount of time taken by the particle to view plane in x-direction. It should be noted that the distance traveled by the particles are always the same, meaning, the particle was travelling faster when the total time was shorter. In order to reach to faster speeds, since all particles were travelling at belt speed before experiencing any effect of the magnetic field, force acting on them should have been greater.

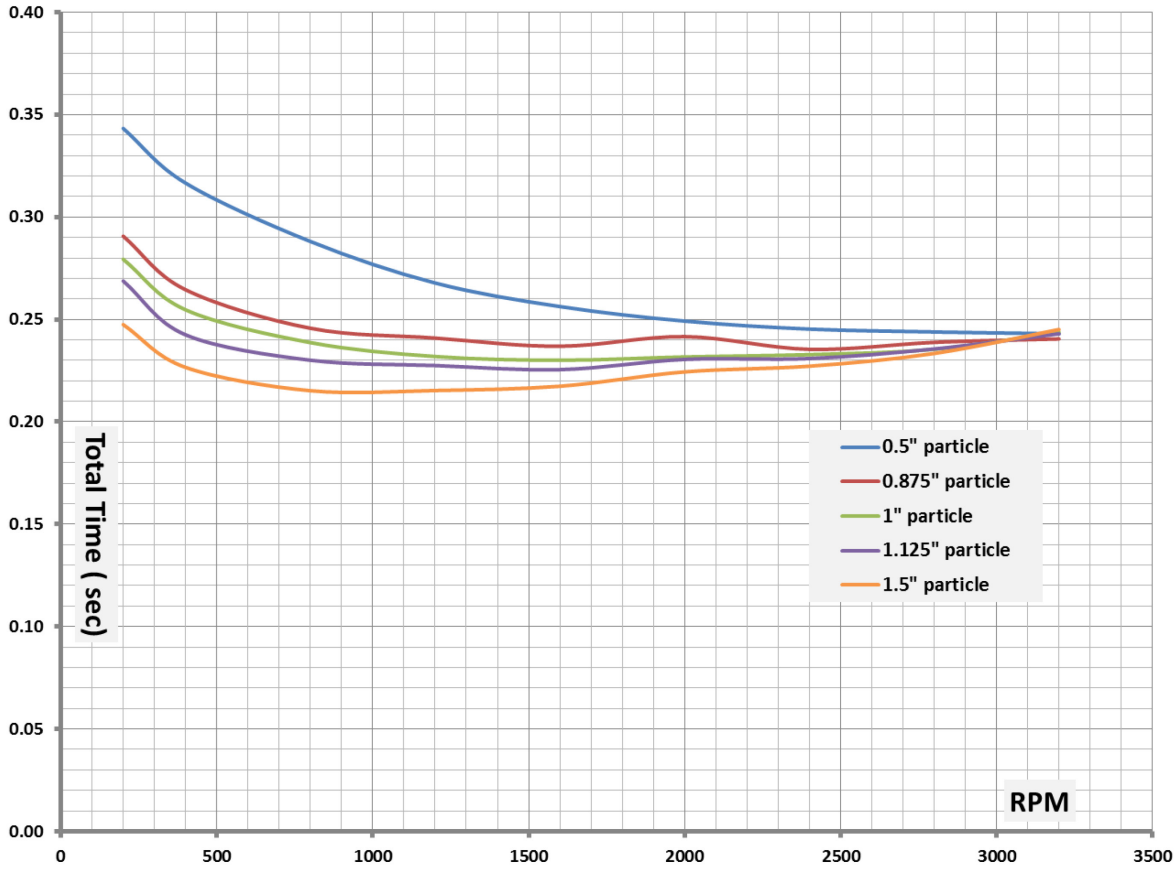

Figure 11. Measured times of travel for particles, concentric type eddy current separator

As it can be seen from Figure 11, increasing the rotational speed of the magnetic element has a positive impact on the speed of particles, though the effect diminishes past some speed for especially coarse particles. The reason of this is that as the speed of the magnetic element is increased, particles experience as stronger lifting force due to the magnetic force in y-direction; not getting the chance to be accelerated by the component of magnetic force in x-direction.

Further investigation was carried out in which the belt of the eddy current separator was stopped and particles were hand fed into the field slowly to examine the effects of magnetic force. It was found out that at low rotational speed of the magnetic element, particles are accelerated rapidly in the x-direction while not being lifted off the belt noticeably. Increasing the rotational speed of the magnetic element diminishes the effect up to the point that as the lift-off due to the component of magnetic force acting in y-direction is so great that it repels the particle back on to

the belt in negative x-direction, when particle sizes are small. For the particle with largest diameter (1.5”), the leading edge (i.e. edge closest to the magnetic element) lifts off and stays levitated for a few moments before accelerating towards the magnetic element. Such observations are not possible when the belt conveyor is moving as the friction between the belt and the particle will provide enough force to drive it into the magnetic field.

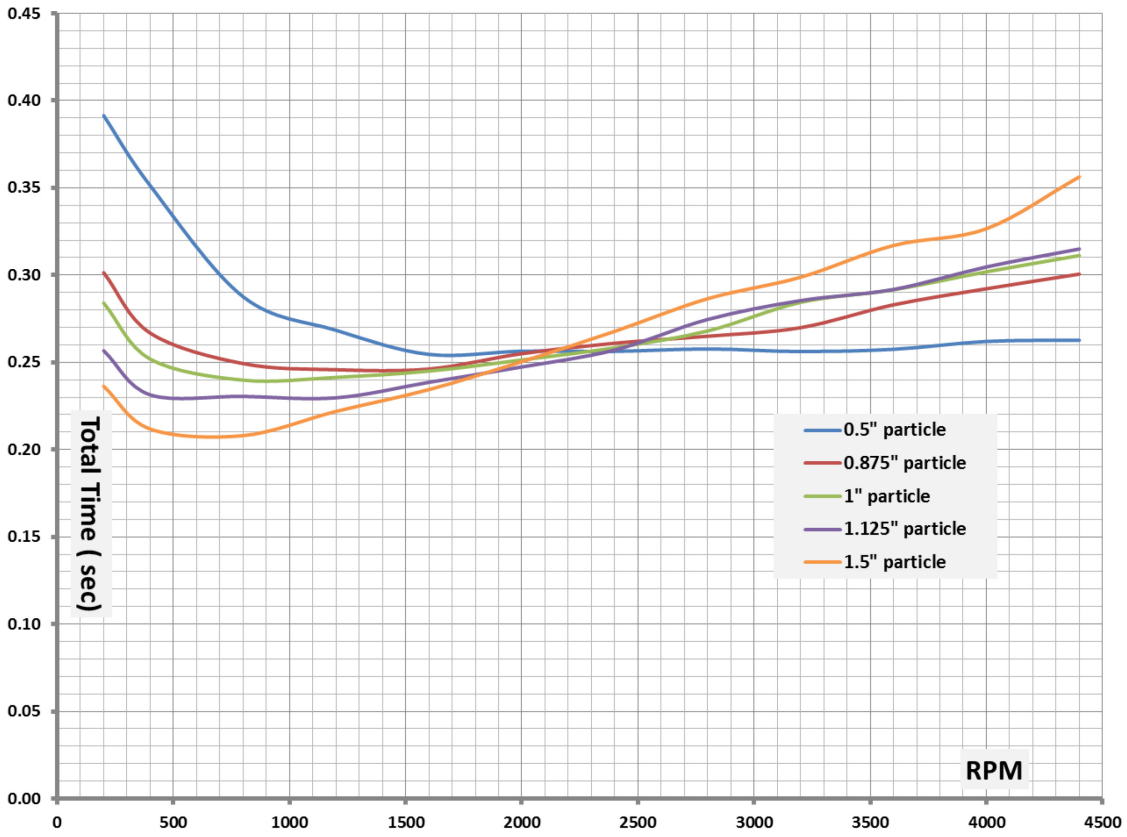

Figure 12. Measured times of travel for particles, eccentric type eddy current separator

When the data for measured times for the eccentric type eddy current separator is examined, the effect discussed above can be seen more clearly. This is an expected outcome since this type of machine is designed to improve the recovery of fine sized particles rather than coarse ones. It can be seen from Figure 12 that when operating this machine to process a feed of mixed sizes, recovery of coarse sized particles could be impacted negatively if high rotational speeds are chosen.

Comprehensive results of time measurements are presented in Appendix B.

3.5. Results of Size Measurements

Data obtained from the size measurements support the conclusion reached before; as the rotational speed of the magnetic element increases, the perceived top size in the trajectories also increase, reaching their peak at the highest rotational speeds.

Appendix C contains graphs showing the relation of change in size with varying rotational speed of magnetic element for both types of design.

4. DERIVATION OF THE FORMULA FOR MAGNETIC FORCE CALCULATIONS

In this chapter the novel approach used for the derivation of new equations will be explained in detail. These equations were used to calculate the magnetic force to calculate the lift-off locations of particles. In the last section of this chapter, results obtained by newly derived formulas to determine the locations where lifting off of the particle starts will be compared to experimental findings obtained by the novel analysis methods developed in Chapter 3.

4.1. Fundamentals

As covered in Chapter 2, describing the relation between metallic particles and magnetic field of eddy current separators is a challenging task. Assumptions that were made in order to simply the problem to implement a solution usually limited practical applications. Considering the highly variable nature of feed material in a recycling operation, it is clear that any adopted approach to determine the interactions in terms of force require flexibility and accuracy in terms of metal type, shape and size.

Before giving out the details of the method employed to derive the equation for the magnetic force, it is important to address the sequence of processes that lead to separation of metals from non-metals in an eddy current separator.

Variation of the magnetic flux acting on metals will create potential differences within the metal. This potential difference, which could also be termed as an electromotive force (EMF), creates currents, called eddy currents. As with any current, eddy currents also have magnetic fields. Interaction of the source magnetic field causing eddy currents and the magnetic fields of eddy currents give rise to either repulsion or attraction depending on whether the magnetic flux density is increasing (repulsive) or decreasing (attractive).

The simple definition above incorporates the powerful fundamental equations in electromagnetism. The first one is called Faraday's Law, which states that the flux through any open surface is a function the magnetic flux density (magnetic field strength) multiplied by the area:

$$\phi = B \cdot A \quad (1)$$

This is a dot product, meaning that it can be rewritten in the following form:

$$\phi = B * A * cos\theta \quad (2)$$

where θ is the angle between the magnetic field and the vector perpendicular to the area of the surface. When the magnetic field and area are parallel, i.e. $\theta=90^{o}$, there is no field penetrating the surface thus flux is non-existing.

Faraday's Law of Induction states that when the flux ϕ is changing with time, an EMF will be generated.

$$\frac{d\phi}{dt} = EMF \quad (3)$$

The value and direction of the EMF is given by Lenz's Law, which describes that any EMF generated will oppose the behavior of the source it created it. Thus, above equation needs to be modified to:

$$\varepsilon = -\frac{d\phi}{dt} \quad (4)$$

If one substitutes Equation 2 into Equation 4, then:

$$\varepsilon = -\frac{d(BA\cos\theta)}{dt} = -\left(\frac{dB}{dt}A\cos\theta + B\frac{dA}{dt}\cos\theta + BA\cos\theta\frac{d\theta}{dt}\right) \quad (5)$$

Equation 5 describes that EMF can be generated in all different ways. Change in the magnetic flux density or magnetic field strength in time, or, change due to distortion in the area present in the magnetic field could also cause an EMF. The orientation of the surface within the field as

given by the last term would play a role in creation of an EMF. Thus, all should be considered when calculating the EMF generated.

In majority of the cases, if not all, as rigid particles are present in the feed to eddy current separators, effect of second term in Equation 5 can be disregarded. This would leave the first and last terms for consideration in calculations.

When surfaces, i.e. particles of real world sizes, are in question it should be remembered that distance of each region within the surface will not be at the same distance to magnets, when in the field. In other words, the effect of the changing field will be different and needs to be calculated individually since any assumption that effects of the magnetic field is homogeneous would either an over or under estimation. Such a task is quite ambitious unless some observations and assumptions could be made to simplify the problem.

4.2. Coordinate System

The coordinate system selected is given in the Figure 13, below. The horizontal direction parallel to the travel direction of the belt is selected as x-axis; the vertical direction perpendicular to the surface of the belt is selected as y-axis, and, the direction parallel to the width of the belt is selected as the z-axis.

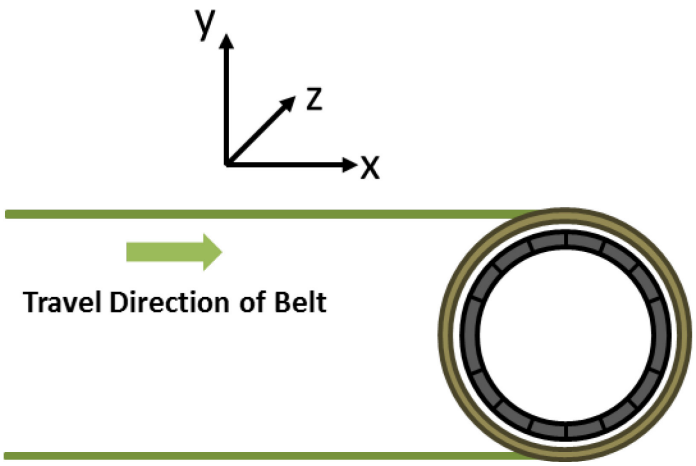

Figure 13. Coordinate system employed during calculations

4.3. Geometry

Geometric relations and the associated terms are given in the figure presented below.

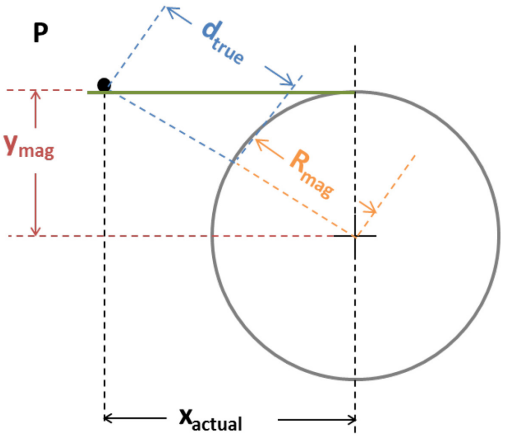

Figure 14. Geometry and related terminology

The definition of the terms introduced in Figure 14, which will be used throughout the derivations and calculations, are as follows:

d_{true}	:	distance of a location to the face of the magnets on the magnetic element
Y_{mag}	:	vertical distance (y-axis) from the center of the magnetic element
R_{mag}	:	radius of the magnetic element
X_{actual}	:	horizontal distance (x-axis) to the center of the magnetic element

All of the above terms have the unit of meters.

4.4. Analogy

Consider the case of two current carrying wires as given by the figure below. The wires are parallel to each other and the current on both wires flow at the same direction.

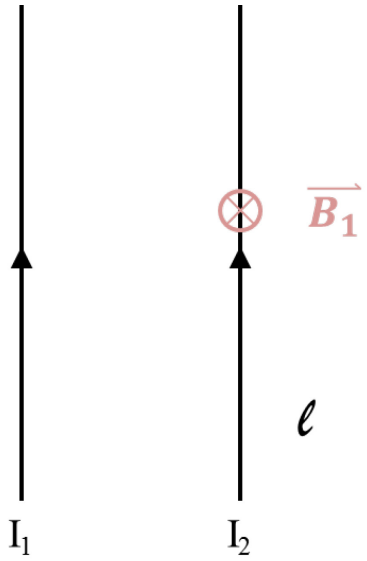

Figure 15. Current Carrying Parallel Wires

In order to calculate the force between the wires due to the electromagnetic interactions, the following formula is employed if the current is uniform and distance between the wires is constant:

$$F_{1-2} = I_2 \times B_1 * l \tag{6}$$

where B_1 is the magnetic field created by current I_1, I_2 is the current on wire 2 and ℓ is the length of the wires. If the force per unit length needs to be calculated, Equation 6 can be rewritten as:

$$\frac{F_{1-2}}{l} = I_2 \times B_1 \tag{7}$$

When examined further, it would be realized that at a given instant, the particle will have a collection of points that are equidistant to the magnets. These points can be formed into a line to simulate a wire on which the magnitude of B from the magnetic element will be the same. Thus for any particle of solid shape, the particle can be thought as made up of such lines (i.e. "wires"). The current acting on unit length of any chosen line parallel to the axis of rotation of magnetic element will be the eddy current, I_{eddy}, formed by the oscillation of source magnetic field

whereas the magnetic field strength, B, will be the magnitude of the field at that particular location.

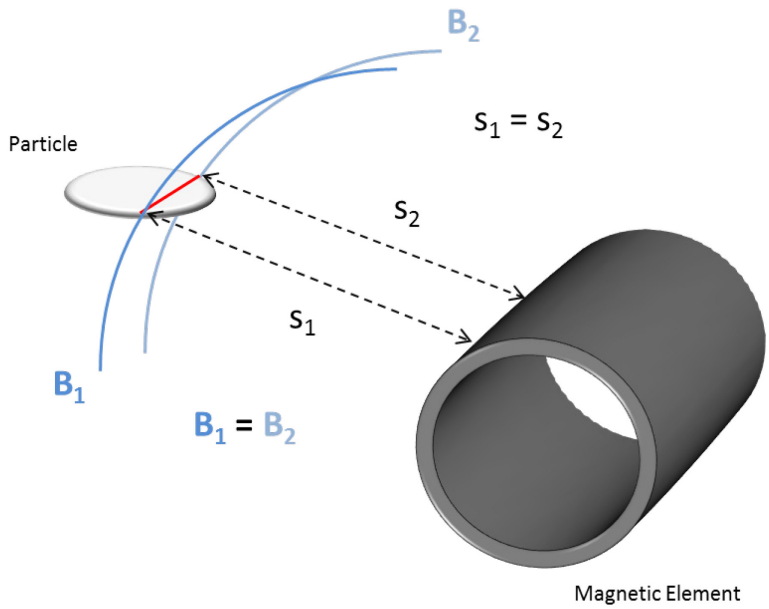

Figure 16. Line made up of equidistant points on particle

Multiplying these two values by the length of the line selected on the particle, one can find the total force on the selection. By adding up all the vectors of force acting on all selected lines, one can find the total force acting on the particle.

4.5. Derived Formula

In order to calculate the force acting on a particle due to magnetic interactions in an eddy current separator, the analogy newly developed in section 4.4 will be used together with the fundamental formulas introduced in section 4.1. At the beginning, focus will be on calculating the EMF induced by the changing magnetic field along any line selected on the particle. In order to this, Faraday's Law will be employed. Later, the EMF will be converted to current so that I_{eddy} can be found. And in the end force will be calculated by multiplying I_{eddy} by B, magnetic field strength, present at that location.

4.5.1. EMF

In section 4.1, the following was obtained to calculate the EMF generated:

$$\varepsilon = -\left(\frac{dB}{dt} A\cos\theta + BA\cos\theta\frac{d\theta}{dt}\right) \quad (8)$$

Examining the layout of the process in an eddy current separator as given in the figure below, one will notice that before the particle lifts off from the belt surface, the only change in magnetic field perpendicular to the surface area of the particle is due to the change in the vertical direction. In other words, the contribution of the change in the magnetic field is due to its component in y-direction; component in the x-direction has no effect on the EMF.

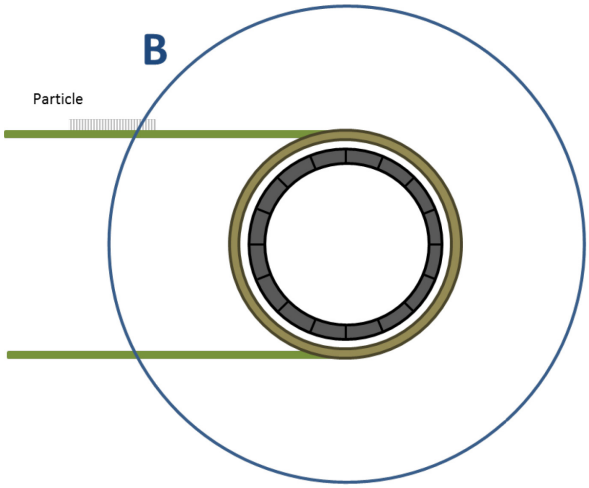

Figure 17. Position of particle and the magnetic element before any lift-off

In the operation of an eddy current separator, the required change in the magnetic field is obtained by the following effects:

- Rotation of the magnetic element (speed at which rotor turns)
- Alternating poles on magnetic element (from North to South and back)
- Motion of particle towards the magnetic element (belt speed)
- Location of the particle (distance to magnetic element)

4.5.1.1. Rotation of Magnetic Element

The speed at which the rotor is turning is usually given in units of revolutions per minute (RPM). This value cannot be used directly in the calculations so it needs to be converted into the rotational frequency. The conversion is carried out by:

$$f_{rotor} = RPM_{rotor} * \frac{1\ min}{60\ sec} \quad (9)$$

which will give the number revolutions occurring per second in Hertz.

4.5.1.2. Alternating Poles

When individual magnets are placed on a shell to form the magnetic element, in order to attain the highest amount of change, they are placed in an alternating fashion. Thus, a magnet facing out with a north pole will have a magnet before it with a south pole as well as a magnet after it, again, with a south pole.

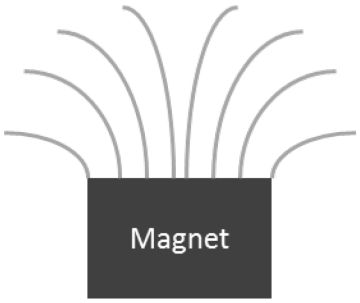

Figure 18. Magnetic Field Lines

Approaching this magnet horizontally from left to right or right to left, the magnetic flux density observed will first increase then it will decrease. Thus, for a single pole, the change in the flux density will not occurs only once but will happen twice. The total number of changes observed by the particle would be two times the number of poles present on the magnetic element.

4.5.1.3. Belt Speed

In the normal operation of eddy current separators, the rotor containing the magnets is rotated clockwise. The travel direction of the belt, and so the particles, will coincide with the direction of the magnetic element and this needs to be taken into account while considering the change. Since both are in the same direction, their difference will give the net change. In order to calculate the difference though, a conversion is needed since the motion of the belt is translational whereas the motion of the magnetic element is rotational.

The belt speed can be expressed as frequency based on the following formula:

$$f_{belt} = \left(\frac{\upsilon_{belt}}{R_{mag}}\right)\left(\frac{1}{2\pi}\right) \quad (10)$$

where υ_{belt} is the linear speed of the belt and R_{mag} is the radius of the magnetic element.

4.5.1.4. Location of Particle

As mentioned in section 4.1, magnetic field observed by the particle or any location on/in the particle will depend on its distance to the magnetic element. Calculating the magnetic field based on the magnets used and their geometry is beyond the scope of this research, thus, these calculations were performed using the software *Infolytica*, which gives a report of the magnetic flux density in x and y-directions.

Data gathered from Infolytica for a pair of magnets on the magnetic element was plotted and curve fitted in order to find an equation for calculating the value of the field at any point. Since, in generation of the EMF, interest is only in the amount of change, what needs to be taken into account is the ΔB rather than the instantaneous B values.

Visiting back the design of the magnetic element, alternating poles also give rise to opposite directions of flux, which should be considered, when introducing the ΔB term. Since B attains both positive (north poles) and negative (south poles) values, true change is twice the ΔB term. When all the equations are written down, one will have the following:

$$|B_x| = B_{max_x} e^{-66\, d_{true}} \tag{11}$$

$$|B_y| = B_{max_y} e^{-62\, d_{true}} \tag{12}$$

$$\Delta B_x = 2|B_x| \tag{13}$$

$$\Delta B_y = 2|B_y| \tag{14}$$

B_{max_x} and B_{max_y} are the maximum values of magnetic field strength that can be observed in x and y-directions. The d_{true} term above defines the distance between the specific point on the surface of a particle and the face of the magnets on the magnetic element. d_{true} can be rewritten in terms of the location in x-y coordinate system based on the geometry introduced in section 4.3:

$$d_{true} = \sqrt{(x_{actual})^2 + (y_{mag})^2} - R_{mag} \tag{15}$$

4.5.1.5. Area

Up to this point, considerations were only for the derivation of terms that caused or contributed to a change in magnetic field. Recalling Equation 8, the term for the surface area where the flux is present, also needs to be incorporated in to the equation for calculation of EMF. However, since the particle is now considered as made up of thin wires parallel to magnetic element based on the novel approach developed, area of each of these wires needs to be calculated.

Since disc shaped particles were used in the experiments, derivations will be based on that geometry. In order to create the wires on the surface of particle, it is sliced into strips that are parallel to the axis of rotation of the magnetic element as follows:

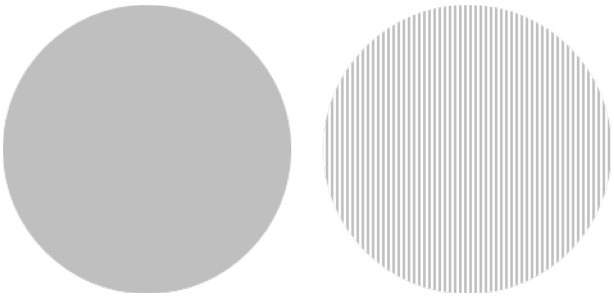

Figure 19. Slicing of the particle (solid on left and sliced to strips on right)

To mathematically define half the length of a strip, radius of the disc is swept along the arc of the particle from 0^o to 180^o as shown in the figure below:

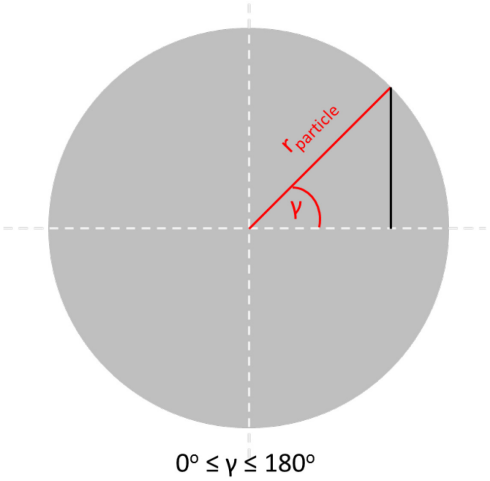

Figure 20. Formation of a half-strip on the particle

Since area of the surface of each strip is needed, steps outlined below are followed in order to find the individual area of the strips.

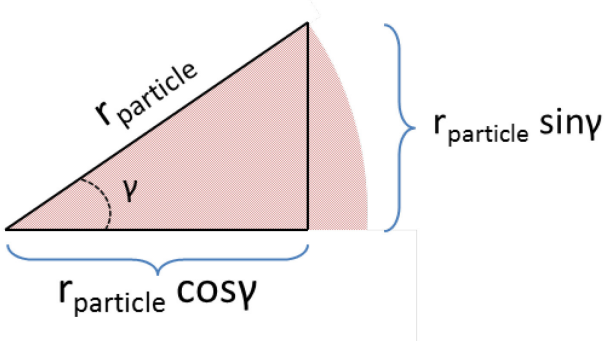

Figure 21. Geometric relations for strip area calculations

Consider the start of slicing when angle γ is advanced by a degree. A slice is formed, which represents a fraction of the total surface area of one of the circular faces of the disc. The formula for the area of slice will be given by:

$$A_{slice} = \frac{\gamma}{360} \pi \, r_{particle}{}^{2} \tag{16}$$

Interest is in the individual area for each strip, thus the area that is bounded by the right triangle as can be seen from the figure needs to be subtracted from the total area of the slice. The area for the triangle can be obtained by:

$$A_{triangle} = \frac{1}{2}\left(r_{particle} \sin\gamma\right)\left(r_{particle} \cos\gamma\right) \tag{17}$$

which, when simplified, can be written as:

$$A_{triangle} = \frac{1}{4} r_{particle}{}^{2} \sin 2\gamma \tag{18}$$

When the angle is advanced to the next value (e.g. from 2^{o} to 3^{o}), it is going to contain the cumulative area from all previous angles. This cumulative value also needs to be deducted in order to find the exact area of each strip.

Based on the findings discussed, the final equation for calculating the area of a strip would be given by the following formula:

$$A_{strip_i} = 2 * \left(A_{slice_i} - A_{triangle_i}\right) - \sum_{0}^{i-1} A_{strip_j} \tag{19}$$

Combining all the terms that contribute to the generation of EMF and making necessary arrangement as well as simplifications, formula is obtained in its closed formed as follows:

$$\varepsilon = 4(\mathfrak{f}_{rotor} - \mathfrak{f}_{belt})N_{poles}\left(B_{max_y}e^{-62d_{true}}\right) * A_{strip} \quad (20)$$

Division of the surface to 180 strips (from 0^o to 180^o) is sufficient to get small enough strips to represent dA for a particle size of 0.5" (1.27cm) in diameter. However, as the size of the particle gets bigger, the angle of advance should be decreased to prevent calculation too high of a dA value. Thus an approach of increasing the number of slices based on the diameter was adopted so that each slice is the same width no matter how big the particle is. This is accomplished by dividing the diameter of the particle by 0.5" or 1.27cm and multiplying the quotient with 180. The number obtained will later be used to divide 180^o in order to get the increment of angle between formations of each slice.

For example, for determining the angle of advance for a particle of size 1.125", first 1.125" is divided by 0.5" to find 2.25. Multiplying 2.25 with 180, one gets 405 meaning that for accuracy 405 slices need to be formed while sweeping from 0^o to 180^o. Calculating the amount of angle increment by dividing 180^o by 405, one finds a value of 0.44^o. When the same calculations are repeated for other sizes, values of 0.57^o, 0.5^o and 0.33^o are found for particles of size 0.875", 1" and 1.5", respectively.

4.5.2. Eddy Currents

As explained previously, eddy currents are formed due to the induced EMF, formula for which was derived in the previous section for a strip. In this section, calculations will be given for the derivation of the formula that will give the value for I_{eddy}.

4.5.2.1 I_{eddy} at the Surface

Current can be calculated using Ohm's Law, which states that its relation with the EMF and resistance of the medium the current is flowing:

$$\varepsilon = I\Omega \quad (21)$$

Here ε is the EMF, I is the current and Ω is the resistance. Rearranging the equation to calculate current:

$$I = \frac{\varepsilon}{\Omega} \tag{22}$$

Resistance is defined as the resistivity of a body to the flow of electric current, so the geometry of the body becomes important and has to be included in the calculations.

$$\Omega = \frac{length}{conductivity * area} = \frac{h_{particle}}{\sigma A_{strip}} \tag{23}$$

In Equation 23, $h_{particle}$ is the thickness of the particle and σ is the conductivity that is unique to the type of material used (Aluminum 6061 for this research).

Combining equations 22 and 23, current can be calculated by the following formula:

$$I = \frac{\sigma A_{strip}}{h}\ \varepsilon \tag{24}$$

Substituting Equation 20 into Equation 24 and rearranging, the formula for eddy current on the surface of a strip can now be calculated:

$$I_{eddy_{strip}} = \frac{4\,\sigma\, N_{poles}}{h}\left[(f_{rotor} - f_{belt})\left(B_{max_y} e^{-62 d_{true}}\right)\left(A_{strip}\right)^2\right] \tag{25}$$

4.5.2.2. I_{eddy} in the Volume

Equation 25, as mentioned in the preceding section, gives the current value for the eddy currents on the surface. But since the object has a thickness, eddy currents will also be formed in deeper layers from the surface and this should also be taken into account in calculations.

The magnitude of currents forming below the surface depends on a phenomenon called *skin effect*. When an alternating current is flowing or is generated by an EMF that is varying in time,

current density decreases exponentially below the surface where magnetic field effects. This is given by the graph in Figure 22.

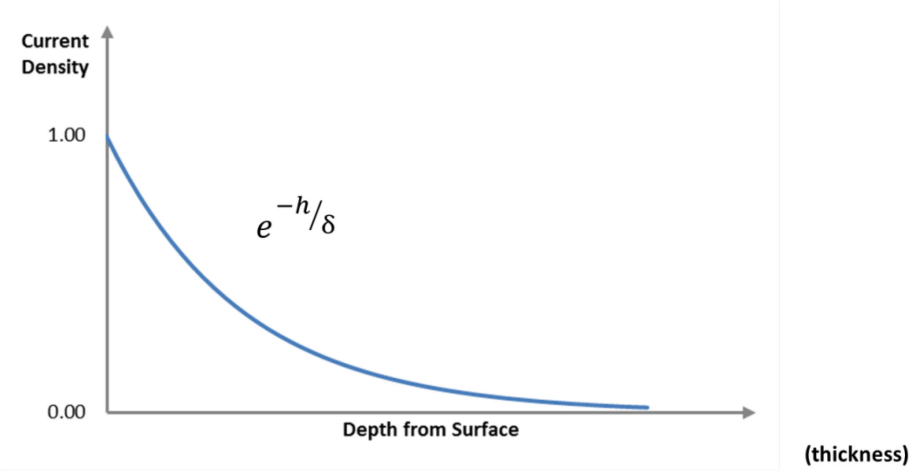

Figure 22. Relation of current density versus depth from surface

In the figure above, h is the thickness of the particle and δ is the skin depth. Skin depth is defined as the depth from the surface where the value of current density reaches to value of 1/e of its original value and is given by the formula:

$$\delta = \sqrt{\frac{2\rho}{\omega\mu}} \qquad (26)$$

where ρ is resistivity and μ is magnetic permeability of the material; ω is the angular frequency of the current.

Magnetic permeability of the material is calculated by multiplying the magnetic permeability of vacuum (μ_o) with the relative permeability of the material. Relative permeability for metals can be taken as 1, which simplifies the μ value to μ_o.

Resistivity is the reciprocal of conductivity, so it can be replaced by conductivity in Equation 26. Angular frequency can be written in terms of frequency. Substituting these, simplifying and rearranging, the following formula is obtained:

$$\delta = \sqrt{\frac{1}{\sigma \pi f \mu_o}} \tag{27}$$

From Equation 27, it is obvious that with increasing frequency, the current density will decrease rapidly meaning that less current will be present in the volume of the particle.

As calculations are aimed at obtaining the current within the volume of the particle, integration is needed to find the total volume. Figure 23 below illustrates the approach taken for the calculation of the integral.

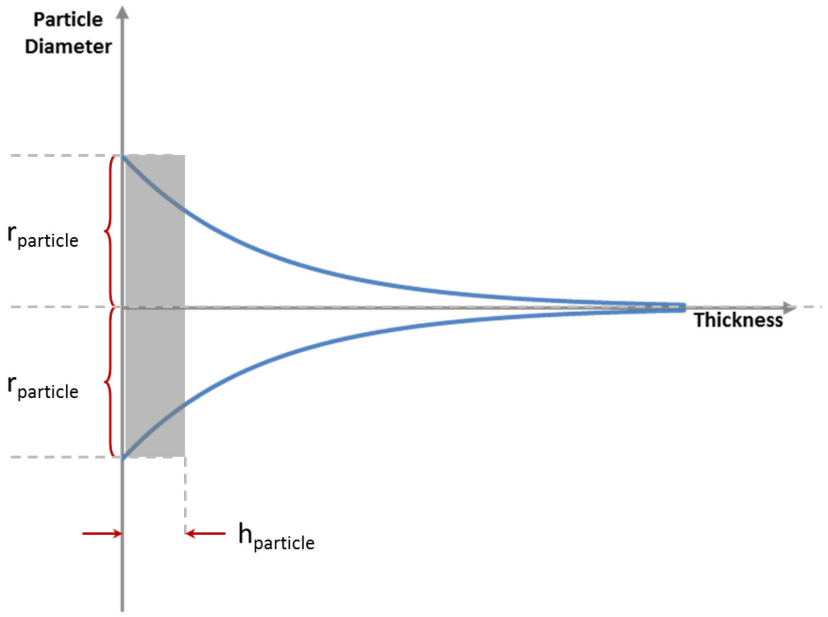

Figure 23. Geometry used for skin effect calculations

Particle surface is defined by the radius and for the integration, skin effect term should also be included as part of the radius into the area calculation. In order to calculate the total volume, for each area, thickness of *dh* will be assigned. The value of *dh* will change from 0 to the thickness of particle, which is $h_{particle}$. Writing these in mathematical terms:

$$\int_0^{h_{particle}} \pi \left(r_{particle} e^{-h/\delta} \right)^2 dh \tag{28}$$

Evaluating this definite integral, the following will be obtained:

$$\pi\, r_{particle}{}^{2} \left[\frac{\delta}{2}\left(1 - e^{-2h/\delta}\right)\right] \tag{29}$$

Since the term for area is already present in the equation for current calculations, the remainder is going to be used and termed as the *Skin Effect Multiplier (SEM)*. Equation 30, gives the formula for SEM below:

$$SEM = \frac{\delta}{2}\left(1 - e^{-2h/\delta}\right) \tag{30}$$

Here, δ is the skin depth and h is the total thickness of the particle.

Now that the loss of current density due to skin effect can be calculated, equations 25 and 30 can be combined to find the total of amount current within the strip volume, as follows:

$$I_{eddy} = \frac{2\,\sigma\,\delta\,N_{poles}}{h}\left[(\mathrm{f}_{net})\left(B_{max_y} e^{-62 d_{true}}\right)\left(A_{strip}\right)^{2}\right]\left(1 - e^{-2h/\delta}\right) \tag{31}$$

4.5.3. Force Formula

In order to calculate the force acting on each strip, right hand rule should be employed. The direction of the force is determined based on the directions of current and magnetic fields. The following figure explains how the rule is used:

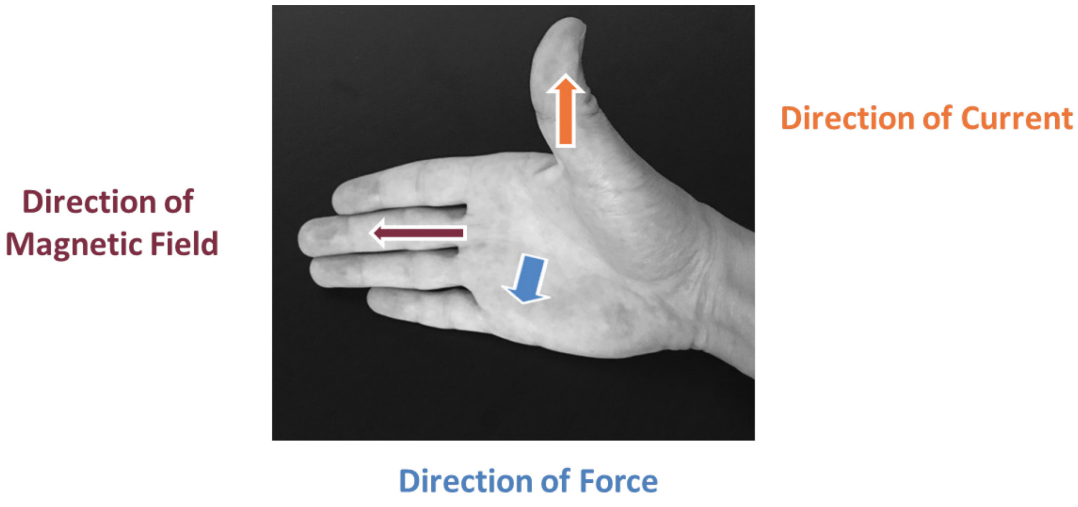

Figure 24. Right Hand Rule for Force Calculations

Recalling the analogy developed in Section 4.4 and noting that eddy currents are in fact small enough to be considered as acting individually at unit length, the force in x and y-direction can be calculated by employing the following:

$$F_x = I_{eddy} B_y \tag{32}$$

$$F_y = I_{eddy} B_x \tag{33}$$

It is counter-intuitive that the force that will be experienced by the particle in x-direction due to the magnetic interactions is caused by the magnetic field acting in the y-direction and vice versa.

Another important point to note is that due to the direction of rotation of the magnetic element, particle always experiences increasing magnetic field strengths and thus forces always act in a repulsive manner.

4.6. Method for Verification of the Derived Formula

In order to verify the validity of the formula derived for magnetic force, data obtained from the experiments for the lift-off location of particles was used.

The major, non-reactive forces acting on the particle before lift-off can be given by the free body diagram presented in Figure 25. Reactive forces such as the normal force and friction are not shown.

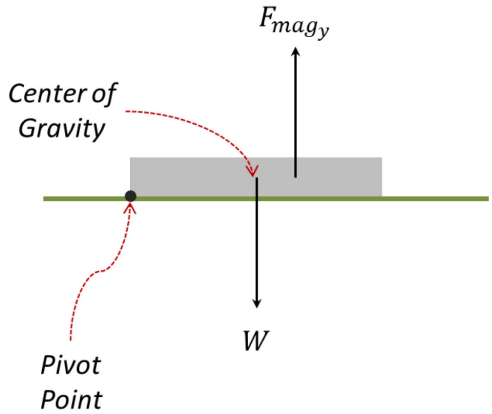

Figure 25. Free body diagram showing major forces acting on particle

As given in the figure, when the equilibrium point is exceeded where the torque formed by the component of magnetic force acting in y-direction overcomes the torque due to the weight of the particle, rotation around the pivot point starts; assuming that friction is high enough to prevent any slipping of the particle on the belt surface. Based on this observation, the exact location of where the lift-off will start can be calculated using the derived formula. For this calculation, a resultant magnetic force in y-direction and its precise location within the particle need to be determined.

Calculation of the resultant force acting on the particle is trivial as it will be a sum of all the forces acting on each strip in y-direction. As all forces are acting in the same direction, an arithmetic sum is enough to determine the magnitude of the resultant force.

Determining the location of where the resultant force will act can be accomplished by summing up all the moments created by the forces at the pivot point and dividing this value by the magnitude of the resultant force already calculated in the previous step.

Once resultant force and its location are found, the equilibrium condition can be written as a constraint to Excel's Solver analysis tool to find the x_{actual} value, which would later be converted to d_{true} based on the geometric relations developed. The spreadsheet is used for different sized particles at varying rotor speeds of the magnetic element and contains the eddy current, strip area and force calculations based on the slicing method.

4.7. Comparison of Experimental versus Calculated Results

The lift-off locations determined by the experiments and by the calculations based on derived formula are presented for comparison in Figure 26 to 30 below. Solid lines show the curves obtained by calculations whereas the dotted curves show the results obtained from the analysis of slow motion videos shot during experiments.

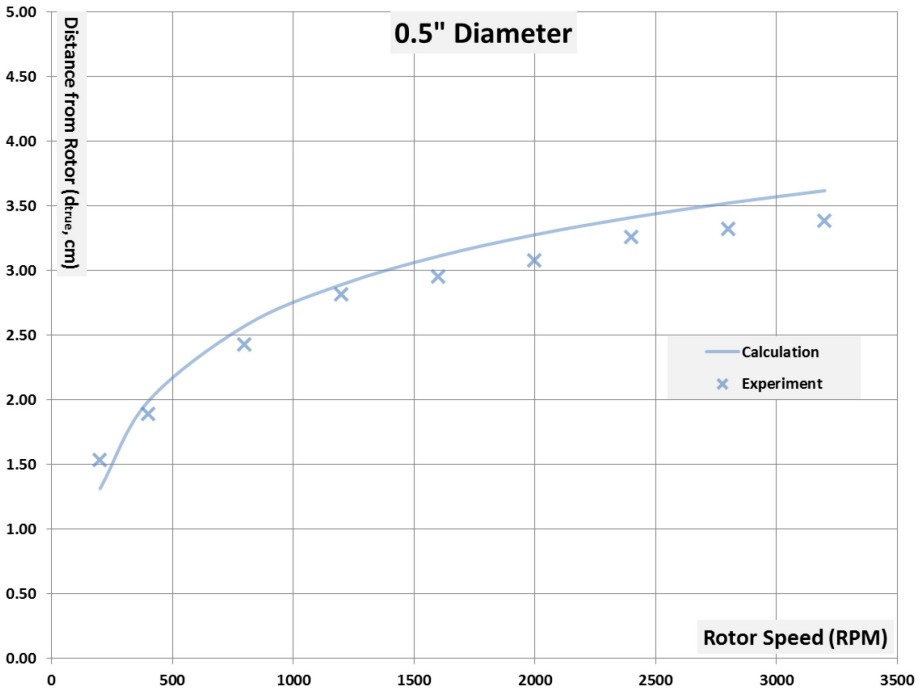

Figure 26. Comparison of calculated vs experimental lift-off location for 0.5" diameter particle

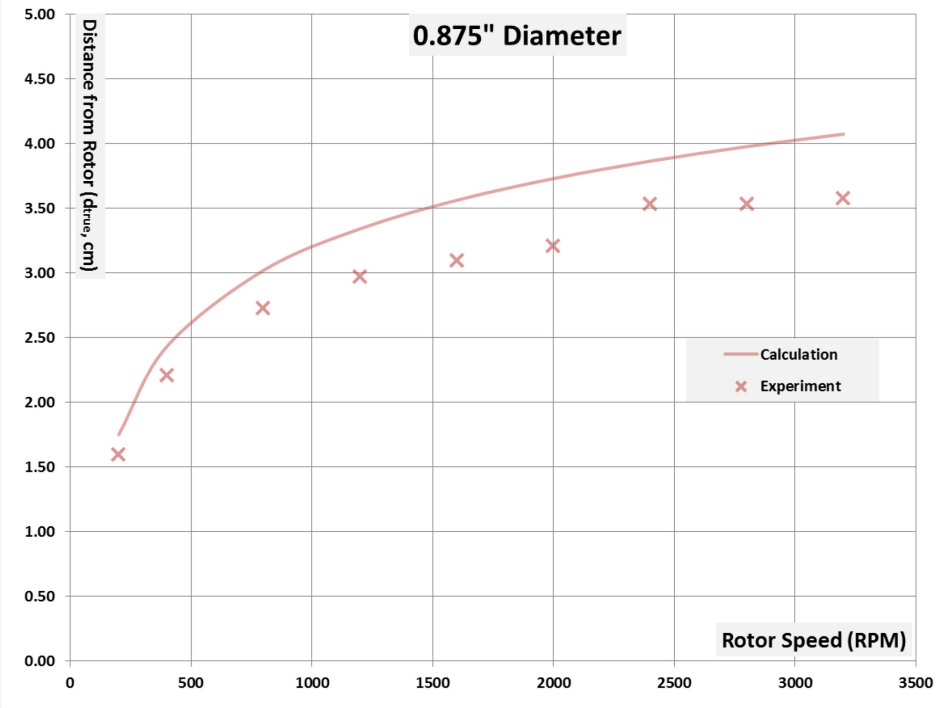

Figure 27. Comparison of calculated vs experimental lift-off location for 0.875" diameter particle

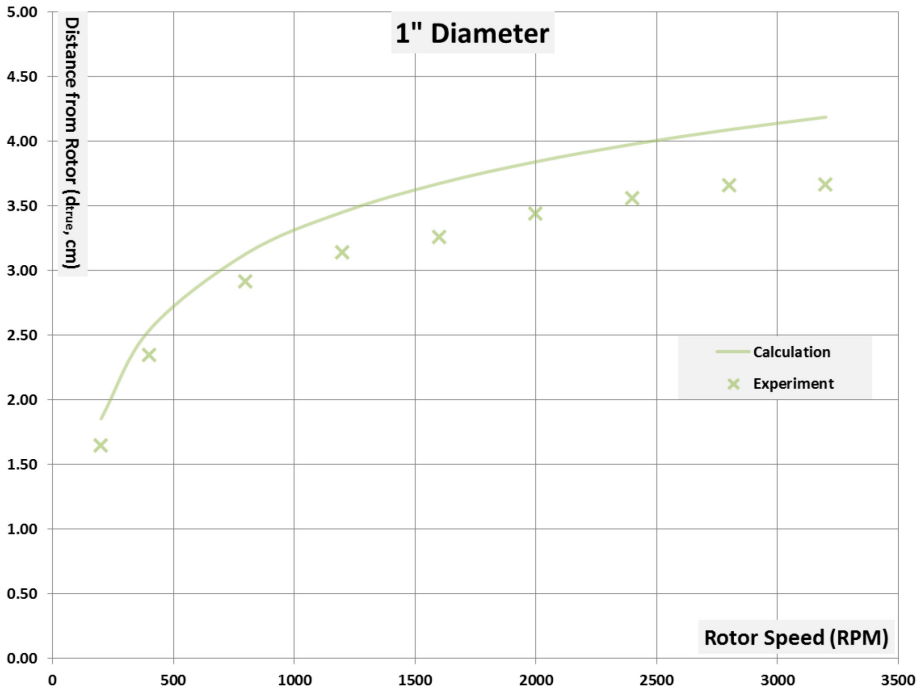

Figure 28. Comparison of calculated vs experimental lift-off location for 1" diameter particle

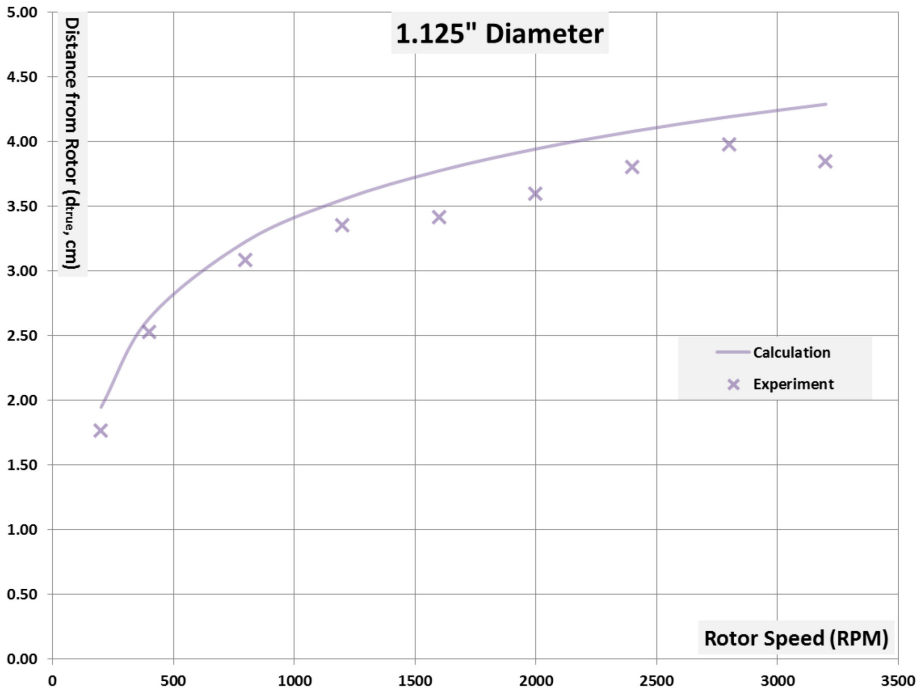

Figure 29. Comparison of calculated vs experimental lift-off location for 1.125" diameter particle

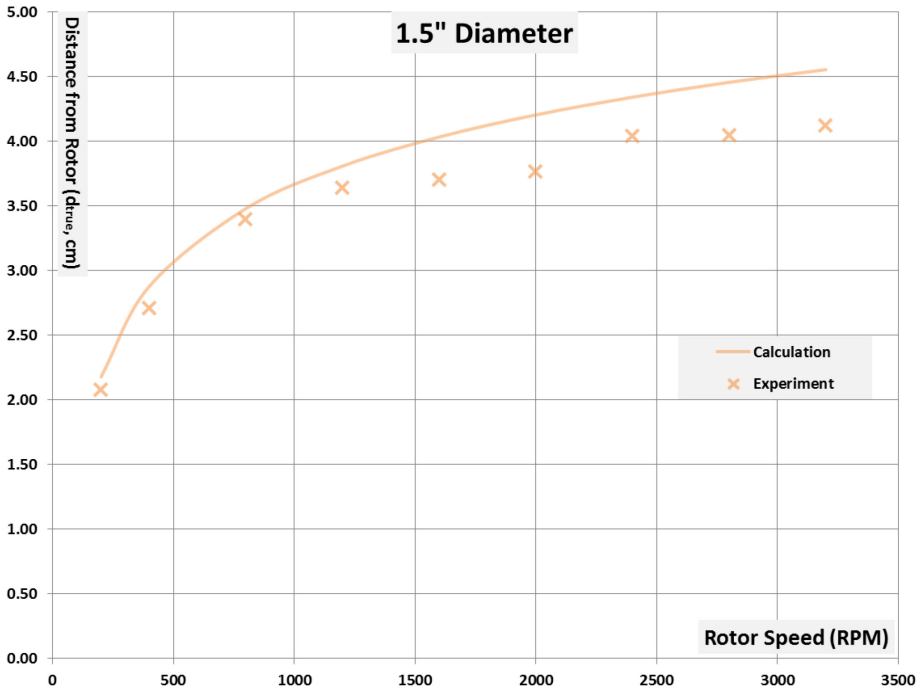

Figure 30. Comparison of calculated vs experimental lift-off location for 1.5" diameter particle

When the results presented in the figures above are compared, it is visible that a high level correlation is achieved though there are differences between the values at higher rotor speeds.

This is an expected situation due to these facts:

i) The particle experiences a magnetic force acting in x-direction by which it is pulled. Especially at higher rotor speeds, before the lift-off, the magnitude of force in x-direction is enough to overcome friction and particle starts slipping on the belt surface and accelerates towards the rotor. Thus, the lift-off location is observed closer to rotor in the experiments.

ii) The method of determining the lift-off location was to check for the change in appearance of the shadow of the particle cast on the belt. For any change to be observed, the particle has to be lifted off from the belt considerably, which would also lead to an observation of a location closer to the rotor.

It can be concluded that the novel method developed and the new magnetic force formula derived is accurate for use in calculations.

5. SIMULATOR FOR EDDY CURRENT SEPARATOR

Although the concept of force calculation developed in Chapter 4 is a major finding by its own, in order for it to find practical use, a model is need to simulate the trajectories of different particles at different rotor speeds so that the separation process can be defined in detail. Having such a model is important for the efficiently operating existing units based on quantitative facts as well as being a highly valuable tool for research to better understand key operating parameters in detail so that existing designs can be improved or new designs can be introduced.

In this chapter, steps taken to build this novel simulator in MS Excel together with its working principles will be examined in detail. A comparison of the results obtained from the newly developed simulator will be compared with the experimental data gathered will also be presented in the closing section.

5.1. Working Principle

The model is built around a dynamic force balance that calculates the net force in x and y-directions at time steps of 0.0005 seconds for a duration of 0.25 seconds starting from zero. At time equals zero seconds, the particle starts its travel on the belt, at belt speed, from the exact location where video capturing started during the experiments. Based on the net forces acting on the particle, a calculation is carried out to find the acceleration of the particle using Newton's Second Law of Motion. Once acceleration is found, velocity and displacement are calculated in order to determine the position of the particle for calculations at the next time step.

Although this is a very straightforward and simple approach, especially for the cases when forces acting on the particle are constant and uniform, it is a quite powerful tool. During the separation process in an eddy current separator, calculations become complicated due to the fact that magnetic force from the magnetic element will produce a variable force as the location and orientation of the particle changes. Thus, the magnetic force acting on the particle should be calculated at each time step for accuracy. And as the novel method of calculating the magnetic force on the particle depends on treating the particle as a group of wires, force on each wire has to be found using the new formula derived in Chapter 4.

In order to accomplish the above stated tasks, the program uses a routine that was newly created for this purpose by Visual Basic for Applications (VBA) code, to transfer location and orientation data of the particle, for each time step, to a module where the developed magnetic force calculations in Chapter 4 are employed. The same routine is used to transfer the results back to the main program from this module, in order to input the components of the resultant magnetic force in x and y-direction for calculation of the net forces at that particular time step.

While carrying out the magnetic force calculations in the respective module, some modifications were made to the formula that was derived in Chapter 4. These additions were made in order to take into account situations where a contribution from both the x and y components of the magnetic field act on the EMF generated on the strips. This is a requirement when the particle is in rotation as its orientation is not parallel to neither of the axes. Neglecting it will result in under estimation of the trajectory since the current cannot be calculated accurately.

As mentioned above, since one has to take into account the rotation of the particle, when torque acting on the particle needs to be calculated, work with forces that are perpendicular (i.e. act as a force that causes rotation through the moment arm). In order to calculate these, a rotation matrix was used to convert forces in x and y directions to obtain the net resultant force y' direction.

As the location data is calculated and recorded by the main routine, now the path followed by the particle during the simulation can be plotted in x-y coordinate system to obtain its trajectory together with its lift-off location. Thus, now, with this novel methodology, the simulator can predict the trajectories of different sized particles at any rotational speed of the magnetic element. This is a major breakthrough as the simulator only uses physical data and no empirical derivations or assumptions.

Some screenshot from the main routine and force calculation modules are presented in the figures below.

Parameters			
Symbol	**Definition**	**Value**	**Unit**
v_i	Belt Speed	**1.00**	m/sec
g	Gravitational Acceleration	9.81	m/sec2
ρ_{air}	Density Air	1.20	kg/m3
$\rho_{particle}$	Density Particle	2700.00	kg/m3
σ	Conductivity	2.66E+07	
-	Particle Shape	Disc	-
D	Particle Diameter	**1.500**	**in**
r	Particle Radius	0.019050	m
h	Particle Thickness	**0.003175**	**m**
C_{drag}	Drag Coefficient	1.1	-
A_{drag}	Drag Area	1.14E-03	m2
A	Particle Area	1.14E-03	m2
$V_{particle}$	Particle Volume	3.62E-06	m3
m	Particle Mass	9.77E-03	kg
I_{CM}	Mmt of Inertia (Center of Mass)	8.87E-07	kgm2
$I_{tangent}$	Mmt of Inertia (Tangent)	4.43E-06	kgm2
t	Time step	**0.0005**	**sec**
D	Start Distance	**0.1932**	**m**
Rotor Speed	Rotational Speed of Mag. Rotor	**6000**	**RPM**
Y_{mag}	Height of Belt Surface	0.1583	m
R_{mag}	Radius of Magnetic Element	0.1485	m
μ_{static}	Coef. Of Static Fric. (Belt)	1.10	-
μ_{dyn}	Coef. Of Dynamic Fric. (Belt)	0.80	-

Table 1. Input Parameters for the developed simulator

Table 1 above shows the input dialog for parameters used in the simulator developed. The parameters in bold and dark blue in color are the ones that were changed during simulations although the simulator can handle changes in other parameters too.

In Figure 31, a screenshot is provided showing the results of calculations on different parameters within the main routine for a selected number of time steps. It is not possible to display all the time steps as the number is quite big for each calculation. From left to right, columns designated for time steps, coordinates of the center of gravity and its orientation, velocities in respective axis directions, components of different forces contributing to translational and rotational motions, as well as constraints to check the behavior of particle.

	A	B	C	D	E	F	G	H	I	J	K	L	M	N	O	P	Q	R	S	T	U	V	W	X	Y	Z	AA	AB	
29		0	1	2	3	4	5	6	7	8	9	10	11	12	13	14	15	16	17	18	19	20	21	22	23	24	25	26	
30	Time	Position of CG			Angle	Linear Velocity		Force friction		Force drag		Force mar	Force magnetic		F net (Translational)		Velocity		Δ Displacement		F mag	r mmt	Torque	α	ω	Δβ	Airborne	End of	Rot
31		X cmr	Y cmr	d cmr	β	x	y	Static	Dynamic	x	y	y	x	y	x	y	x	y	x	y	y'	y'	τ	(rad/s²)	(rad/s)	(deg)	Check	Belt	Cl
32	0.0000	-0.1932	0.1599	0.1023	0.00	1.0000	0.0000	1.05E-01	7.66E-02	0.00E+00	0.00E+00	-9.59E-02	1.57E-04	1.38E-04	0.00E+00	0.00E+00	1.00E+00	0.00E+00	5.00E-04	0.00E+00	1.38E-04	5.49E-03	0.00E+00	0.00E+00	0.00E+00	0.00	0	0	
33	0.0005	-0.1927	0.1599	0.1019	0.00	1.0000	0.0000	1.05E-01	7.66E-02	0.00E+00	0.00E+00	-9.59E-02	1.64E-04	1.45E-04	0.00E+00	0.00E+00	1.00E+00	0.00E+00	5.00E-04	0.00E+00	1.45E-04	5.48E-03	0.00E+00	0.00E+00	0.00E+00	0.00	0	0	
34	0.0010	-0.1922	0.1599	0.1015	0.00	1.0000	0.0000	1.05E-01	7.66E-02	0.00E+00	0.00E+00	-9.59E-02	1.72E-04	1.52E-04	0.00E+00	0.00E+00	1.00E+00	0.00E+00	5.00E-04	0.00E+00	1.52E-04	5.48E-03	0.00E+00	0.00E+00	0.00E+00	0.00	0	0	
35	0.0015	-0.1917	0.1599	0.1011	0.00	1.0000	0.0000	1.05E-01	7.66E-02	0.00E+00	0.00E+00	-9.59E-02	1.81E-04	1.60E-04	0.00E+00	0.00E+00	1.00E+00	0.00E+00	5.00E-04	0.00E+00	1.60E-04	5.47E-03	0.00E+00	0.00E+00	0.00E+00	0.00	0	0	
36	0.0020	-0.1912	0.1599	0.1007	0.00	1.0000	0.0000	1.05E-01	7.66E-02	0.00E+00	0.00E+00	-9.59E-02	1.89E-04	1.68E-04	0.00E+00	0.00E+00	1.00E+00	0.00E+00	5.00E-04	0.00E+00	1.68E-04	5.47E-03	0.00E+00	0.00E+00	0.00E+00	0.00	0	0	
37	0.0025	-0.1907	0.1599	0.1004	0.00	1.0000	0.0000	1.05E-01	7.66E-02	0.00E+00	0.00E+00	-9.59E-02	1.99E-04	1.76E-04	0.00E+00	0.00E+00	1.00E+00	0.00E+00	5.00E-04	0.00E+00	1.76E-04	5.46E-03	0.00E+00	0.00E+00	0.00E+00	0.00	0	0	
38	0.0030	-0.1902	0.1599	0.1000	0.00	1.0000	0.0000	1.05E-01	7.66E-02	0.00E+00	0.00E+00	-9.59E-02	2.08E-04	1.85E-04	0.00E+00	0.00E+00	1.00E+00	0.00E+00	5.00E-04	0.00E+00	1.85E-04	5.45E-03	0.00E+00	0.00E+00	0.00E+00	0.00	0	0	
39	0.0035	-0.1897	0.1599	0.0996	0.00	1.0000	0.0000	1.05E-01	7.65E-02	0.00E+00	0.00E+00	-9.59E-02	2.18E-04	1.94E-04	0.00E+00	0.00E+00	1.00E+00	0.00E+00	5.00E-04	0.00E+00	1.94E-04	5.45E-03	0.00E+00	0.00E+00	0.00E+00	0.00	0	0	
40	0.0040	-0.1892	0.1599	0.0992	0.00	1.0000	0.0000	1.05E-01	7.65E-02	0.00E+00	0.00E+00	-9.59E-02	2.28E-04	2.04E-04	0.00E+00	0.00E+00	1.00E+00	0.00E+00	5.00E-04	0.00E+00	2.04E-04	5.44E-03	0.00E+00	0.00E+00	0.00E+00	0.00	0	0	
41	0.0045	-0.1887	0.1599	0.0988	0.00	1.0000	0.0000	1.05E-01	7.65E-02	0.00E+00	0.00E+00	-9.59E-02	2.39E-04	2.14E-04	0.00E+00	0.00E+00	1.00E+00	0.00E+00	5.00E-04	0.00E+00	2.14E-04	5.44E-03	0.00E+00	0.00E+00	0.00E+00	0.00	0	0	
42	0.0050	-0.1882	0.1599	0.0984	0.00	1.0000	0.0000	1.05E-01	7.65E-02	0.00E+00	0.00E+00	-9.59E-02	2.51E-04	2.24E-04	0.00E+00	0.00E+00	1.00E+00	0.00E+00	5.00E-04	0.00E+00	2.24E-04	5.43E-03	0.00E+00	0.00E+00	0.00E+00	0.00	0	0	
43	0.0055	-0.1877	0.1599	0.0981	0.00	1.0000	0.0000	1.05E-01	7.65E-02	0.00E+00	0.00E+00	-9.59E-02	2.63E-04	2.35E-04	0.00E+00	0.00E+00	1.00E+00	0.00E+00	5.00E-04	0.00E+00	2.35E-04	5.43E-03	0.00E+00	0.00E+00	0.00E+00	0.00	0	0	
44	0.0060	-0.1872	0.1599	0.0977	0.00	1.0000	0.0000	1.05E-01	7.65E-02	0.00E+00	0.00E+00	-9.59E-02	2.75E-04	2.47E-04	0.00E+00	0.00E+00	1.00E+00	0.00E+00	5.00E-04	0.00E+00	2.47E-04	5.42E-03	0.00E+00	0.00E+00	0.00E+00	0.00	0	0	
45	0.0065	-0.1867	0.1599	0.0973	0.00	1.0000	0.0000	1.05E-01	7.65E-02	0.00E+00	0.00E+00	-9.59E-02	2.88E-04	2.59E-04	0.00E+00	0.00E+00	1.00E+00	0.00E+00	5.00E-04	0.00E+00	2.59E-04	5.42E-03	0.00E+00	0.00E+00	0.00E+00	0.00	0	0	
46	0.0070	-0.1862	0.1599	0.0969	0.00	1.0000	0.0000	1.05E-01	7.65E-02	0.00E+00	0.00E+00	-9.59E-02	3.02E-04	2.72E-04	0.00E+00	0.00E+00	1.00E+00	0.00E+00	5.00E-04	0.00E+00	2.72E-04	5.41E-03	0.00E+00	0.00E+00	0.00E+00	0.00	0	0	
47	0.0075	-0.1857	0.1599	0.0965	0.00	1.0000	0.0000	1.05E-01	7.65E-02	0.00E+00	0.00E+00	-9.59E-02	3.17E-04	2.85E-04	0.00E+00	0.00E+00	1.00E+00	0.00E+00	5.00E-04	0.00E+00	2.85E-04	5.40E-03	0.00E+00	0.00E+00	0.00E+00	0.00	0	0	
48	0.0080	-0.1852	0.1599	0.0962	0.00	1.0000	0.0000	1.05E-01	7.65E-02	0.00E+00	0.00E+00	-9.59E-02	3.32E-04	2.99E-04	0.00E+00	0.00E+00	1.00E+00	0.00E+00	5.00E-04	0.00E+00	2.99E-04	5.40E-03	0.00E+00	0.00E+00	0.00E+00	0.00	0	0	
49	0.0085	-0.1847	0.1599	0.0958	0.00	1.0000	0.0000	1.05E-01	7.65E-02	0.00E+00	0.00E+00	-9.59E-02	3.47E-04	3.14E-04	0.00E+00	0.00E+00	1.00E+00	0.00E+00	5.00E-04	0.00E+00	3.14E-04	5.39E-03	0.00E+00	0.00E+00	0.00E+00	0.00	0	0	
50	0.0090	-0.1842	0.1599	0.0954	0.00	1.0000	0.0000	1.05E-01	7.64E-02	0.00E+00	0.00E+00	-9.59E-02	3.64E-04	3.29E-04	0.00E+00	0.00E+00	1.00E+00	0.00E+00	5.00E-04	0.00E+00	3.29E-04	5.39E-03	0.00E+00	0.00E+00	0.00E+00	0.00	0	0	
51	0.0095	-0.1837	0.1599	0.0950	0.00	1.0000	0.0000	1.05E-01	7.64E-02	0.00E+00	0.00E+00	-9.59E-02	3.81E-04	3.45E-04	0.00E+00	0.00E+00	1.00E+00	0.00E+00	5.00E-04	0.00E+00	3.45E-04	5.38E-03	0.00E+00	0.00E+00	0.00E+00	0.00	0	0	
52	0.0100	-0.1832	0.1599	0.0947	0.00	1.0000	0.0000	1.05E-01	7.64E-02	0.00E+00	0.00E+00	-9.59E-02	3.99E-04	3.62E-04	0.00E+00	0.00E+00	1.00E+00	0.00E+00	5.00E-04	0.00E+00	3.62E-04	5.38E-03	0.00E+00	0.00E+00	0.00E+00	0.00	0	0	
53	0.0105	-0.1827	0.1599	0.0943	0.00	1.0000	0.0000	1.05E-01	7.64E-02	0.00E+00	0.00E+00	-9.59E-02	4.18E-04	3.79E-04	0.00E+00	0.00E+00	1.00E+00	0.00E+00	5.00E-04	0.00E+00	3.79E-04	5.37E-03	0.00E+00	0.00E+00	0.00E+00	0.00	0	0	
54	0.0110	-0.1822	0.1599	0.0939	0.00	1.0000	0.0000	1.05E-01	7.64E-02	0.00E+00	0.00E+00	-9.59E-02	4.37E-04	3.98E-04	0.00E+00	0.00E+00	1.00E+00	0.00E+00	5.00E-04	0.00E+00	3.98E-04	5.36E-03	0.00E+00	0.00E+00	0.00E+00	0.00	0	0	
55	0.0115	-0.1817	0.1599	0.0935	0.00	1.0000	0.0000	1.05E-01	7.64E-02	0.00E+00	0.00E+00	-9.59E-02	4.58E-04	4.17E-04	0.00E+00	0.00E+00	1.00E+00	0.00E+00	5.00E-04	0.00E+00	4.17E-04	5.36E-03	0.00E+00	0.00E+00	0.00E+00	0.00	0	0	
56	0.0120	-0.1812	0.1599	0.0932	0.00	1.0000	0.0000	1.05E-01	7.64E-02	0.00E+00	0.00E+00	-9.59E-02	4.79E-04	4.37E-04	0.00E+00	0.00E+00	1.00E+00	0.00E+00	5.00E-04	0.00E+00	4.37E-04	5.35E-03	0.00E+00	0.00E+00	0.00E+00	0.00	0	0	
57	0.0125	-0.1807	0.1599	0.0928	0.00	1.0000	0.0000	1.05E-01	7.63E-02	0.00E+00	0.00E+00	-9.59E-02	5.02E-04	4.58E-04	0.00E+00	0.00E+00	1.00E+00	0.00E+00	5.00E-04	0.00E+00	4.58E-04	5.35E-03	0.00E+00	0.00E+00	0.00E+00	0.00	0	0	
58	0.0130	-0.1802	0.1599	0.0924	0.00	1.0000	0.0000	1.05E-01	7.63E-02	0.00E+00	0.00E+00	-9.59E-02	5.25E-04	4.81E-04	0.00E+00	0.00E+00	1.00E+00	0.00E+00	5.00E-04	0.00E+00	4.81E-04	5.34E-03	0.00E+00	0.00E+00	0.00E+00	0.00	0	0	
59	0.0135	-0.1797	0.1599	0.0920	0.00	1.0000	0.0000	1.05E-01	7.63E-02	0.00E+00	0.00E+00	-9.59E-02	5.50E-04	5.04E-04	0.00E+00	0.00E+00	1.00E+00	0.00E+00	5.00E-04	0.00E+00	5.04E-04	5.33E-03	0.00E+00	0.00E+00	0.00E+00	0.00	0	0	
60	0.0140	-0.1792	0.1599	0.0917	0.00	1.0000	0.0000	1.05E-01	7.63E-02	0.00E+00	0.00E+00	-9.59E-02	5.76E-04	5.28E-04	0.00E+00	0.00E+00	1.00E+00	0.00E+00	5.00E-04	0.00E+00	5.28E-04	5.33E-03	0.00E+00	0.00E+00	0.00E+00	0.00	0	0	
61	0.0145	-0.1787	0.1599	0.0913	0.00	1.0000	0.0000	1.05E-01	7.63E-02	0.00E+00	0.00E+00	-9.59E-02	6.02E-04	5.54E-04	0.00E+00	0.00E+00	1.00E+00	0.00E+00	5.00E-04	0.00E+00	5.54E-04	5.32E-03	0.00E+00	0.00E+00	0.00E+00	0.00	0	0	
62	0.0150	-0.1782	0.1599	0.0909	0.00	1.0000	0.0000	1.05E-01	7.62E-02	0.00E+00	0.00E+00	-9.59E-02	6.31E-04	5.80E-04	0.00E+00	0.00E+00	1.00E+00	0.00E+00	5.00E-04	0.00E+00	5.80E-04	5.32E-03	0.00E+00	0.00E+00	0.00E+00	0.00	0	0	
63	0.0155	-0.1777	0.1599	0.0905	0.00	1.0000	0.0000	1.05E-01	7.62E-02	0.00E+00	0.00E+00	-9.59E-02	6.60E-04	6.08E-04	0.00E+00	0.00E+00	1.00E+00	0.00E+00	5.00E-04	0.00E+00	6.08E-04	5.31E-03	0.00E+00	0.00E+00	0.00E+00	0.00	0	0	

Figure 31. A view from the Excel spreadsheet of the Main Routine

	A	B	C	D	E	F	G	H	I	J	K	L	M	N	O	P	Q	R	S	T
1																				
2	Dparticle	1.5	in		Speed	3200	rpm			0.500	1.00									
3	rparticle	0.01905	m		f	52.33	Hz			0.875	1.75									
4	xactual	0.122468	m		h	0.003175	m			1.000	2.00									
5	yactual	0.221214	m		Npoles	22				1.125	2.25									
6	Rmag	0.1485	m		δ	0.01				**1.500**	**3.00**									
7	|B|	0.28	T		SEM	2.53E-03														
8	Bx (max)	0.33	T		By (max)	0.25	T			Solver =>	540									
9	β	0.00	deg		σ	2.66E+07	S/m													
10	sinβ	0.00			cosβ	1.00														
11	nx	66.00	for e^-nd		ny	62.00	for e^-nd													
12	g	9.81	m/sec2		Density	2700	kg/m3													
13	Quotient	0	Q1		Belt Speed	1.00	m/sec													
14																				
15																				
16												*(EMF)*						*Rotation Matrix*		
17	γ (deg)	xloc'	yloc'	d (m)	Bx	By	ΔBx	ΔBy	Astrip	Npoles)·Δ	A Ratio	Ωstrip	Current	Forcey	Forcex	Forcey'	Forcex'	Mmntx	Mmnty	
18	0.33	0.1415	0.2212	0.11411	0.00018	0.00021	0.00035	0.00043	4.76E-11	4.68E-11	4.18E-08	2.51E+00	4.73E-14	8.34E-18	1.01E-17	8.34E-18	1.01E-17	1.18E-18	1.85E-18	
19	0.67	0.1415	0.2212	0.11411	0.00018	0.00021	0.00035	0.00043	3.33E-10	3.28E-10	2.92E-07	3.58E-01	2.32E-12	4.09E-16	4.95E-16	4.09E-16	4.95E-16	5.79E-17	9.04E-17	
20	1.00	0.1415	0.2212	0.11411	0.00018	0.00021	0.00035	0.00043	9.05E-10	8.90E-10	7.94E-07	1.32E-01	1.71E-11	3.01E-15	3.65E-15	3.01E-15	3.65E-15	4.26E-16	6.66E-16	
21	1.33	0.1415	0.2212	0.11411	0.00018	0.00021	0.00035	0.00043	1.76E-09	1.73E-09	1.55E-06	6.77E-02	6.48E-11	1.14E-14	1.38E-14	1.14E-14	1.38E-14	1.62E-15	2.53E-15	
22	1.67	0.1415	0.2212	0.11410	0.00018	0.00021	0.00035	0.00043	2.91E-09	2.86E-09	2.55E-06	4.11E-02	1.76E-10	3.10E-14	3.76E-14	3.10E-14	3.76E-14	4.39E-15	6.87E-15	
23	2.00	0.1415	0.2212	0.11410	0.00018	0.00021	0.00035	0.00043	4.33E-09	4.26E-09	3.80E-06	2.75E-02	3.92E-10	6.91E-14	8.37E-14	6.91E-14	8.37E-14	9.78E-15	1.53E-14	
24	2.33	0.1415	0.2212	0.11410	0.00018	0.00021	0.00035	0.00043	6.05E-09	5.95E-09	5.30E-06	1.97E-02	7.63E-10	1.35E-13	1.63E-13	1.35E-13	1.63E-13	1.90E-14	2.98E-14	
25	2.67	0.1415	0.2212	0.11410	0.00018	0.00021	0.00035	0.00043	8.05E-09	7.91E-09	7.06E-06	1.48E-02	1.35E-09	2.38E-13	2.89E-13	2.38E-13	2.89E-13	3.37E-14	5.27E-14	
26	3.00	0.1415	0.2212	0.11409	0.00018	0.00021	0.00035	0.00043	1.03E-08	1.02E-08	9.06E-06	1.16E-02	2.23E-09	3.93E-13	4.76E-13	3.93E-13	4.76E-13	5.56E-14	8.69E-14	
27	3.33	0.1415	0.2212	0.11409	0.00018	0.00021	0.00035	0.00043	1.29E-08	1.27E-08	1.13E-05	9.25E-03	3.47E-09	6.13E-13	7.42E-13	6.13E-13	7.42E-13	8.67E-14	1.36E-13	

Figure 32. A view from the Excel spreadsheet of the Magnetic Force Calculation Routine

Given in Figure 32 is a screenshot from the sub-routine that is used to calculate the x and y components of the magnetic force based on the novel method described and newly derived equations in Chapter 4. As can be seen, the top portion of the spreadsheet has the properties of the material as well as properties of the magnetic field. Since a particle of 1.5" in diameter is subject to calculations, the ratio of its diameter to 0.5" sized particle is taken and found to be 3. This is done for all particle sizes in order to find the number of slices to cover the angle change from 0 to 180 degrees. For the case of 1.5" particle, 540 slices will be used.

Location of the center of gravity of the particle is extracted from the main routine and inputted here to the values of x_{actual} and y_{actual}, later geometric calculations are carried out to determine the location of each strip in the coordinate system. Based on the location, the magnetic field density is calculated based on the equations derived in Chapter 4. Proceeding with the calculation of EMF, followed by the current density, force acting on each strip is individually found.

Not visible in the figure above is the calculated value and location of the resultant magnetic force components in x and y directions. These are sent back to the main routine for calculating the resultant force.

5.2.1. Types of Motion

When defining the type of motion of the particles, center of gravity of the particle is referenced. Based on this, there are two types of motion: translational and rotational. Translational motion is observed when the center of gravity of the particle changes location in the x-y coordinate system. Rotational motion occurs due to torque acting on the particle as result of the distribution of magnetic force.

Rotational motion can be observed after lifting of the particle off the belt surface starts. If the particle is not slipping, the rotation will be around the pivot point where the particle is in contact with the belt; however, if there is slipping, the particle will have rotation around its center of gravity. These will be examined further in detail in the proceeding sections.

5.2.2. Handling Rotation in Calculations

Once rotation starts, as the orientation of the particle will change, the magnetic force acting on it will be different, which needs to be compensated. For this purpose, rotation matrix was used to perform a rotation by β degrees.

5.2.3. Free Body Diagrams

The diagrams showing the forces acting on the particle at each phase of motion is presented below. It should be noted that the normal force is not presented in the figures as it is not directly used in the programming of the simulator. Instead, constraints were introduced to simulate its effect in the calculations.

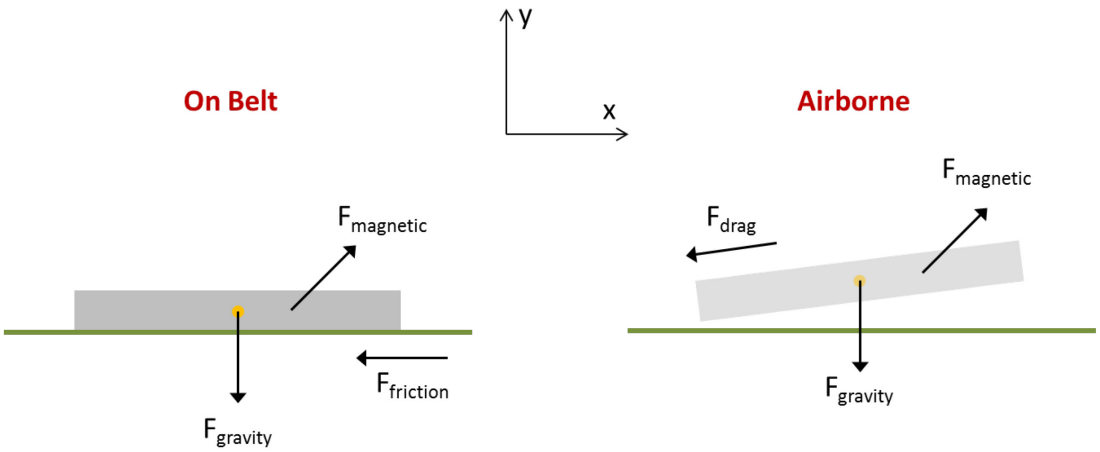

Figure 33. Free Body Diagrams for Translational Motion

Figure 31 shows the forces that are considered to be acting on the particle when it is on belt (left) and when it is airborne (right) at its translational motion state. At the instance the particle becomes airborne, force due to friction between the belt and particle is replaced by the air drag. Drag force is introduced into calculations in such manner that it always acts in the opposite direction of travel both in x and y-directions. Coefficient of drag is chosen to represent a disc, with a value of 1.1 though once rotation starts, it is expected that a higher drag will be observed by the particle.

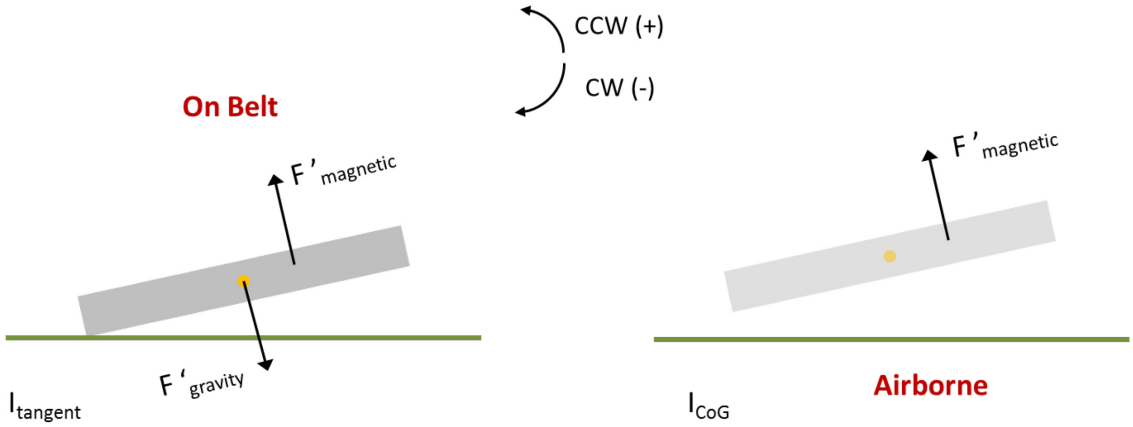

Figure 34. Free Body Diagrams for Rotational Motion

In Figure 32, forces acting on the particle during rotational phase of motion are given. Once the particle becomes airborne, the only force creating torque will be due to magnetic force.

5.2.4. Equations

Equations used during calculations within the simulation are presented below.

5.2.4.1. Translational Motion

Linear Acceleration : $\frac{F_{net}}{m} = a$

Linear Velocity : $\vartheta_2 = \vartheta_1 + a\Delta t$

Linear Displacement : $\Delta s = \frac{(\vartheta_1 + \vartheta_2)}{2}\Delta t$

5.2.4.2. Rotational Motion

Angular Acceleration : $\frac{\tau}{I} = \alpha$

Angular Velocity : $\omega_2 = \omega_1 + \alpha\Delta t$

Angular Displacement : $\Delta\beta = \frac{(\omega_1 + \omega_2)}{2}\Delta t$

5.2.4.3. Moment of Inertia

Rotation at Pivot Point : $I_{tangent} = \frac{5}{4} m {r_{particle}}^2$

Rotation at Center of Gravity : $I_{CoG} = \frac{1}{4} m {r_{particle}}^2$

5.2.5. Constraints

In order to simulate the path taken by the particle as real and as precise as possible, the following constraints were introduced into the simulation:

i. When the magnetic force component in x-direction has a value greater than the value of force applied to the particle by static friction, sliding occurs and frictional force is switched to use of dynamic friction
ii. Rotation, or lift-off, of the particle starts when τ_{net} is positive; i.e. when the moment due to the component of magnetic force in positive y-direction exceeds the moment due to weight of the particle in the negative y-direction
iii. Particle is considered airborne (i.e. free of any belt contact) when the value of its center of gravity coordinate in y-axis is greater than the value of $(Y_{mag} + r_{particle})$

Item (iii) is an over estimation for the particle to be airborne since particle can theoretically be airborne whenever its center of gravity is higher than belt. However, as rotation of the particle is inevitable due to torque from magnetic force, particle can be free of belt contact only when it can rotate freely around its center of gravity meaning, its center of gravity needs to be higher than the belt at least by its radius.

5.3. Results

Trajectories obtained from the simulation are plotted together with the experimental data collected during tests. It should be noted that experimental data is a derived form based on size calculations and its precision is not perfect. In addition, the coefficients of static and dynamic friction of the belt surface against aluminum discs are approximated as it was not possible to determine these values experimentally. Thus, for determination of the values, lift-off locations were taken as a cursor; when good correlation between simulation and experiments were reached; those values were used for all tests and particles.

5.3.1. Simulation vs Experiment Comparison for 0.5” Diameter Particles

General trend obtained with simulation correlates well with experimental results though it can be observed that simulation projects a higher path for the particle at lower rotational speeds. Considering error in measurements, fit can be considered as good.

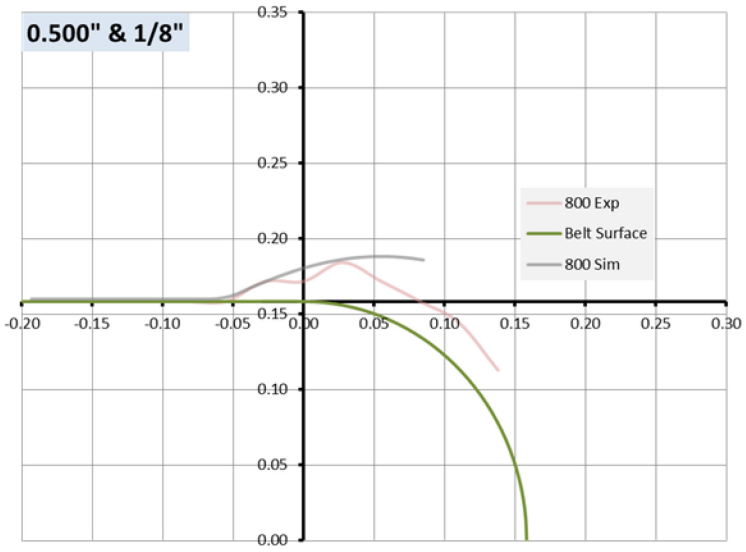

Figure 35. Results of Simulation and Experiments for 0.5” Particle at 800 RPM

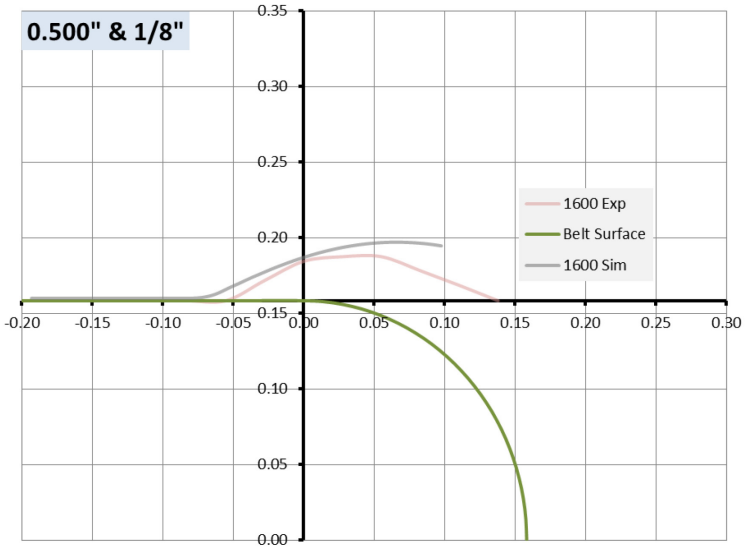

Figure 36. Results of Simulation and Experiments for 0.5” Particle at 1600 RPM

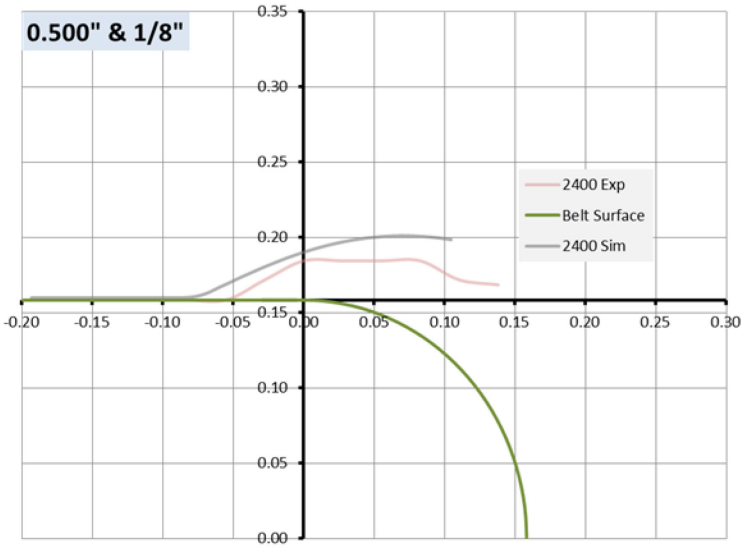

Figure 37. Results of Simulation and Experiments for 0.5" Particle at 2400 RPM

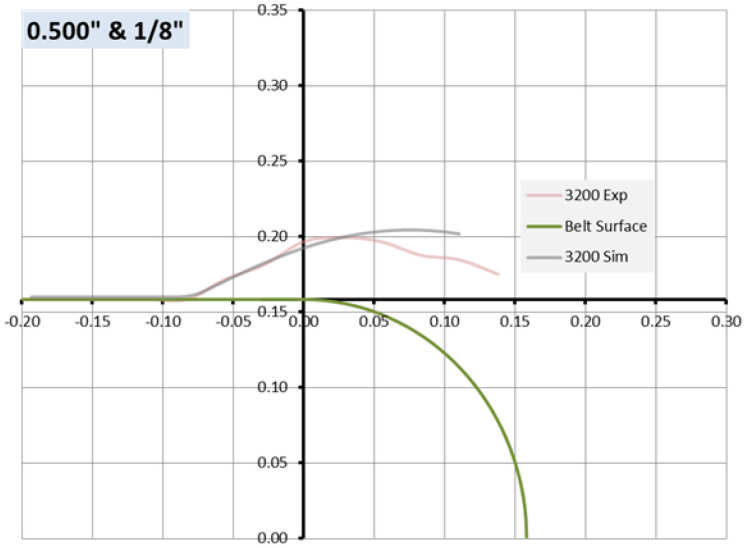

Figure 38. Results of Simulation and Experiments for 0.5" Particle at 3200 RPM

5.3.2. Simulation vs Experiment Comparison for 0.875” Diameter Particles

The trend observed in experiments is quite similar to results of the simulations, though higher trajectory paths were predicted by the simulator. If the locations are where paths cross x-axis are examined, it can be observed that correlations is very good.

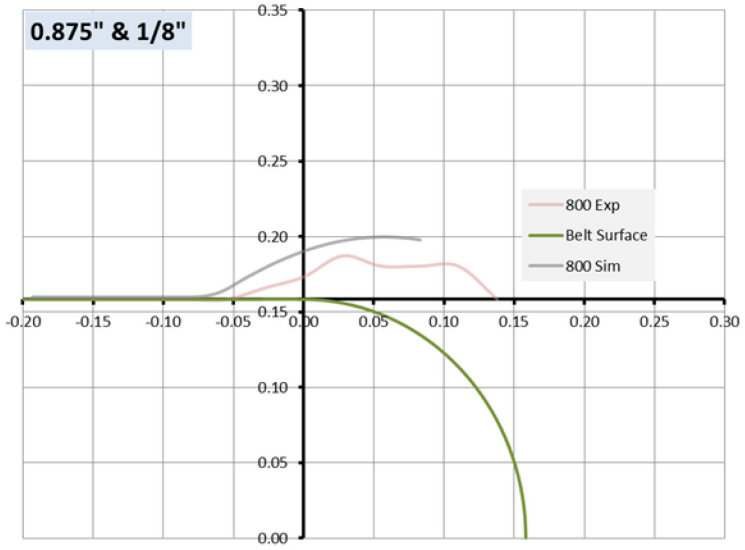

Figure 39. Results of Simulation and Experiments for 0.875” Particle at 800 RPM

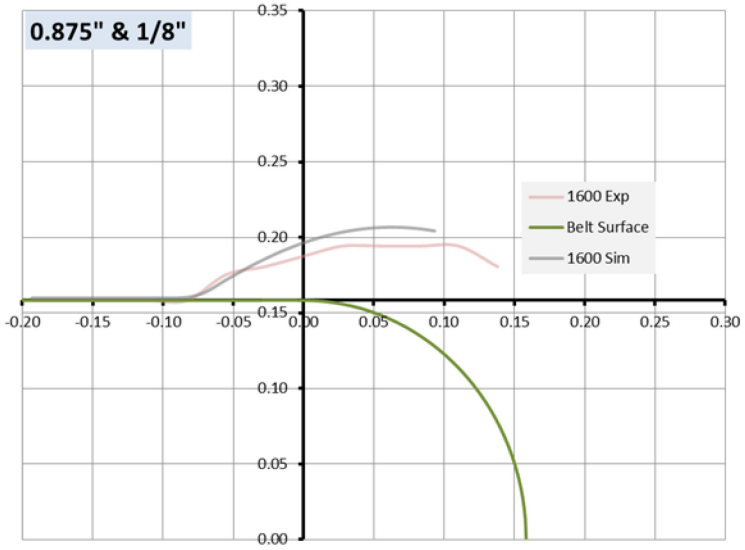

Figure 40. Results of Simulation and Experiments for 0.875” Particle at 1600 RPM

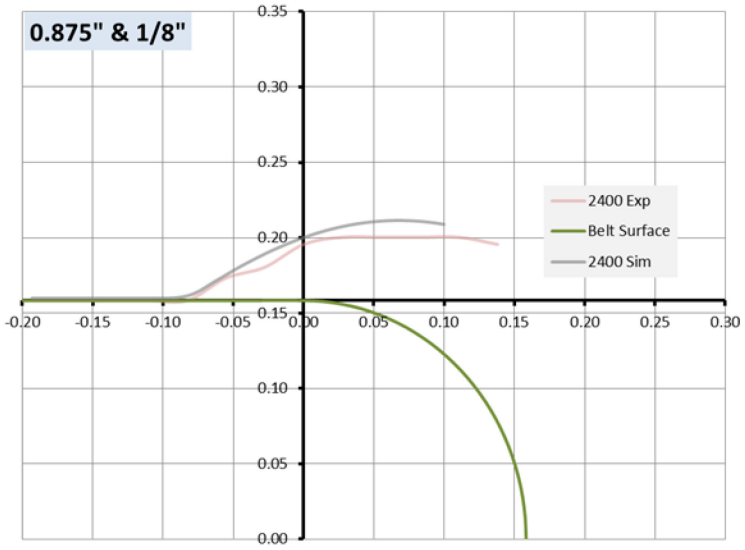

Figure 41. Results of Simulation and Experiments for 0.875" Particle at 2400 RPM

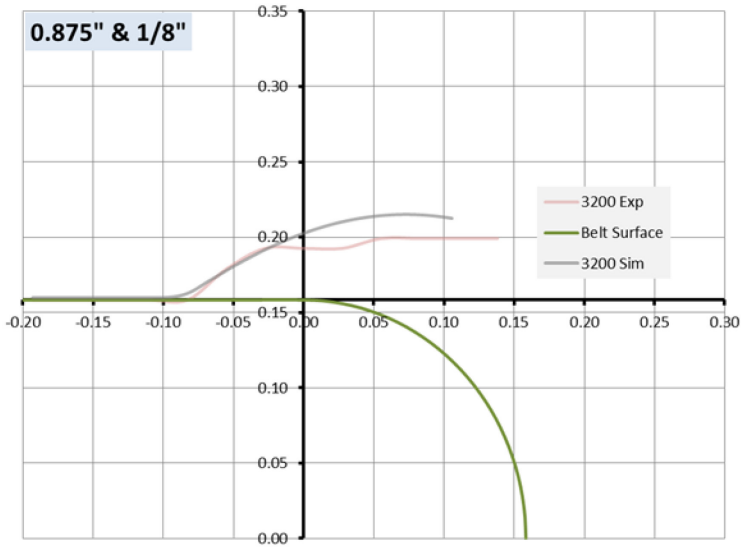

Figure 42. Results of Simulation and Experiments for 0.875" Particle at 3200 RPM

5.3.3. Simulation vs Experiment Comparison for 1” Diameter Particles

Apart from the difference in results at 800 rpm, the set of data for this particle size shows excellent overlap with the simulation results.

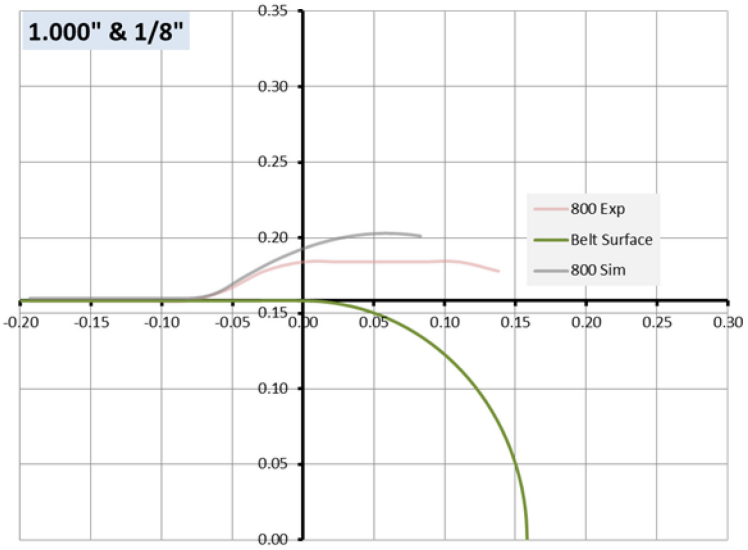

Figure 43. Results of Simulation and Experiments for 1” Particle at 800 RPM

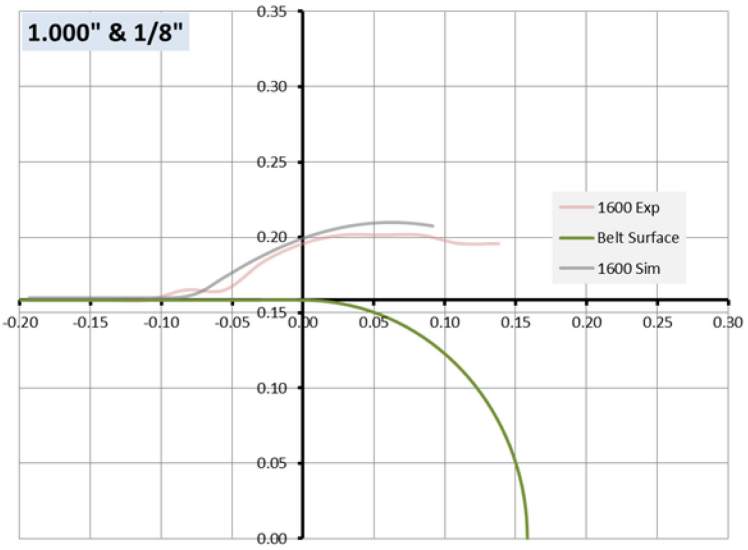

Figure 44. Results of Simulation and Experiments for 1” Particle at 1600 RPM

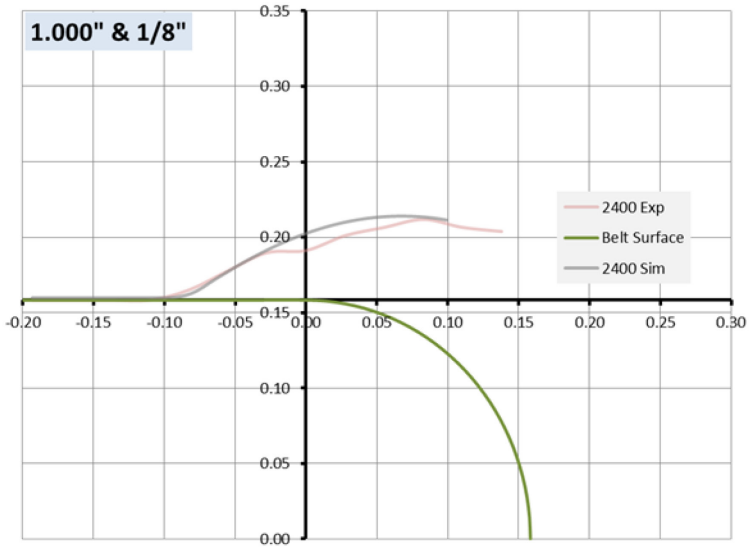

Figure 45. Results of Simulation and Experiments for 1" Particle at 2400 RPM

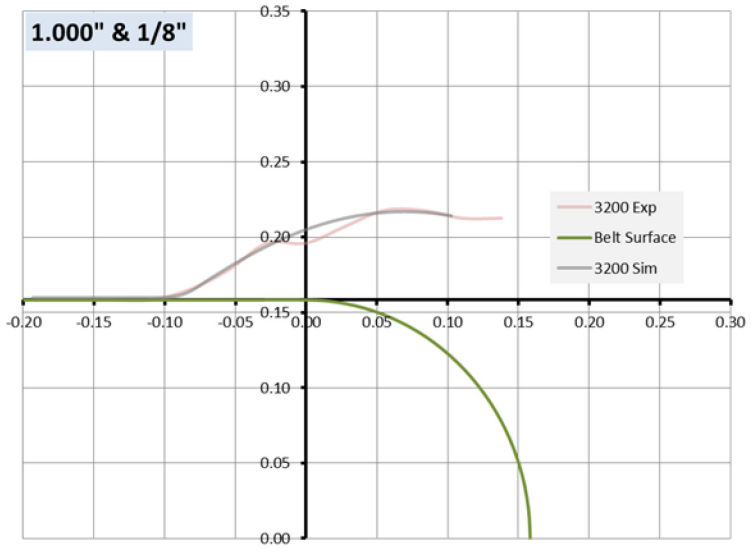

Figure 46. Results of Simulation and Experiments for 1" Particle at 3200 RPM

5.3.4. Simulation vs Experiment Comparison for 1.125” Diameter Particles

Comparison of simulated trajectory with actual paths deducted from experiments show a high degree of match for this particle size; lift-off locations and future landing points all show good agreement with each other.

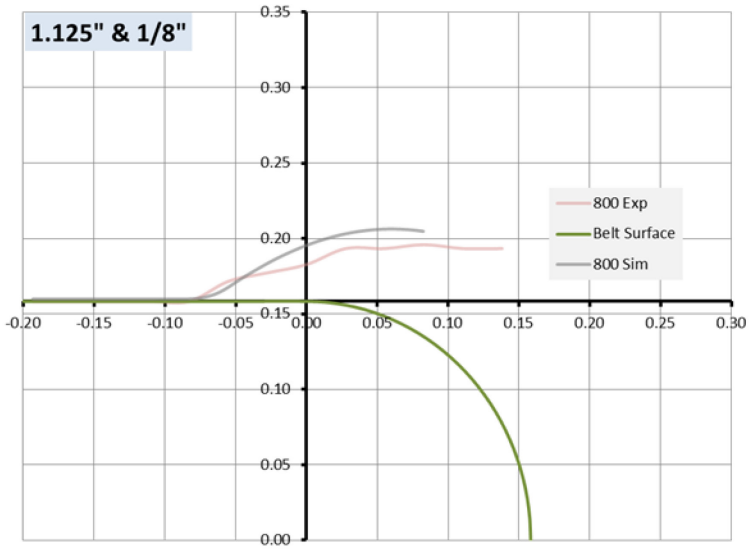

Figure 47. Results of Simulation and Experiments for 1.125” Particle at 800 RPM

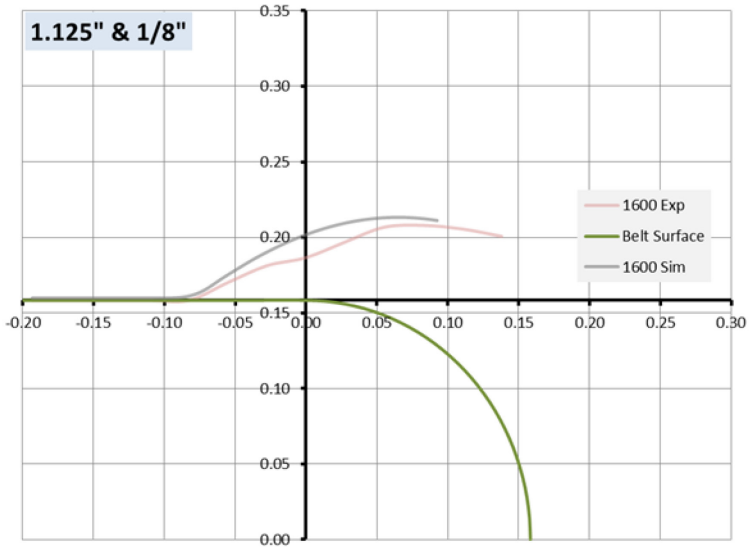

Figure 48. Results of Simulation and Experiments for 1.125” Particle at 1600 RPM

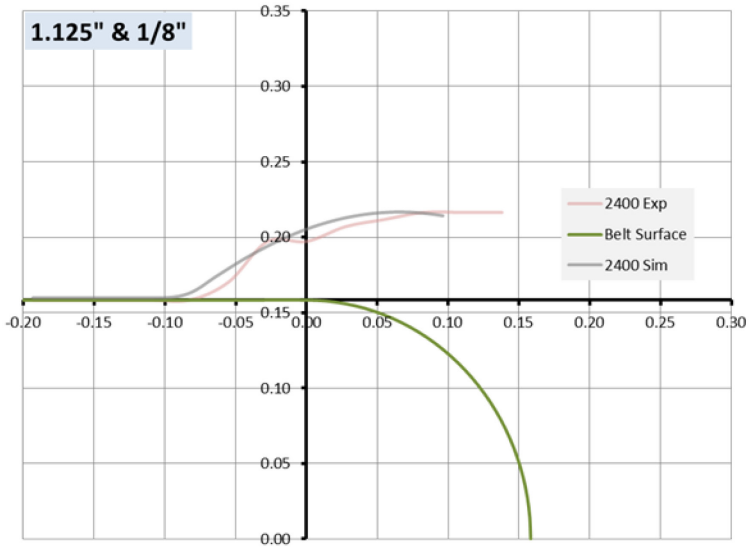

Figure 49. Results of Simulation and Experiments for 1.125" Particle at 2400 RPM

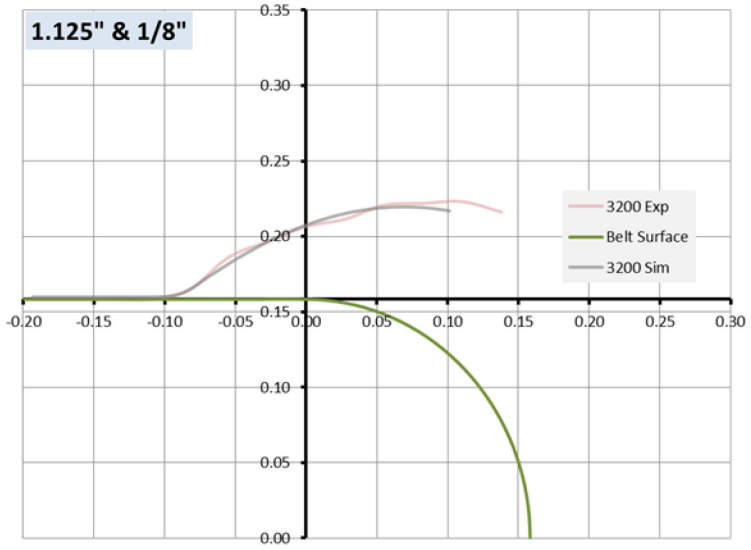

Figure 50. Results of Simulation and Experiments for 1.125" Particle at 3200 RPM

5.3.5. Simulation vs Experiment Comparison for 1.5” Diameter Particles

Contrary to the results obtained for smaller sizes, for this particle, simulation predicts a lower trajectory path compared to the experimental results. The exact match in lift-off locations suggest that this is an error in size measurement during data acquisition, which can be explained by the particle coming out of focus since it gains considerable height and blurred edges making size appear bigger than it really is.

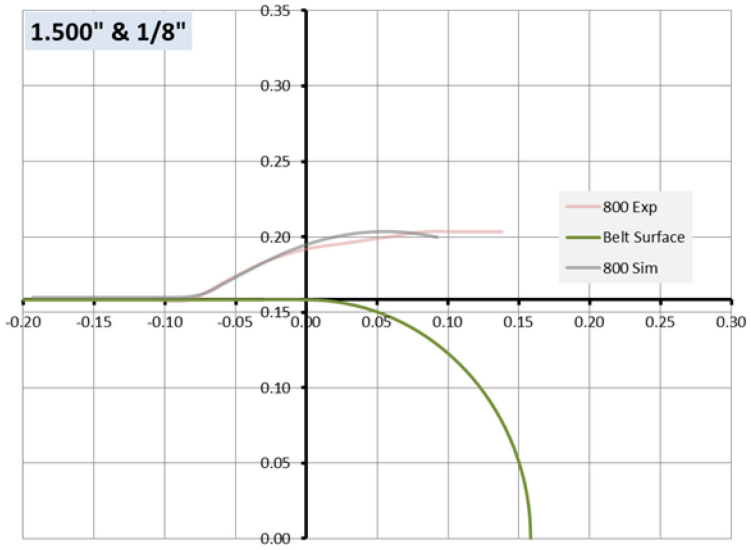

Figure 51. Results of Simulation and Experiments for 1.5” Particle at 800 RPM

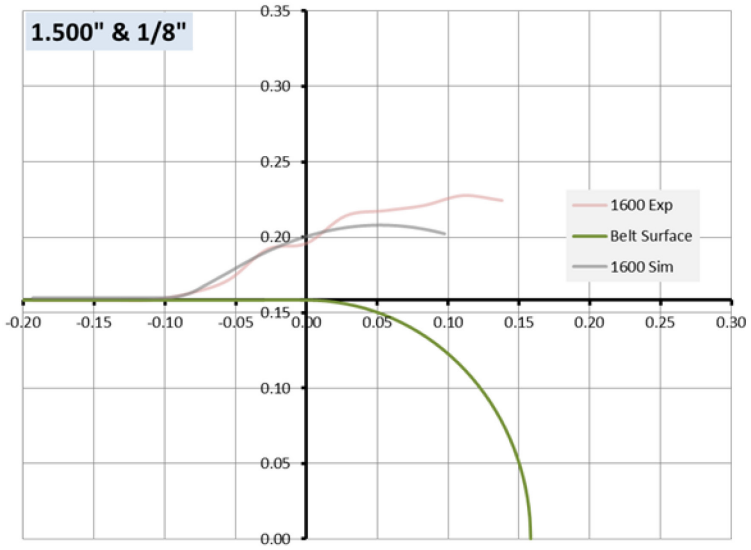

Figure 52. Results of Simulation and Experiments for 1.5" Particle at 1600 RPM

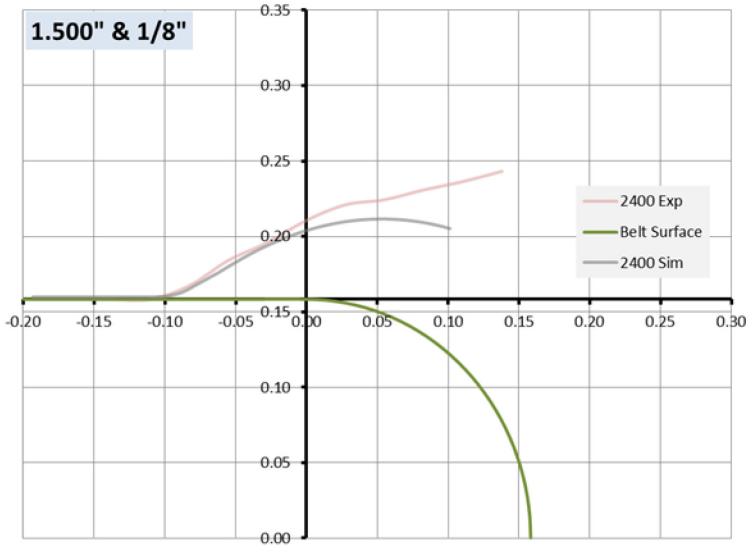

Figure 53. Results of Simulation and Experiments for 1.5" Particle at 2400 RPM

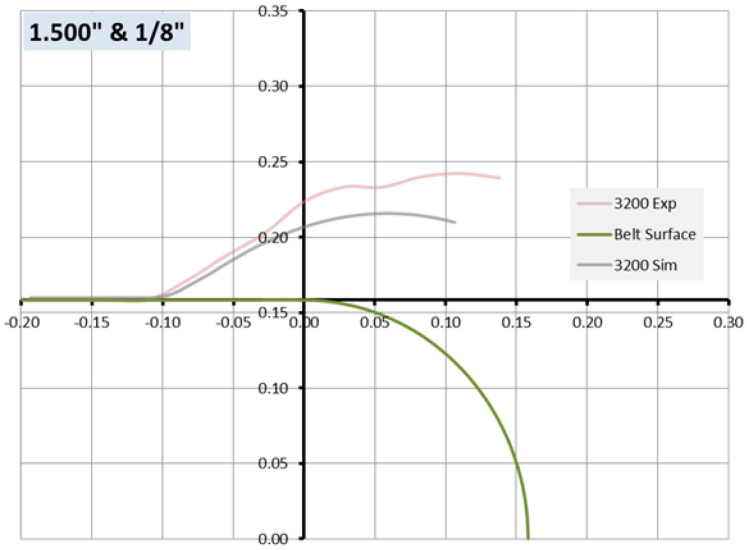

Figure 54. Results of Simulation and Experiments for 1.5" Particle at 3200 RPM

Overall, the level of correlation between the trajectory predicted by the simulation and paths formed by analysis of experimental size change data is quite high indicating that simulator is working to reflect real life conditions.

6. CONCLUSIONS AND CONTRIBUTIONS

In order to model the behavior of an eddy current separator, interaction of many elements with each other and with the magnetic field need to be considered. Any calculation in the field of electromagnetics is an elaborate task, even when static conditions are considered. This becomes an even more involved task when one needs to perform such calculations within the dynamic nature of eddy current separators. Traditionally, simplifications and various assumptions have been utilized in order to generate a model. Instead of simplifications that limit applicability of the technique only to special cases (e.g. a narrow size range) and empirical input, the novel method developed in this dissertation provides a general and fundamental solution.

A novel method was developed that is used to model the behavior of eddy current separators based on intrinsic parameters of the particle such as size, shape and orientation, as well as operational parameters of the eddy current separator like belt speed and rotational speed of the magnetic element. Such a model requires accurate calculations of magnetic force through identification of the effect of relative parameters in mathematical terms.

New equations built on fundamental laws such as Faraday's Law, Lenz's Law and Ohm's Law were derived to calculate the magnetic force. Having the equations to define magnetic force, they were employed to determine the location where the particle would start of lifting off. Results obtained were compared with the experimental findings and very good correlation was realized, proving the validity of derived equations.

Increased accuracy of force calculations made it possible to create a computer simulation that uses dynamic force balancing for determining trajectories of particles. One main routine was linked to different sub-routines through coding in VBA for calculation of magnetic force at each particular time step. With advancing time steps, location and orientation of the particle are determined based on the balance of forces. Using the net force in x and y coordinates, the simulator calculates acceleration, velocity and displacement of the particle with the help of Newton's Laws of Motion. Coordinates for each time step are recorded by the simulator which can be graphed to show the trajectory particle would have followed based on the variables

inputted. Incorporating not only properties of the particle but also operational parameters of the eddy current separator, the simulator is capable of handling different scenarios, which is quite valuable for any research activity as well as determining the true state of a separation operation.

In this dissertation, the techniques needed to verify the derived force calculation method and accuracy of the simulator were also developed. This was made possible by making use of high speed imagery in a novel way. A high speed camera was strategically placed on top the belt to capture the motion of particles. Captured images were analyzed individually to gather information about the lift-off location, time of travel and change in height from the belt surface. In order to calculate the change in height, a relation was developed based on the perceived size of the particles in the images which was successfully implemented to form trajectory paths.

Good correlation of experimental data collected with the calculated data generated show that the method developed to calculate magnetic force, simulator employing force calculations and techniques of data acquisition were all very successful. Detailed analysis of the separation process is now made possible. By having such insight as the ones developed in this dissertation provide the opportunity of in depth examination of problems like metal sorting or recovery of finer sizes, both of which have been challenges waiting to be tackled.

Overall, this contribution provides a viable option for reducing the cost of analyzing; optimizing and designing eddy current separators. The tools introduced in this dissertation also provide any user with the flexibility that is necessary for implementation in practical applications.

7. FUTURE WORK

Although the simulator, at its current condition, can successfully predict particle trajectories, for cases when highest level of precision and accuracy are required, the transitional phase of motion starting with the lift-off of particle from the belt till it becomes airborne at a full rotational state needs to be defined more in detail. Such an undertaking will require introduction of advanced physics concepts, which were beyond the scope of this work.

When margin of error in trajectories of particles is required as nil, such data can be acquired employing more than a single high speed camera in order to capture the motion without any constraints such as focus level and distortion. A system of high speed cameras with digital triggers would be able to capture all aspects of the path taken by particle, provided the particle could be followed automatically by the software rather than manual analysis as was the case in this research.

Running experiments with regular geometric shapes such as polygons and irregular shapes prove to be a challenge due to the requirement of a special feeding mechanism, which can place the particle on the moving belt with the desired orientation with an accuracy and precision of 100%. This is of utmost importance since orientation not only effects the distribution of magnetic force on the object, but it also effects how the particle will behave once it lifts off from the belt surface as alignment off the center of gravity for pivot point will give rise to tilting because of the weight of the particle.

BIBLIOGRAPHY

[1] R. F. Testin, "Recovery of Aluminum from Solid Waste," *Water. Air. Soil Pollut.*, vol. 4, no. 2, pp. 155–166, 1975.

[2] E. J. J. Sommer and G. R. Kenny, "An Electromagnetic System for Dry Recovery of Nonferrous Metal from Shredded Municipal Solid Waste," in *Proceedings of the Fourth Mineral Waste Utilization Symposium*, 1974, pp. 77–84.

[3] C. E. Roos, J. P. Barach, F. M. Wells, A. W. Bateman, P. S. Crooke, D. F. Farrar, R. M. Hackett, G. R. Kenny, R. M. Muira, J. M. Lee, D. S. Loebbaka, R. S. Rowe, E. J. Sommer, R. D. Stafford, and M. S. Webster, "Nonferrous Metal Sorting at Vanderbilt University : Final Report to the Solid Waste Management Office, Environmental Protection Agency," Nashville, TN, 1976.

[4] J. M. D. Coey, *Magnetism and Magnetic Materials*, 4th ed. Cambridge: Cambridge University Press, 2010.

[5] D. Hughes, "On an Induction-Currents Balance, and Experimental Researches Made Therewith," in *Proceedings of the Royal Society of London (1854-1905)*, 1879, vol. 29, pp. 56–65.

[6] E. Schloemann, "Separation of nonmagnetic metals from solid waste by permanent magnets. I. Theory," *J. Appl. Phys.*, vol. 46, no. 11, p. 5012, 1975.

[7] E. Schloemann, "Separation of nonmagnetic metals from solid waste by permanent magnets. II. Experiments on circular disks," *J. Appl. Phys.*, vol. 46, p. 5022, 1975.

[8] H. J. L. Van Der Valk, B. C. Braam, and W. L. Dalmijn, "Eddy-current separation by permanent magnets part I: Theory," *Resour. Conserv.*, vol. 12, no. 3–4, pp. 233–252, 1986.

[9] W. L. Dalmijn, W. P. H. Voskuyl, and H. J. Roorda, "Low-Energy Separation of Nonferrous Metals by Eddy-Current Techniques," in *Proceedings of International Recycling Congress, Berlin*, 1979, vol. 2, pp. 930–935.

[10] D. Fletcher, R. Gerber, P. Lawson, and J. Boehm, "Eddy-Current Separation of Non-Ferrous Conductors and Non-Conductors: Theory and Initial Experiments," *IEEE Trans. Magn.*, vol. 27, no. 6, pp. 5375–5377, 1991.

[11] D. Fletcher, R. Gerber, L. Tarrant, and T. Reid, "Experimental Validation and Generalized

Theory of a Single Boundary Eddy-Current Separator Model," *IEEE Trans. Magn.*, vol. 28, no. 5, pp. 2415–2417, 1992.

[12] D. Fletcher, R. Gerber, and T. Reid, "Theory and Experimental Investigation of an Improved Field Boundary Model for a Single Boundary Eddy-Current Separator," *IEEE Trans. Magn.*, vol. 29, no. 6, pp. 3258–3260, 1993.

[13] P. C. Rem, P. a. Leest, and a. J. van den Akker, "A model for eddy current separation," *Int. J. Miner. Process.*, vol. 49, no. 3–4, pp. 193–200, 1997.

[14] P. C. Rem, E. M. Beunder, and A. J. Van Den Akker, "Simulation of eddy-current separators," *IEEE Trans. Magn.*, vol. 34, no. 4 PART 2, pp. 2280–2286, 1998.

[15] S. Zhang, P. C. Rem, and E. Forssberg, "The Investigation of Separability of Particles Smaller Than 5 mm by Eddy Current Separation Technology. Part I: Rotating Type Eddy Current Separators," *Magn. Electr. Sep.*, vol. 9, no. 4, pp. 233–251, 1999.

[16] S. Zhang, E. Forssberg, B. Arvidson, and W. Moss, "Separation mechanisms and criteria of a rotating eddy-current separator operation," *Resour. Conserv. Recycl.*, vol. 25, no. 3–4, pp. 215–232, 1999.

[17] S. Zhang, P. C. Rem, and E. Forssberg, "Particle trajectory simulation of two-drum eddy current separators," *Resour. Conserv. Recycl.*, vol. 26, no. 2, pp. 71–90, 1999.

[18] N. Fraunholcz, P. C. Rem, and P. A. C. M. Haeser, "Dry Magnus separation," *Miner. Eng.*, vol. 15, no. 1–2, pp. 45–51, 2002.

[19] F. Maraspin, P. Bevilacqua, and P. C. Rem, "Modelling the throw of metals and nonmetals in eddy current separations," *Int. J. Miner. Process.*, vol. 73, no. 1, pp. 1–11, 2004.

[20] J. Ruan and Z. Xu, "A new model of repulsive force in eddy current separation for recovering waste toner cartridges," *J. Hazard. Mater.*, vol. 192, no. 1, pp. 307–313, 2011.

[21] J. Ruan and Z. Xu, "Approaches to improve separation efficiency of eddy current separation for recovering aluminum from waste toner cartridges," *Environ. Sci. Technol.*, vol. 46, no. 11, pp. 6214–6221, 2012.

APPENDIX A : VFD Frequency and Rotor Speeds

RPM	Hz
200	3.33 Hz
400	6.67 Hz
800	13.33 Hz
1200	20.00 Hz
1600	26.67 Hz
2000	33.33 Hz
2400	40.00 Hz
2800	46.67 Hz
3200	53.33 Hz
3600	60.00 Hz
4000	66.67 Hz
4400	73.33 Hz

Table A1. Frequencies used in VFDs and corresponding rotational speeds of the magnetic element

APPENDIX B : Time Measurement Results

Measured times are presented in the graphs below for both types of eddy current separators (ECS). The horizontal axis in the graphs shows the speed of the magnetic element in revolutions per minute; the vertical axis shows the total number of frames. One frame has a time length of 1/10000 seconds.

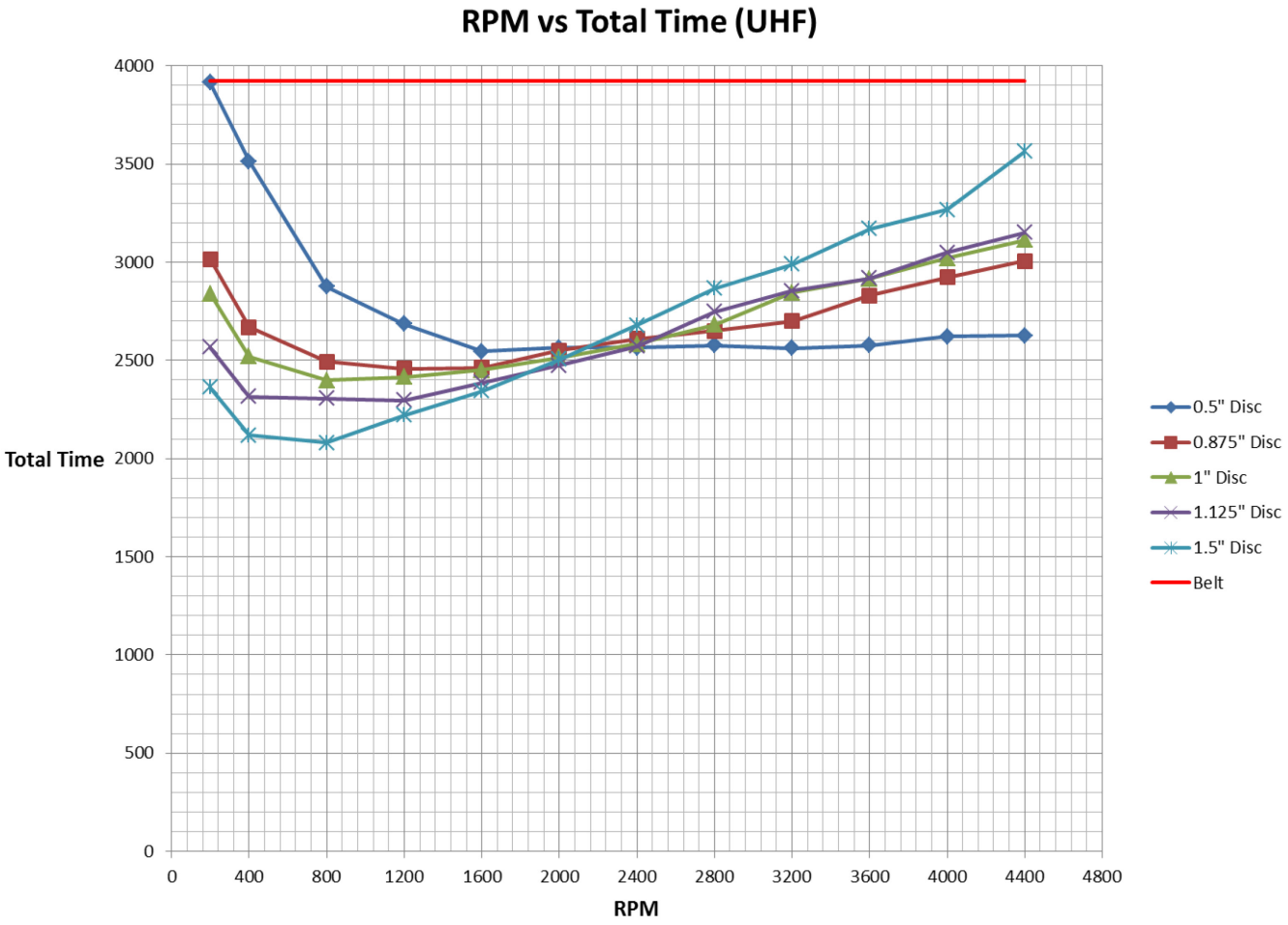

Figure B1. Total travel time for 1/8" thick particles in tests conducted with eccentric type ECS

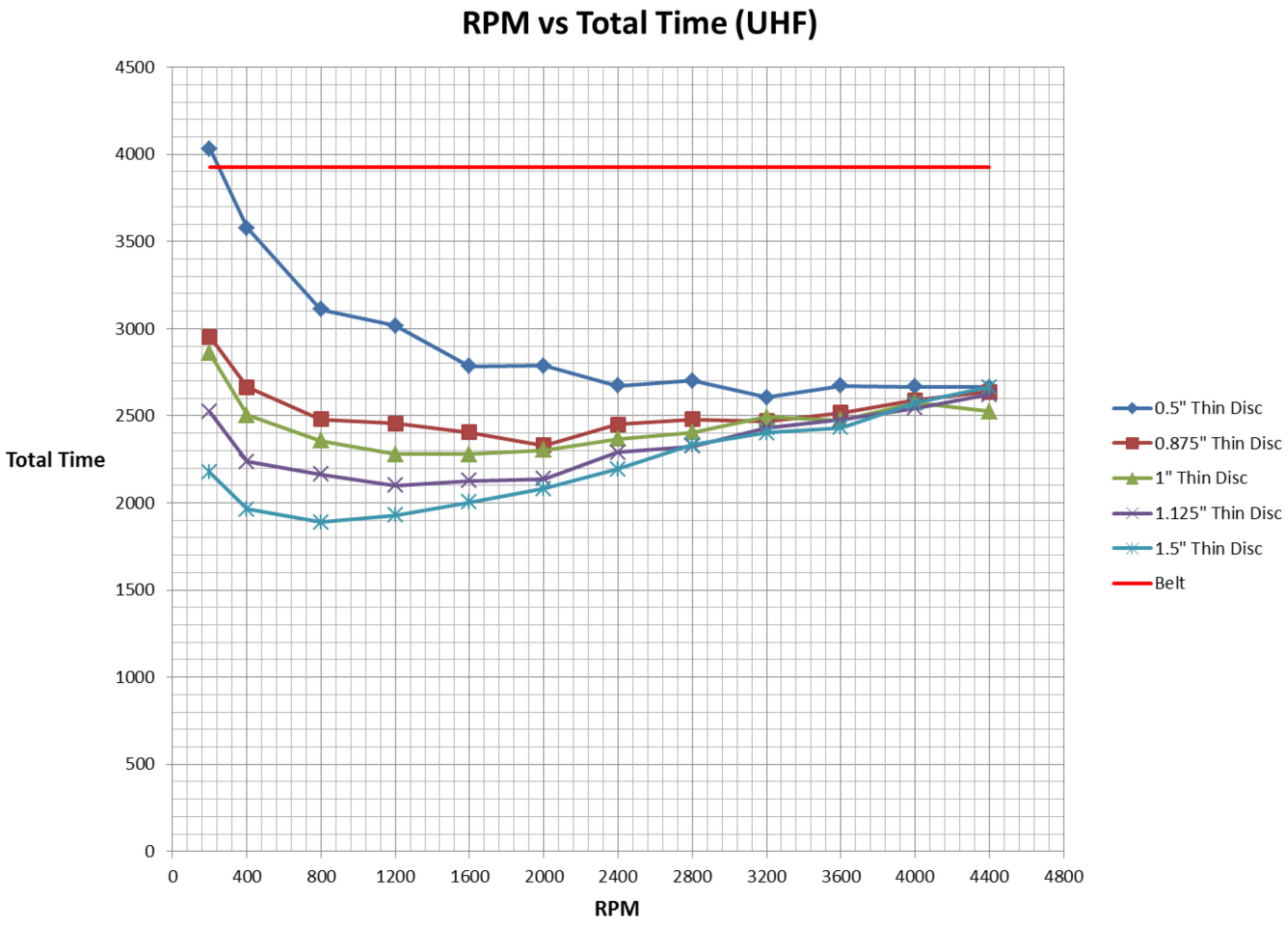

Figure B2. Total travel time for 1/16" thick particles in tests conducted with eccentric type ECS

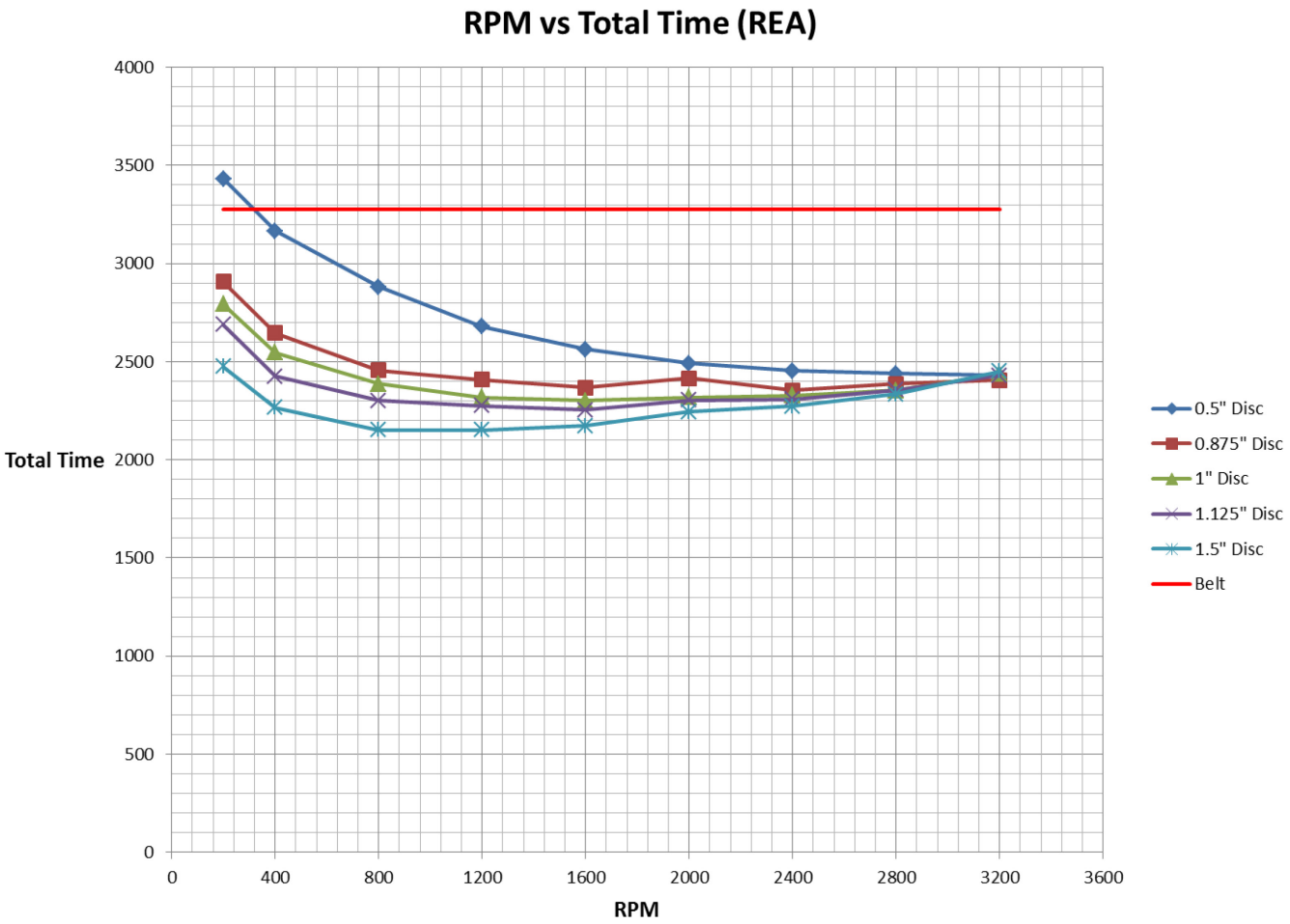

Figure B3. Total travel time for 1/8" thick particles in tests conducted with concentric type ECS

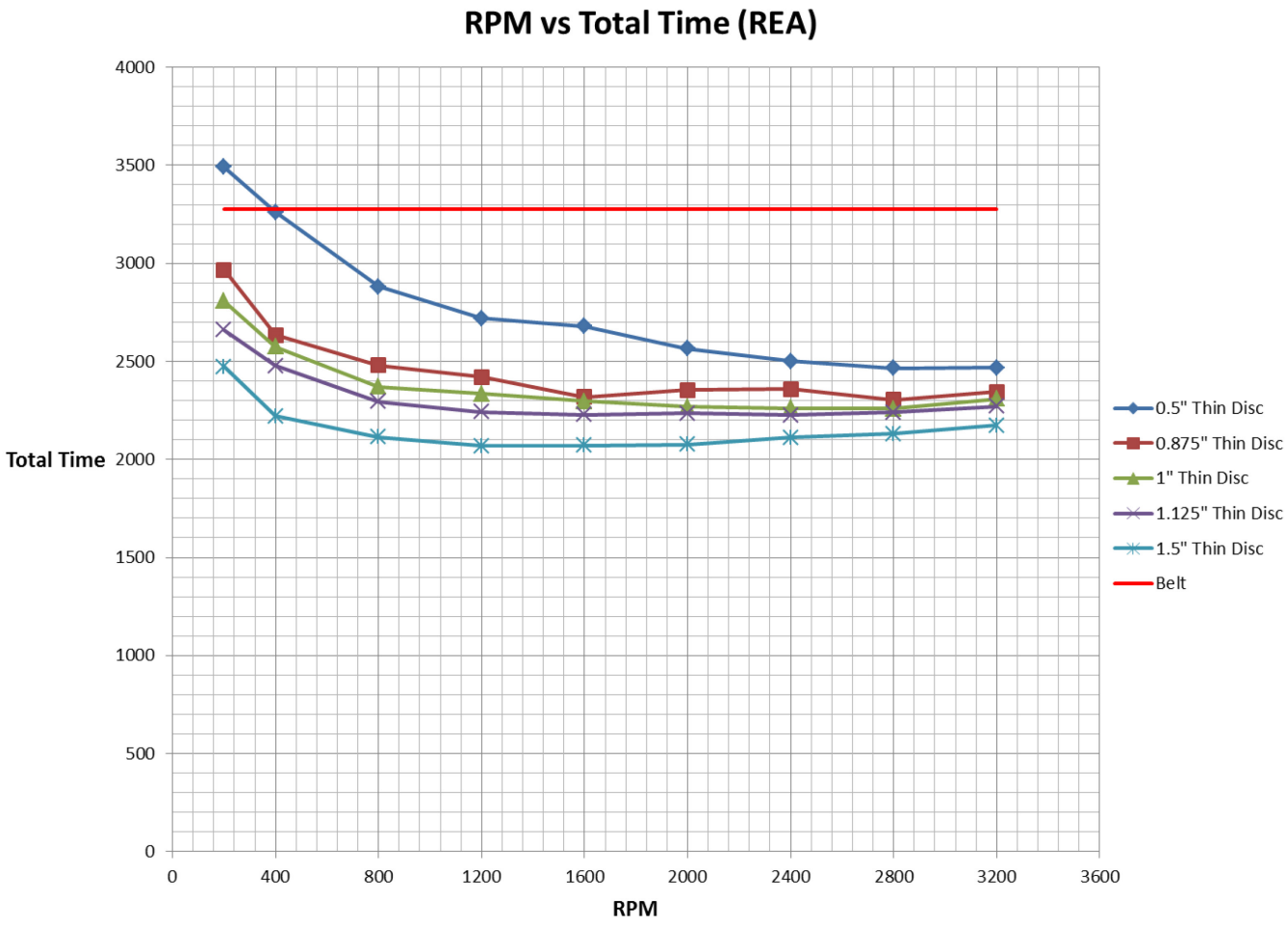

Figure B4. Total travel time for 1/16" thick particles in tests conducted with concentric type ECS

APPENDIX C : Size Change Data

Figures below show the change in the perceived size of the particle in its trajectory due to displacement in y-axis as the rotor speed of the magnetic element is changed. Vertical axis shows the amount of change in percent original size, horizontal axis shows the time in frames. Positive size change shows particle was higher than belt surface and negative change shows particle was lower than belt surface.

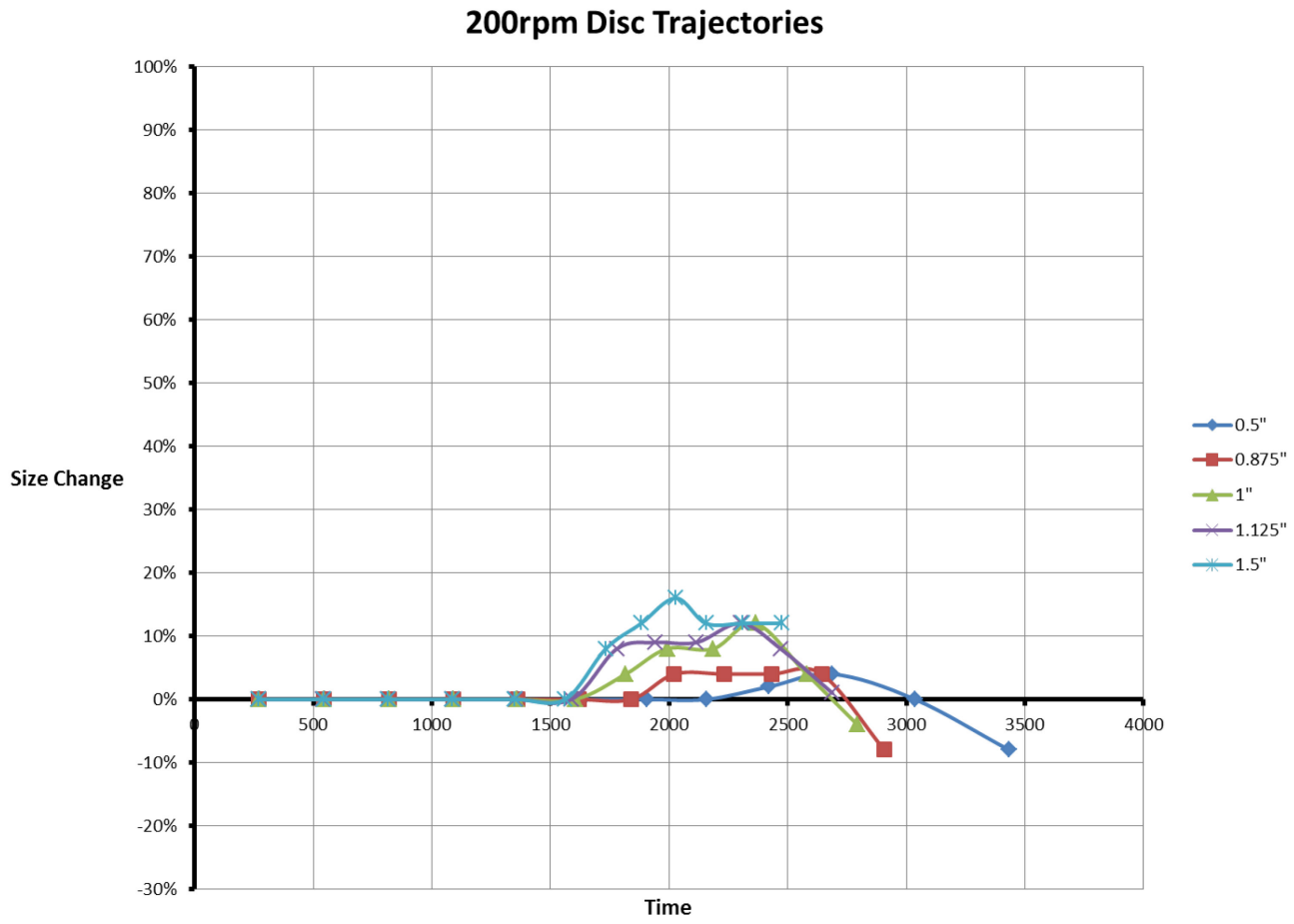

Figure C1. Size change data for 1/8" thick particles in tests conducted with concentric type ECS at 200rpm

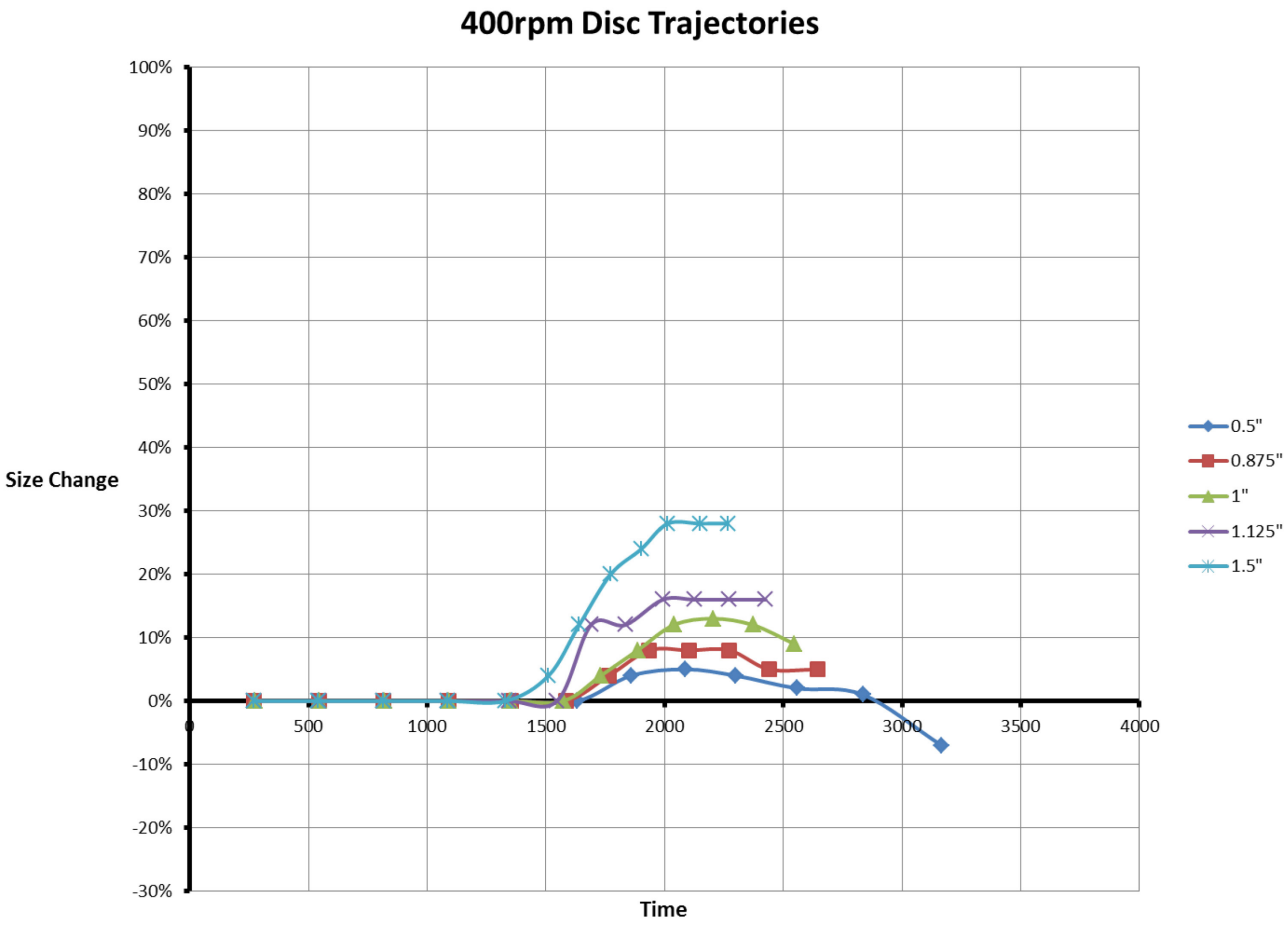

Figure C2. Size change data for 1/8" thick particles in tests conducted with concentric type ECS at 400rpm

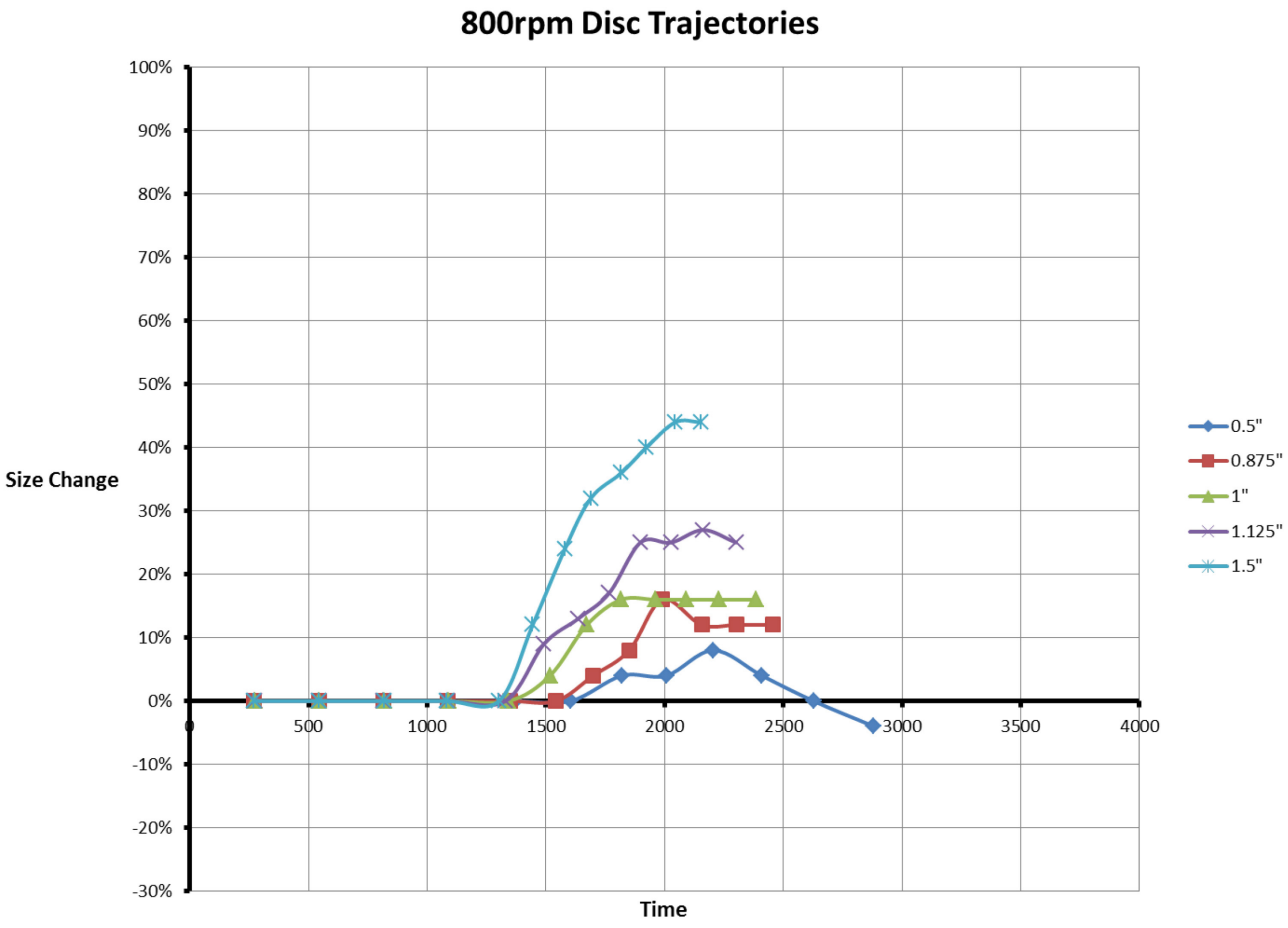

Figure C3. Size change data for 1/8" thick particles in tests conducted with concentric type ECS at 800rpm

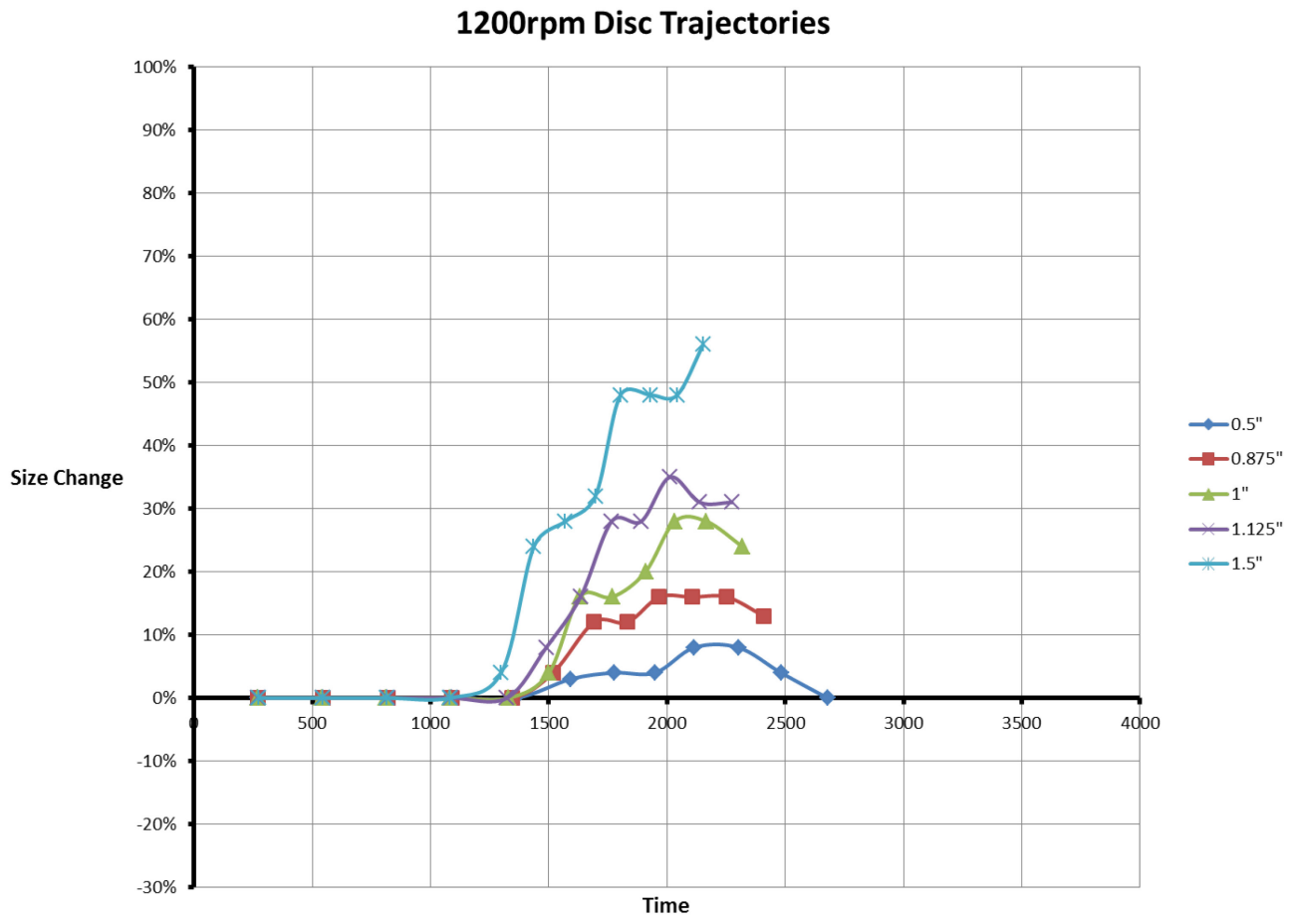

Figure C4. Size change data for 1/8" thick particles in tests conducted with concentric type ECS at 1200rpm

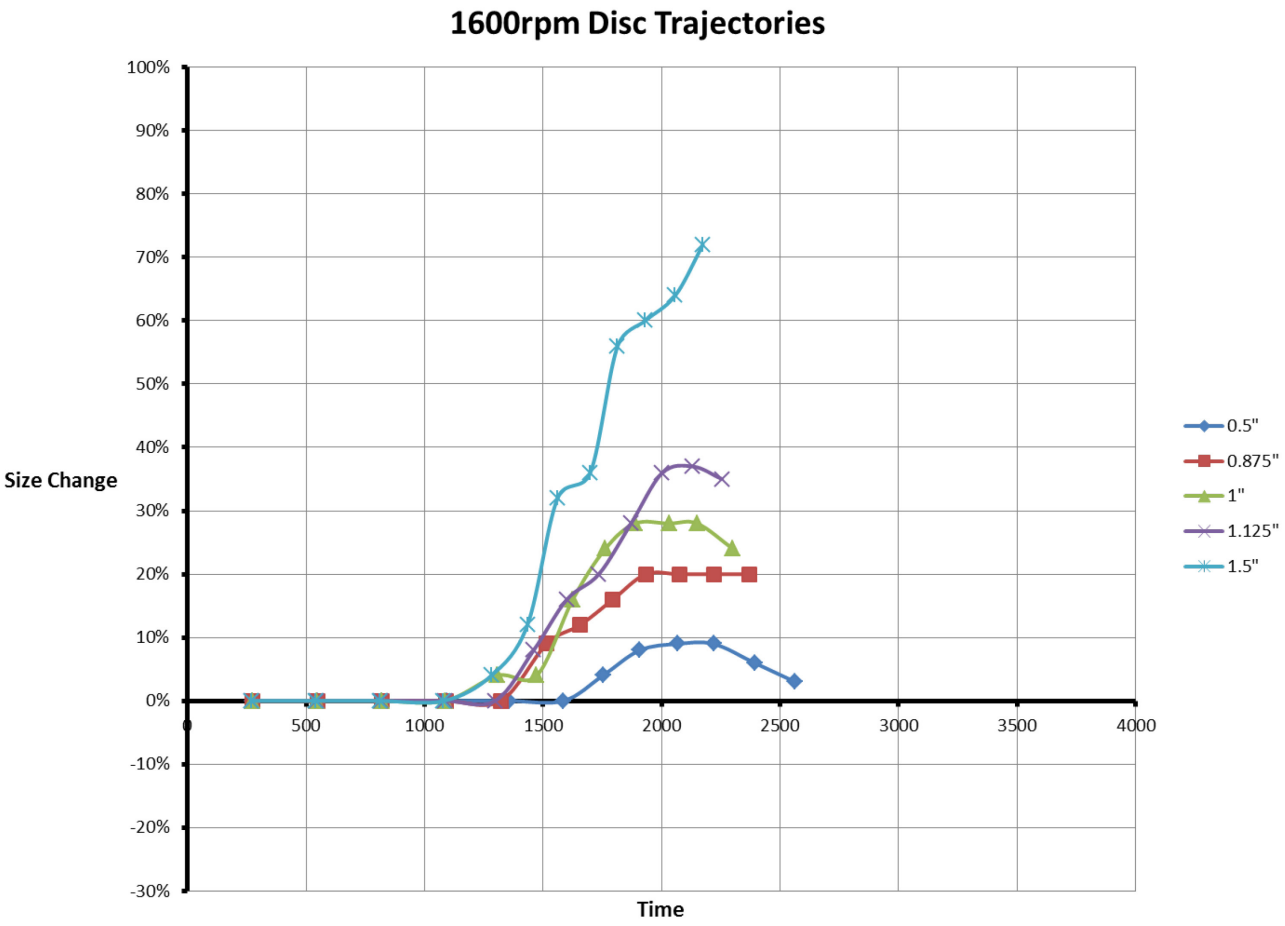

Figure C5. Size change data for 1/8" thick particles in tests conducted with concentric type ECS at 1600rpm

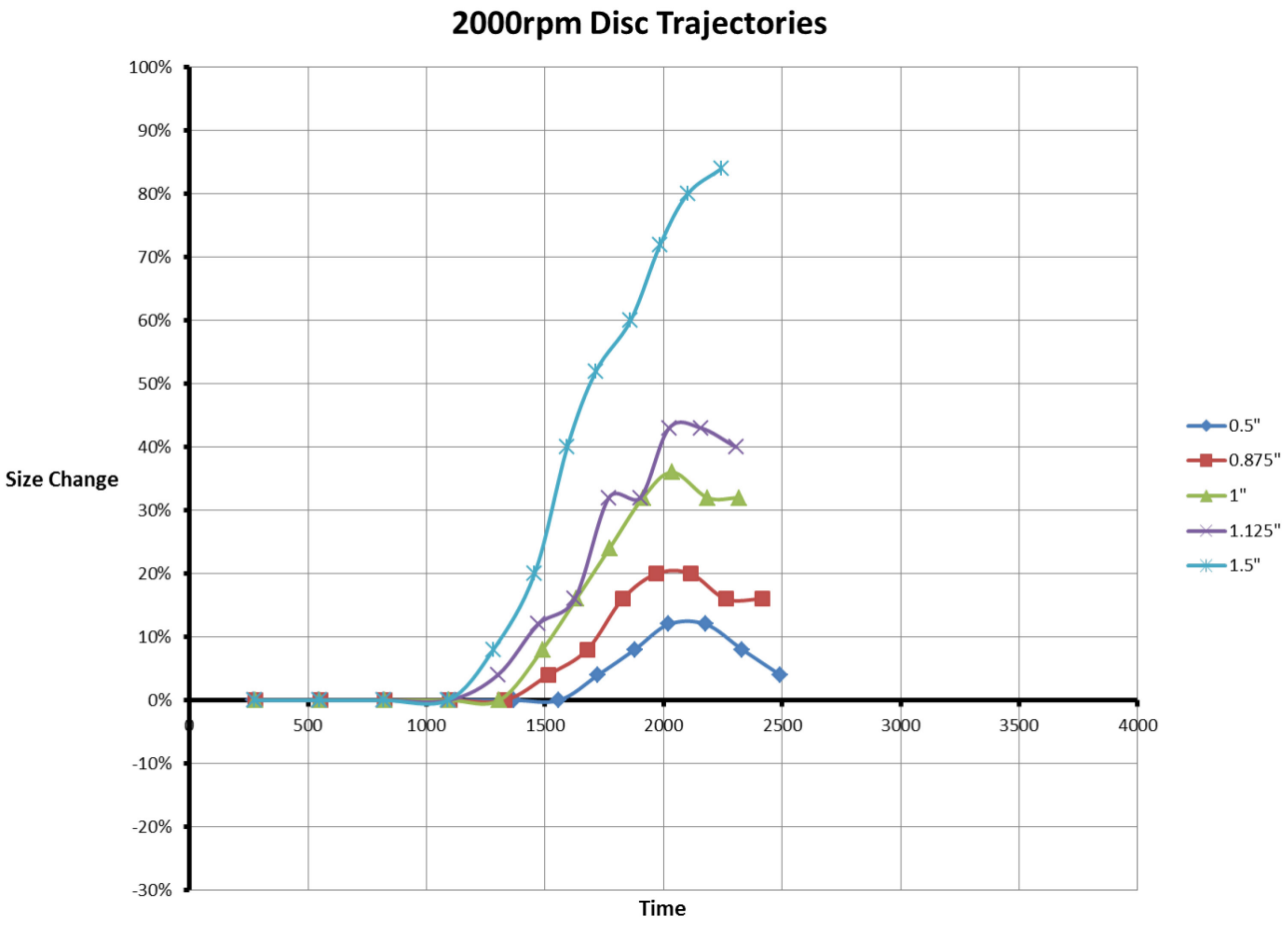

Figure C6. Size change data for 1/8" thick particles in tests conducted with concentric type ECS at 2000rpm

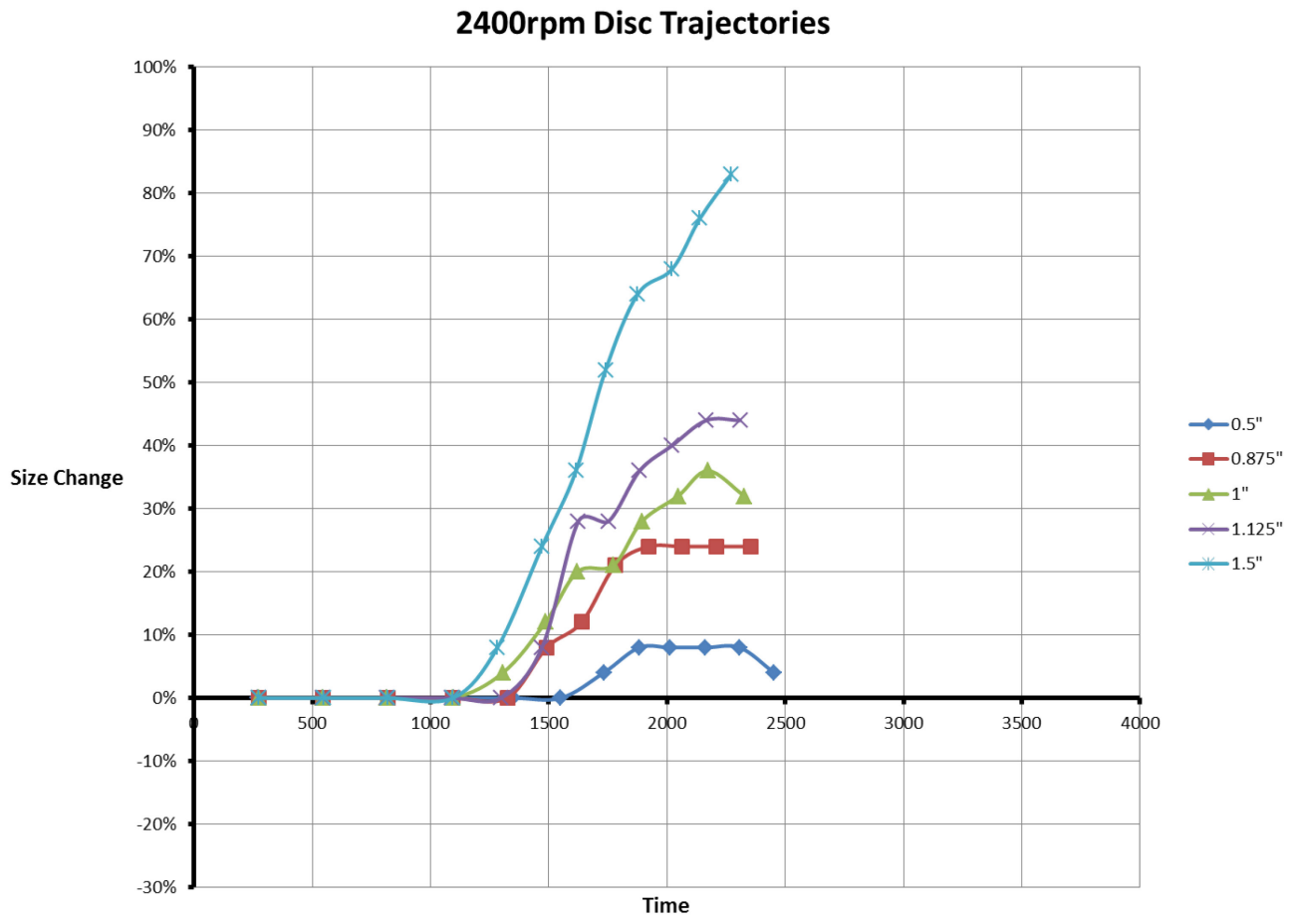

Figure C7. Size change data for 1/8" thick particles in tests conducted with concentric type ECS at 2400rpm

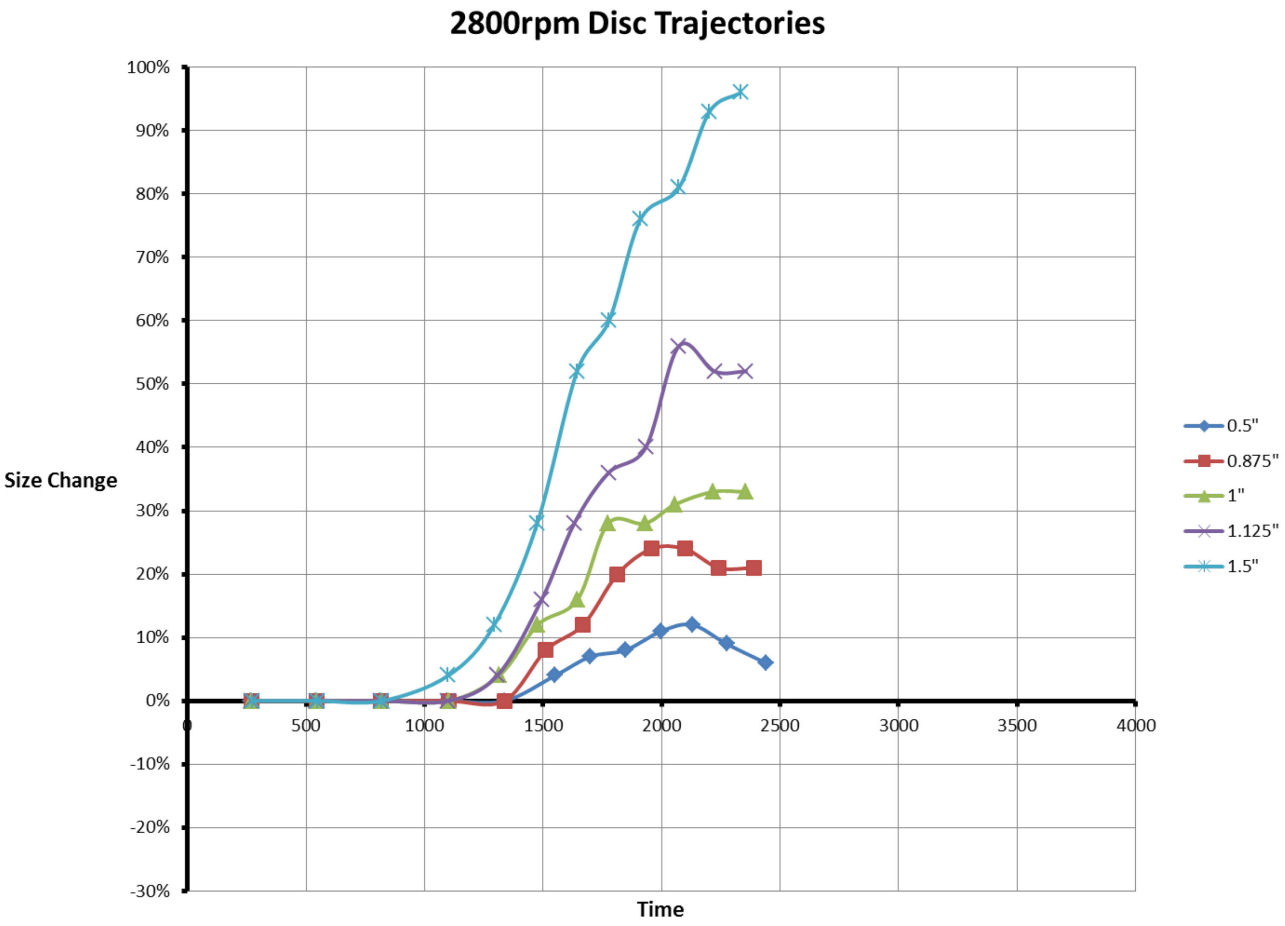

Figure C8. Size change data for 1/8" thick particles in tests conducted with concentric type ECS at 2800rpm

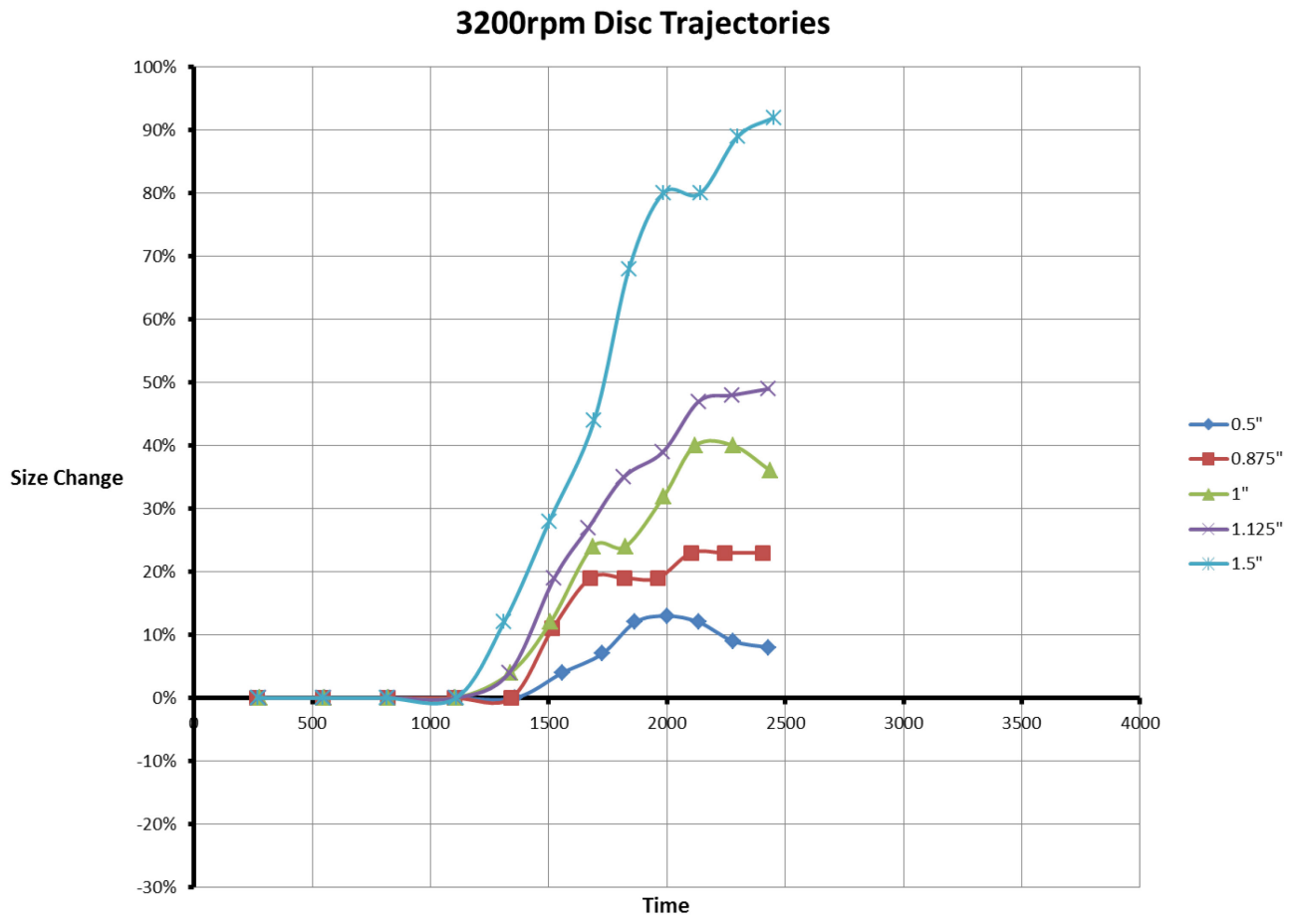

Figure C9. Size change data for 1/8" thick particles in tests conducted with concentric type ECS at 3200rpm

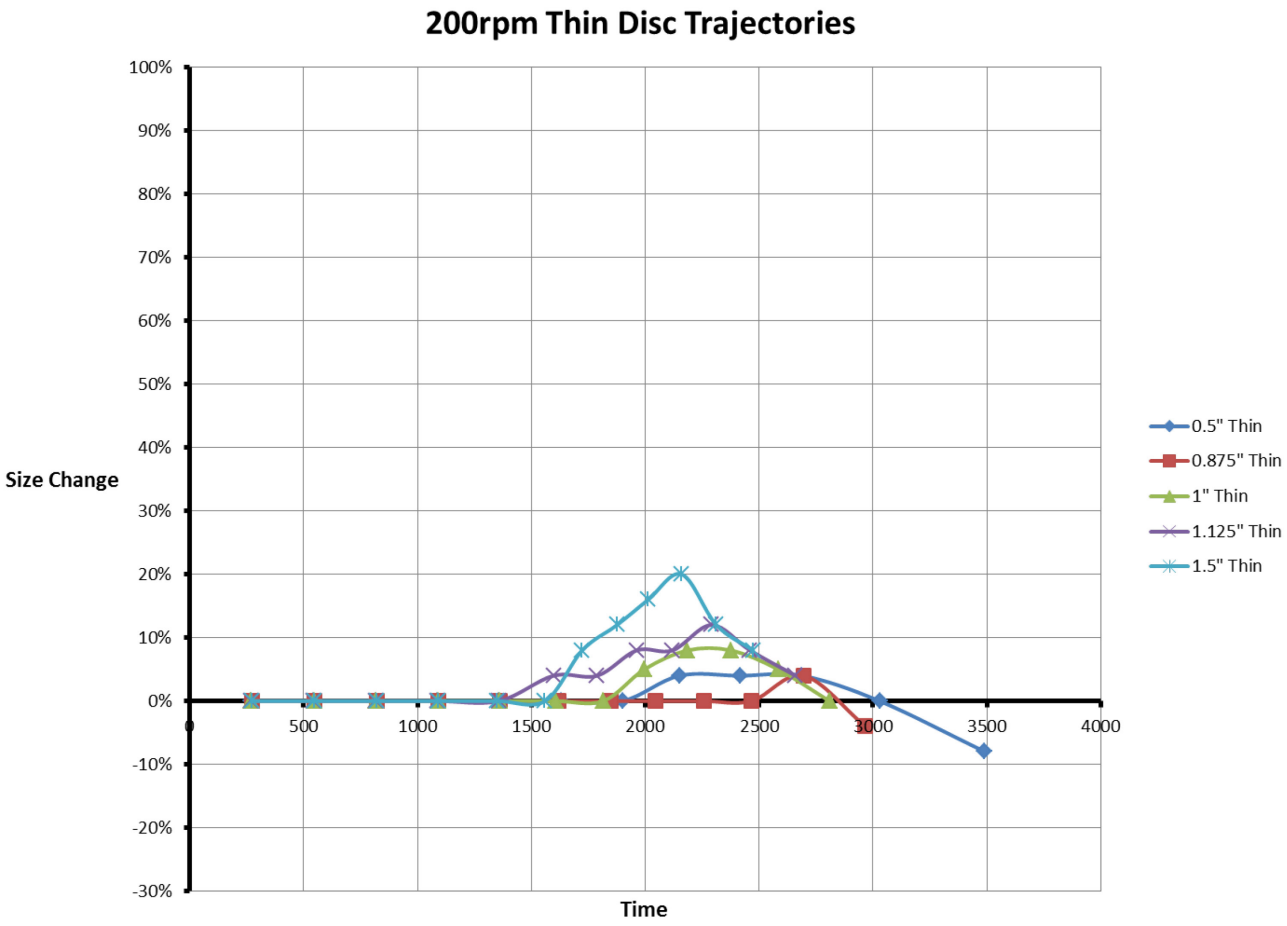

Figure C10. Size change data for 1/16" thick particles in tests conducted with concentric type ECS at 200rpm

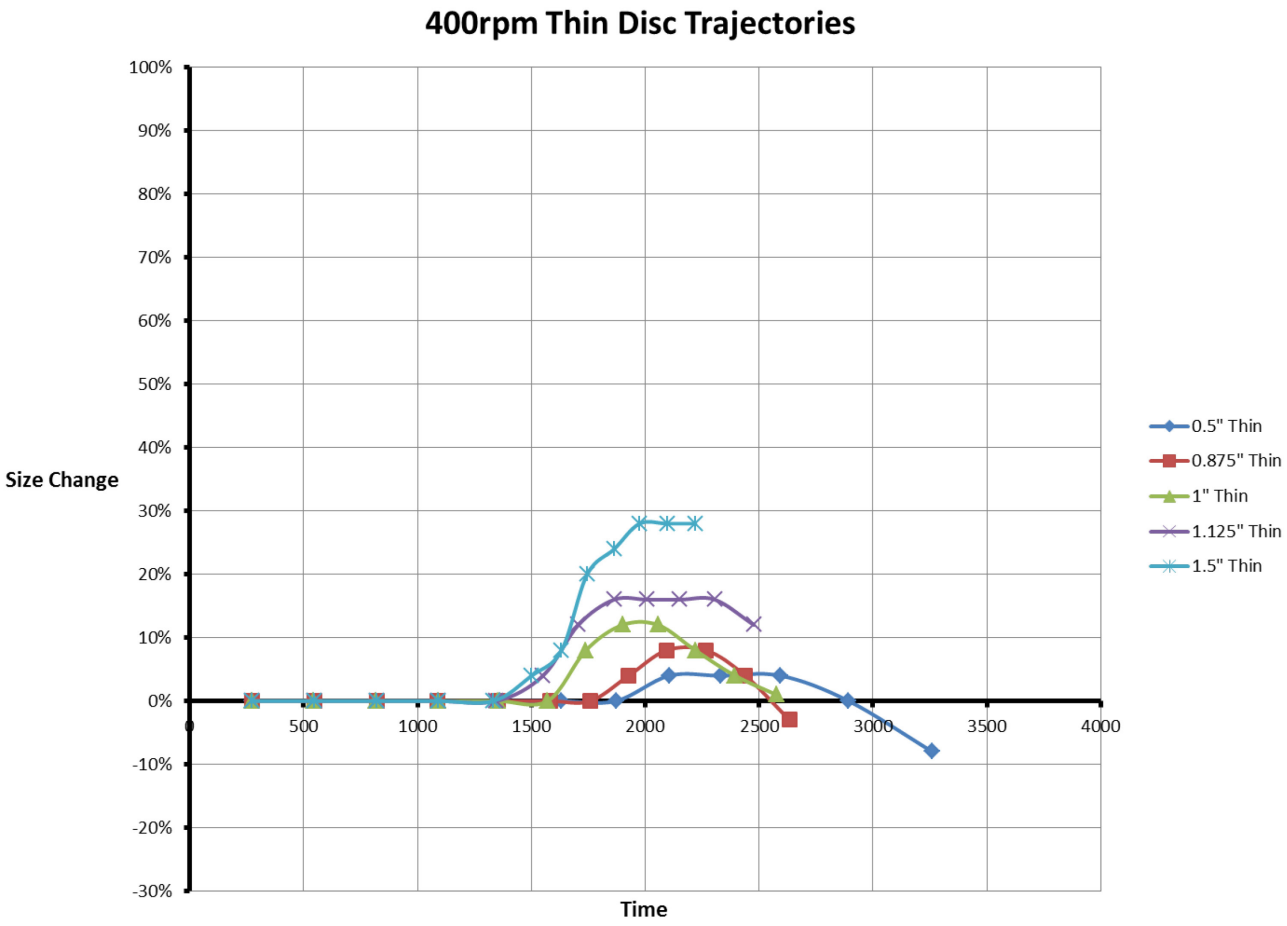

Figure C11. Size change data for 1/16" thick particles in tests conducted with concentric type ECS at 400rpm

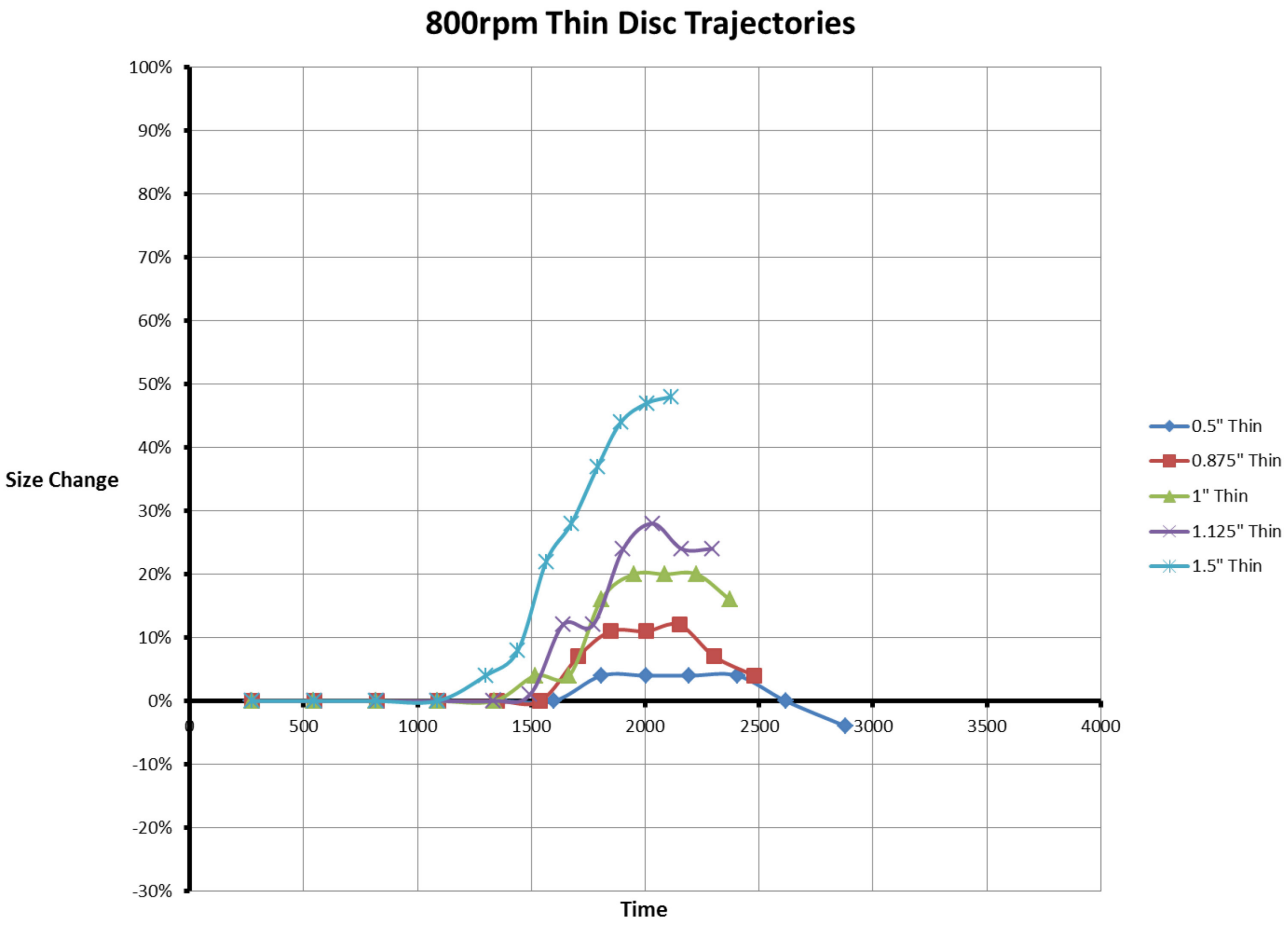

Figure C12. Size change data for 1/16" thick particles in tests conducted with concentric type ECS at 800rpm

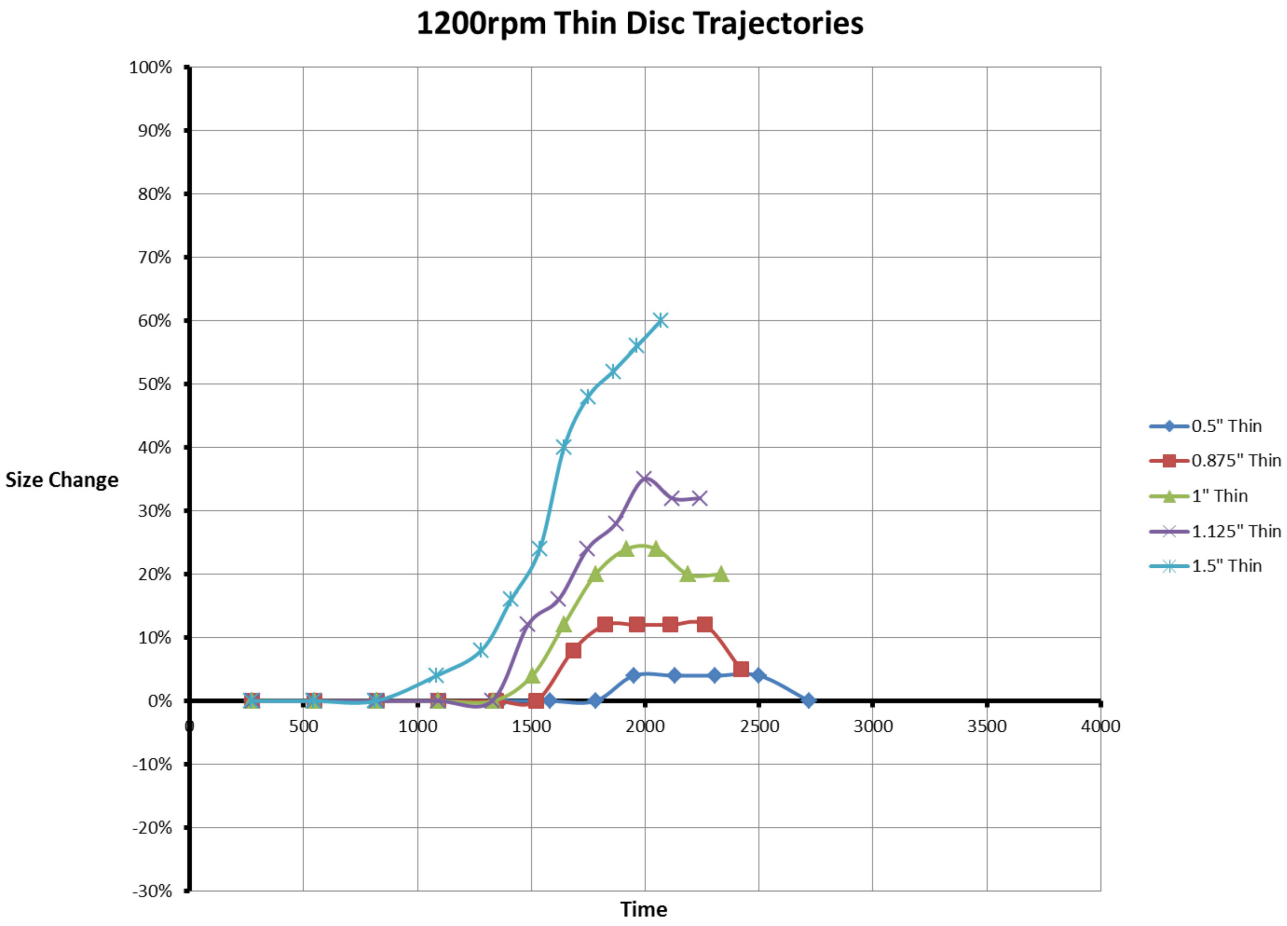

Figure C13. Size change data for 1/16" thick particles in tests conducted with concentric type ECS at 1200rpm

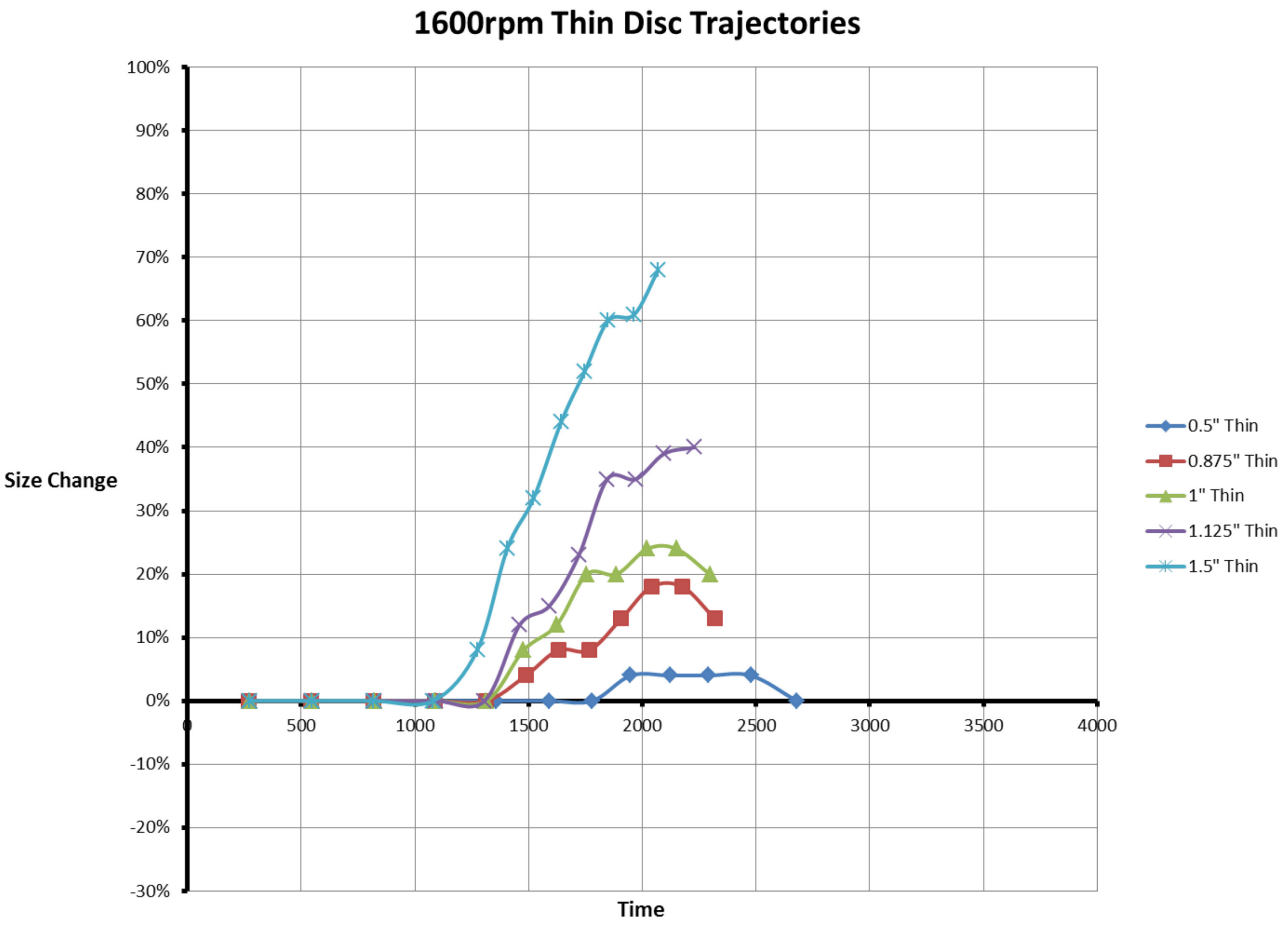

Figure C14. Size change data for 1/16" thick particles in tests conducted with concentric type ECS at 1600rpm

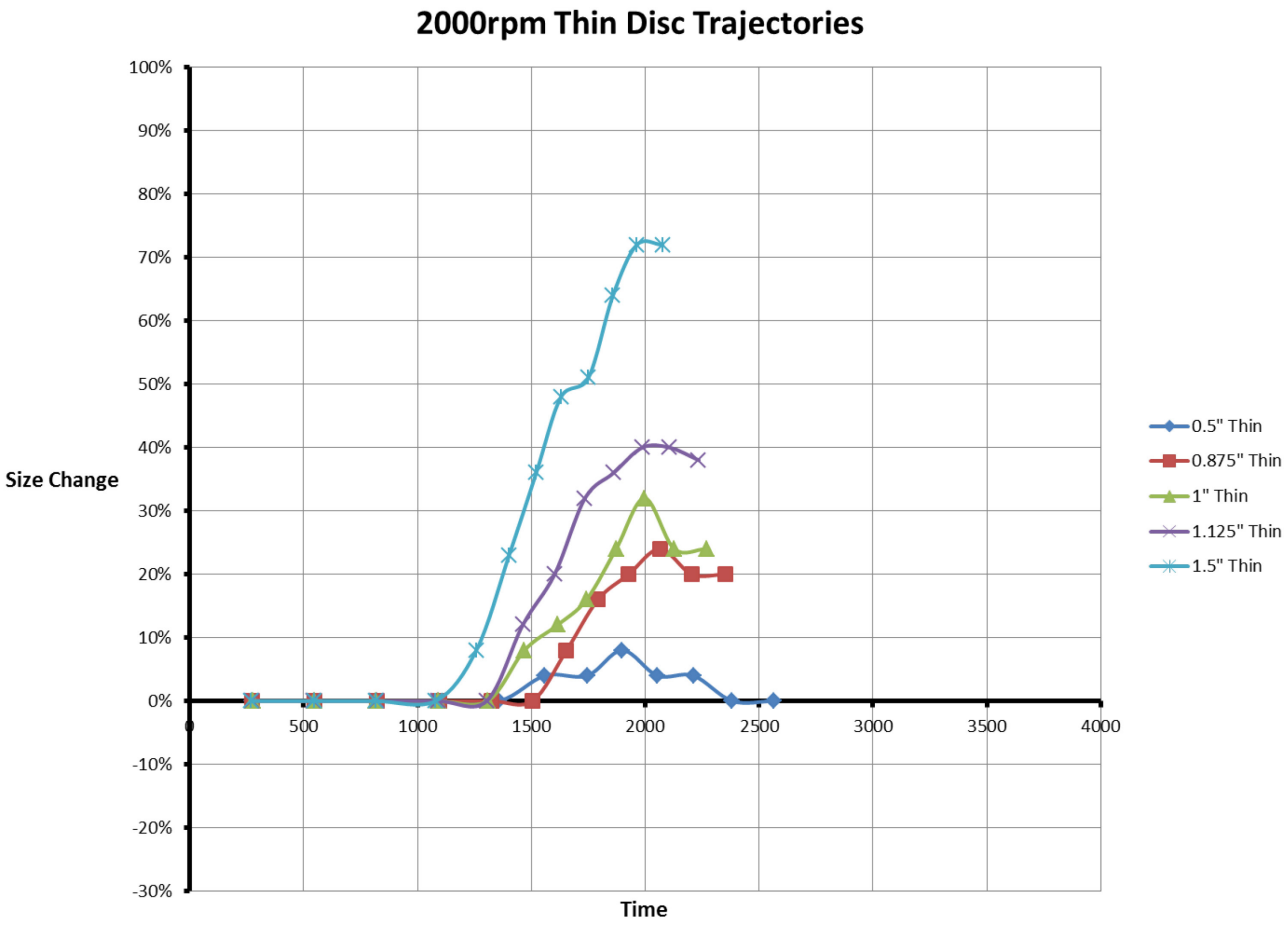

Figure C15. Size change data for 1/16" thick particles in tests conducted with concentric type ECS at 2000rpm

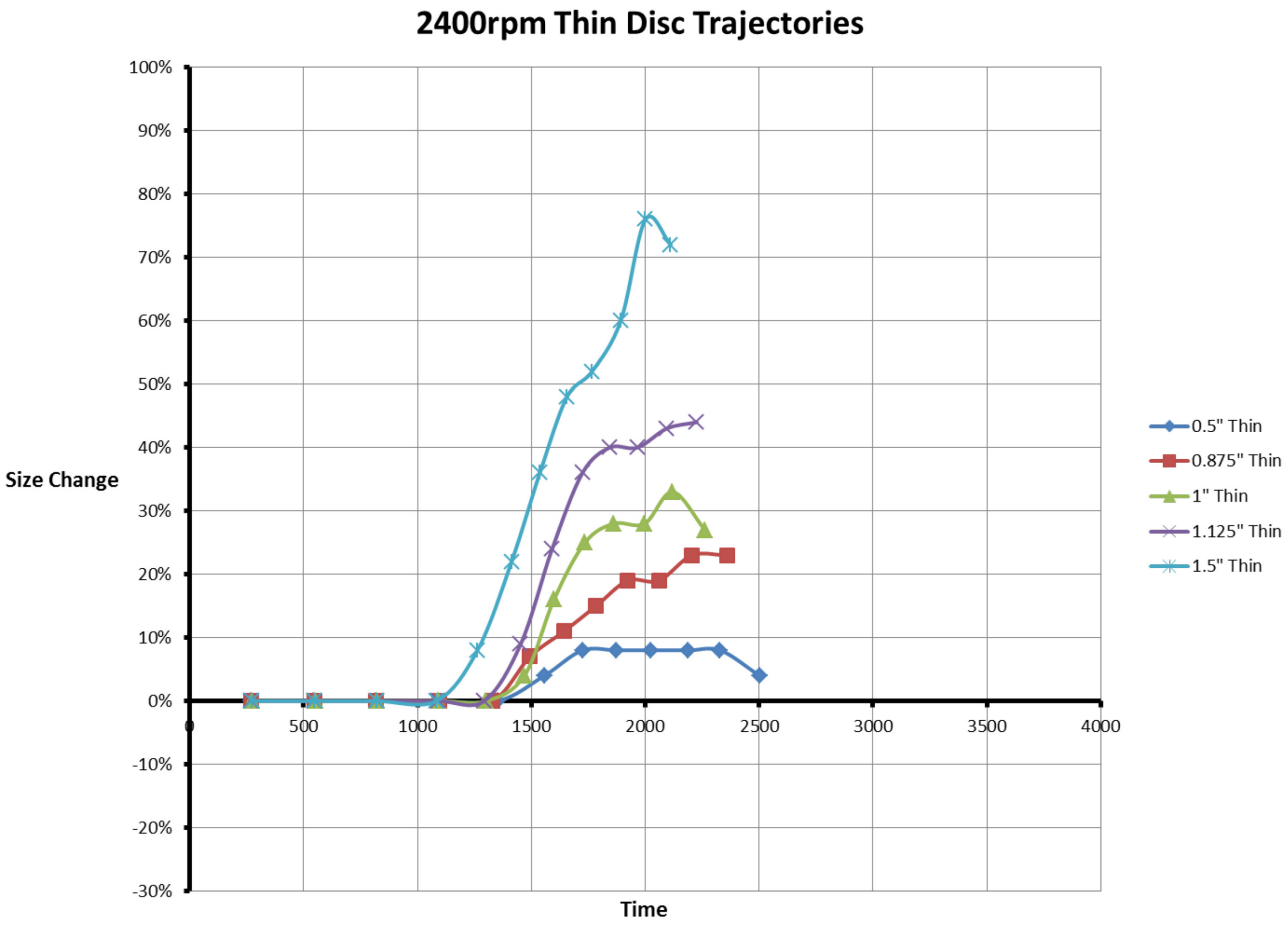

Figure C16. Size change data for 1/16" thick particles in tests conducted with concentric type ECS at 2400rpm

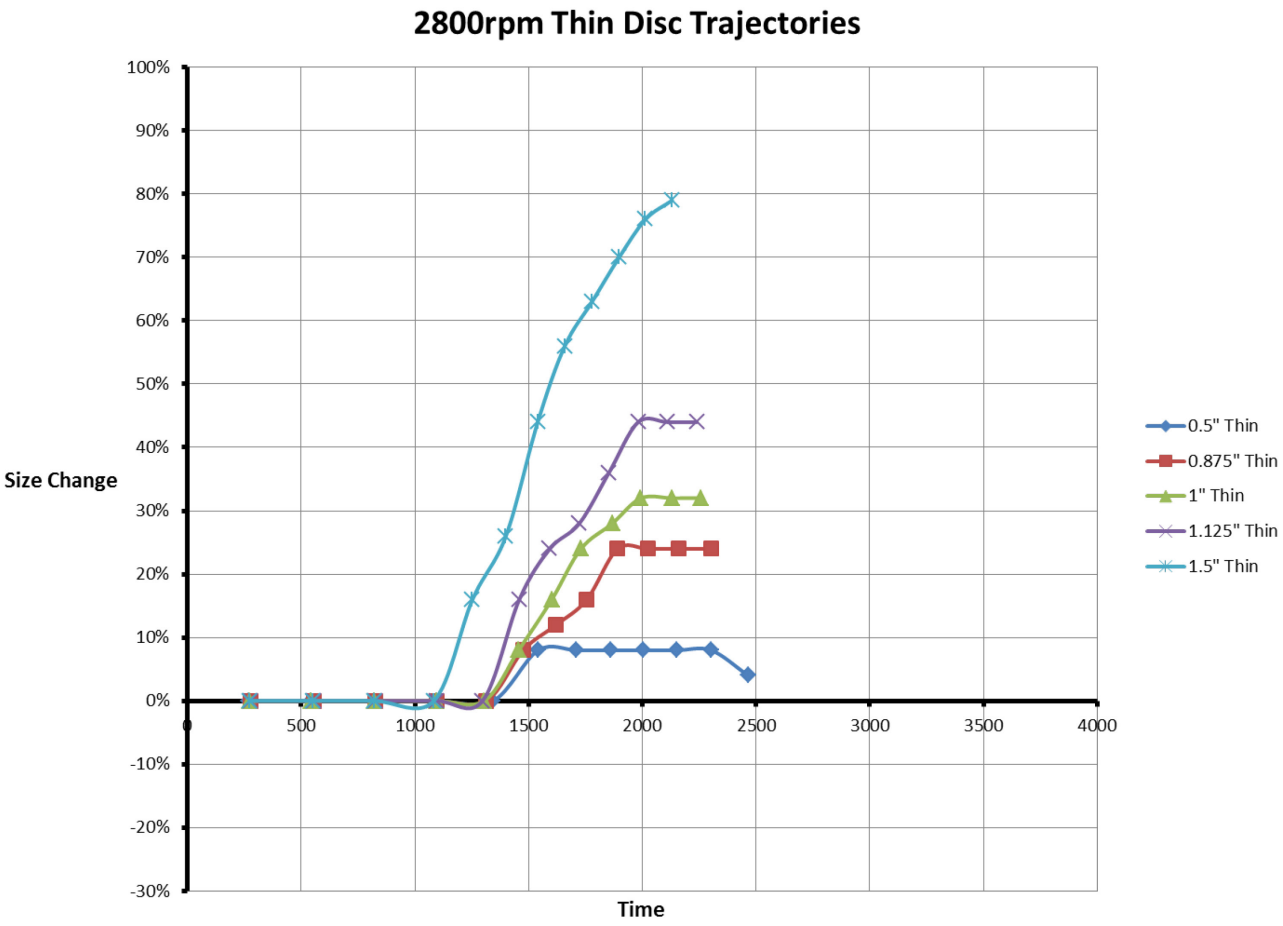

Figure C17. Size change data for 1/16" thick particles in tests conducted with concentric type ECS at 2800rpm

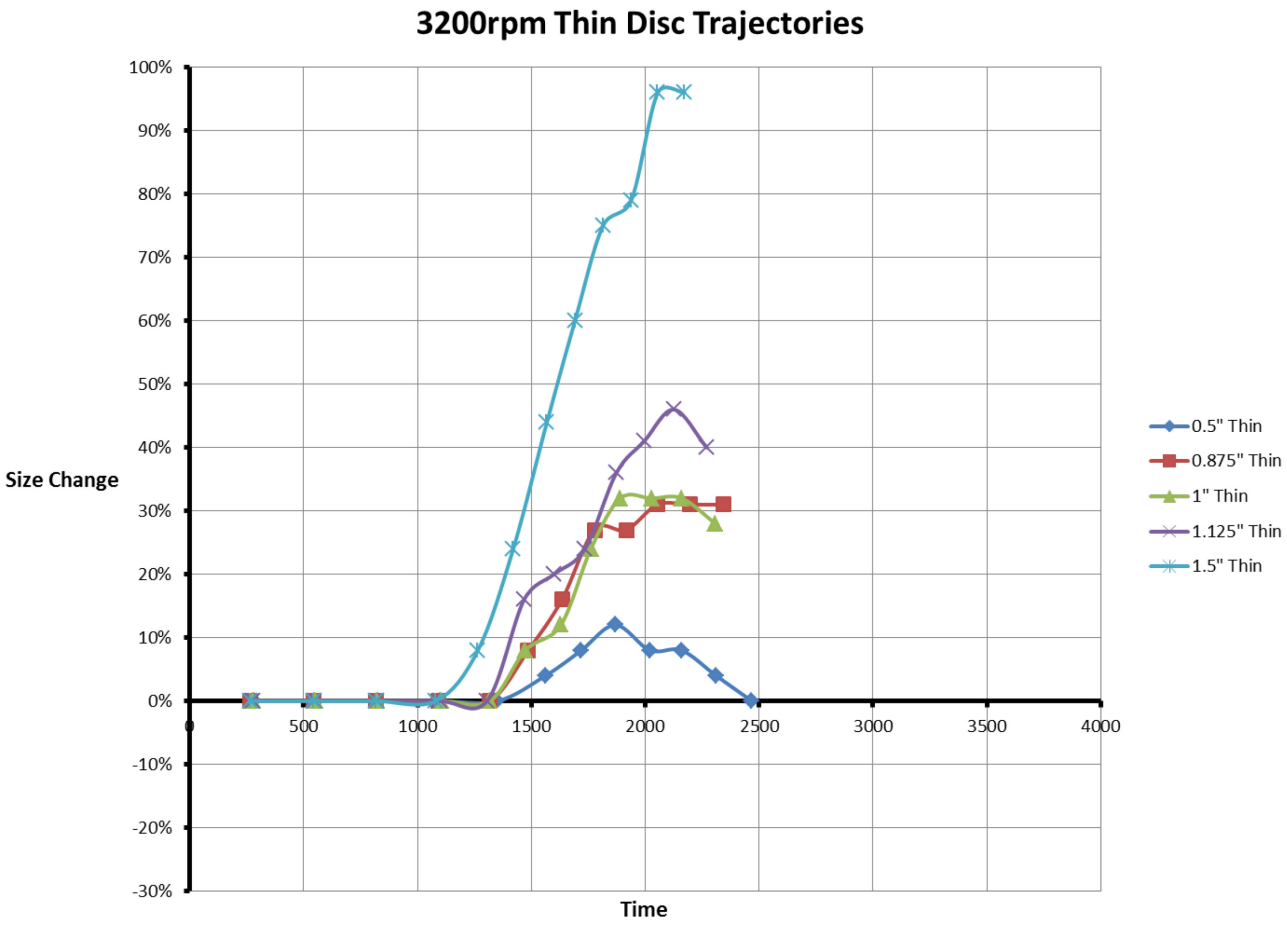

Figure C18. Size change data for 1/16" thick particles in tests conducted with concentric type ECS at 3200rpm

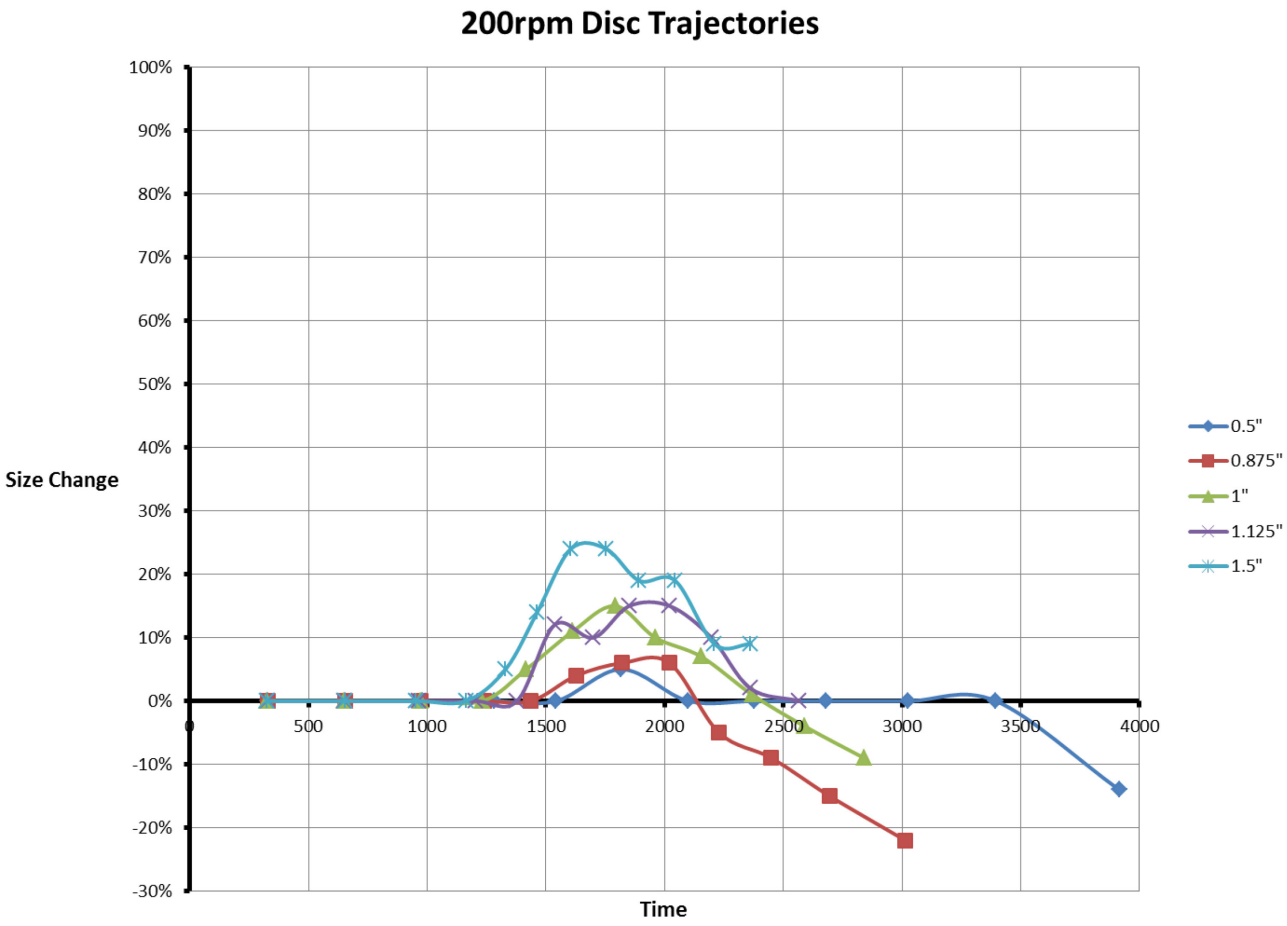

Figure C19. Size change data for 1/8" thick particles in tests conducted with eccentric type ECS at 200rpm

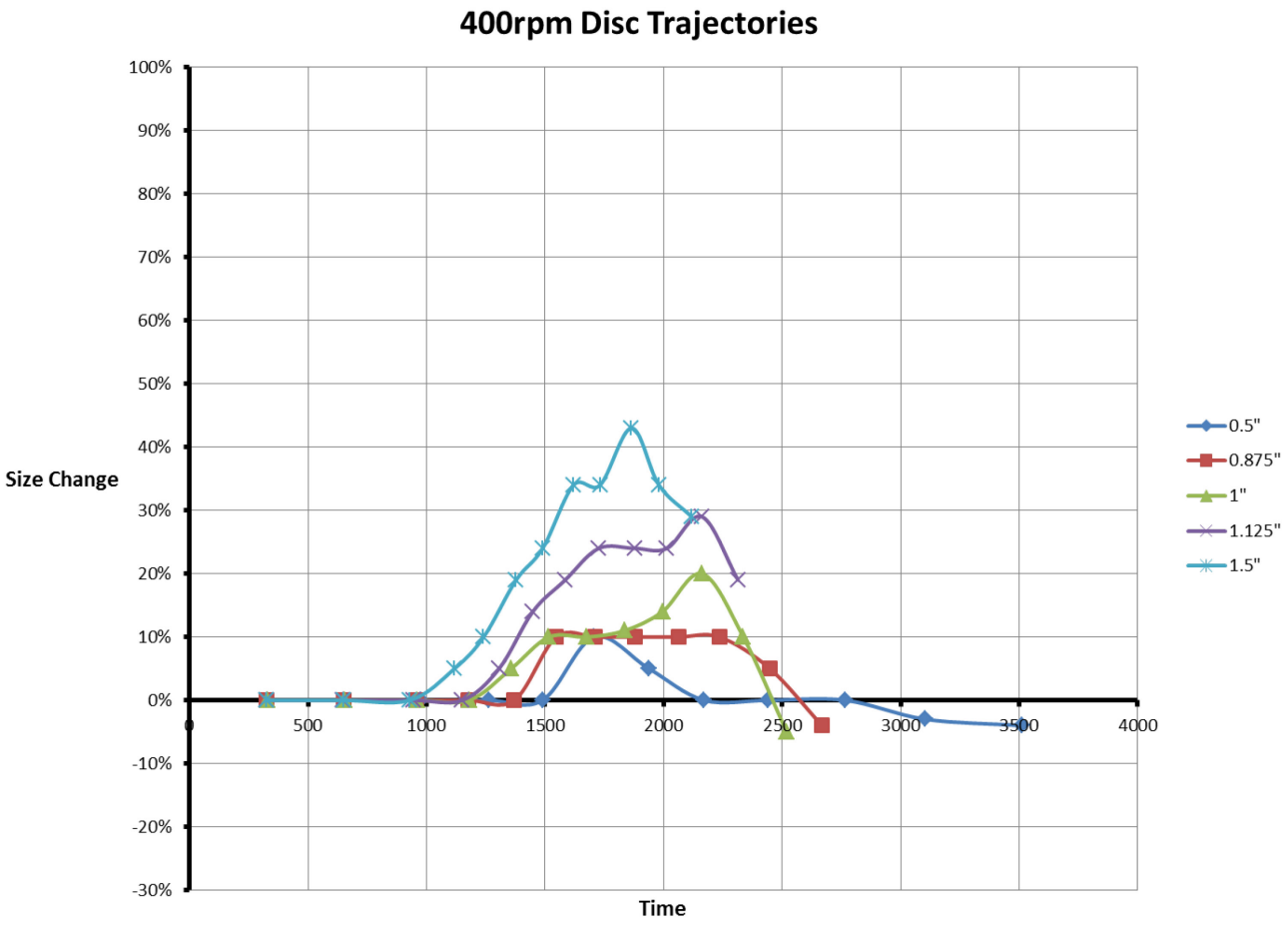

Figure C20. Size change data for 1/8" thick particles in tests conducted with eccentric type ECS at 400rpm

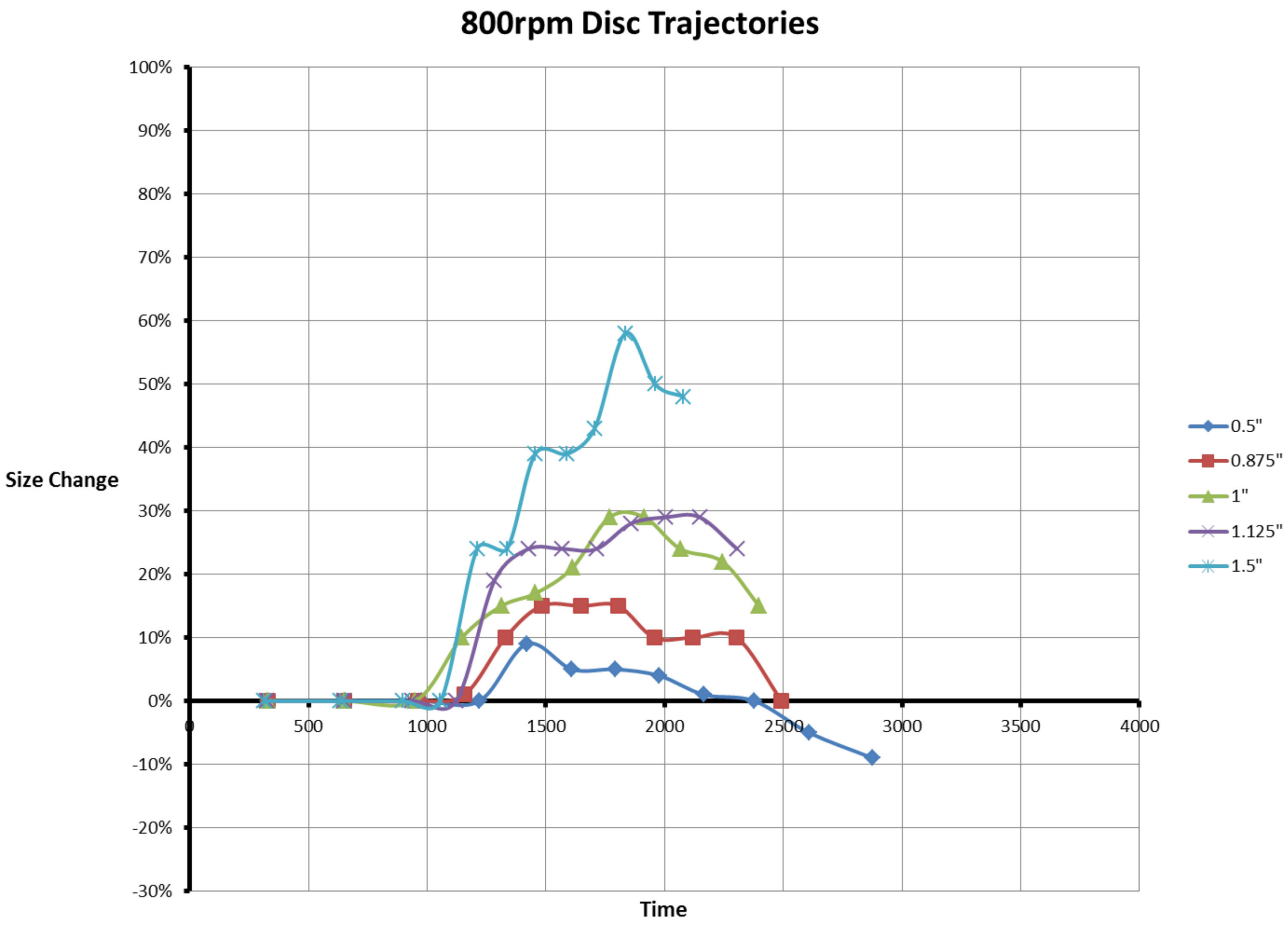

Figure C21. Size change data for 1/8" thick particles in tests conducted with eccentric type ECS at 800rpm

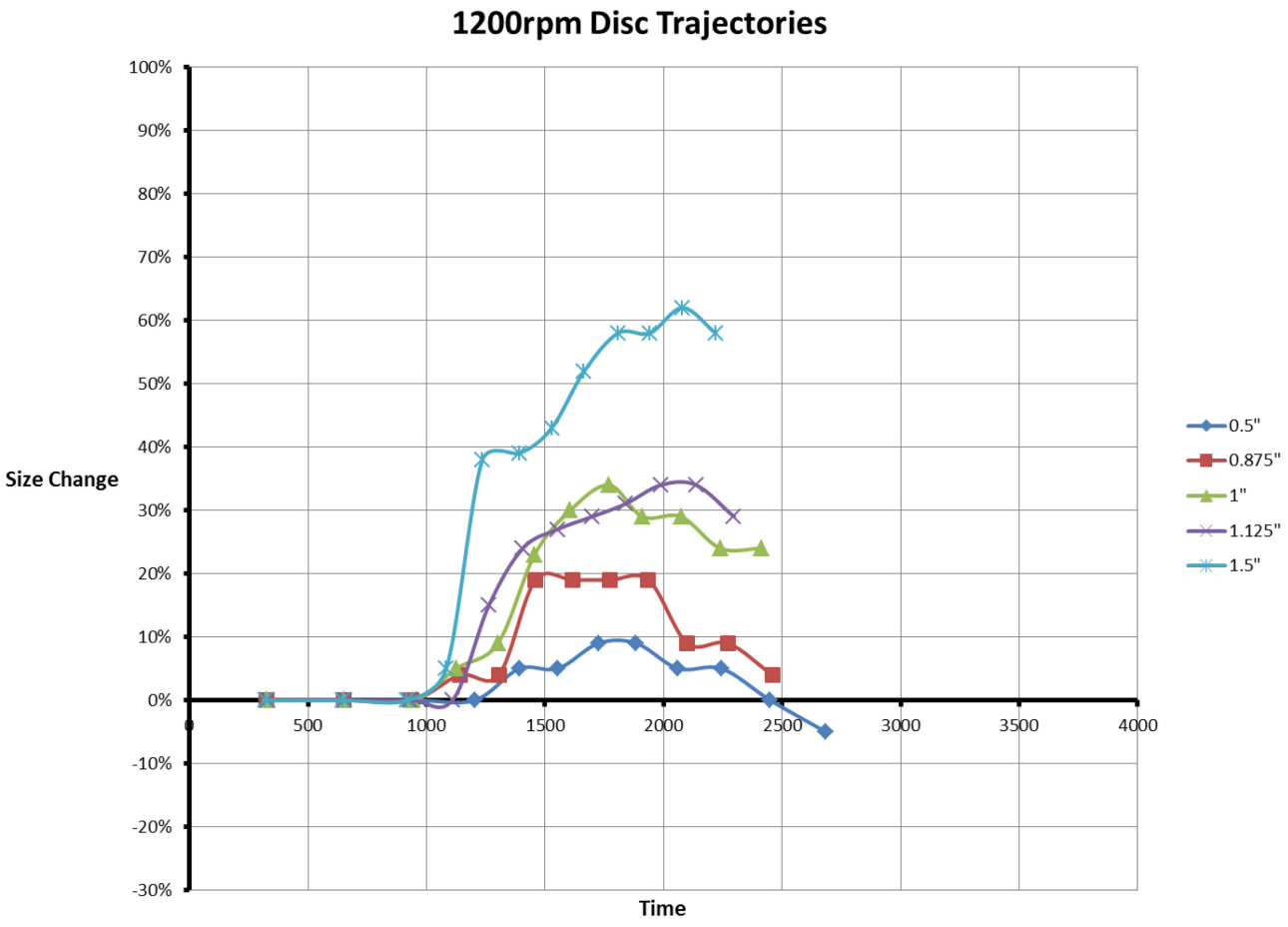

Figure C22. Size change data for 1/8" thick particles in tests conducted with eccentric type ECS at 1200rpm

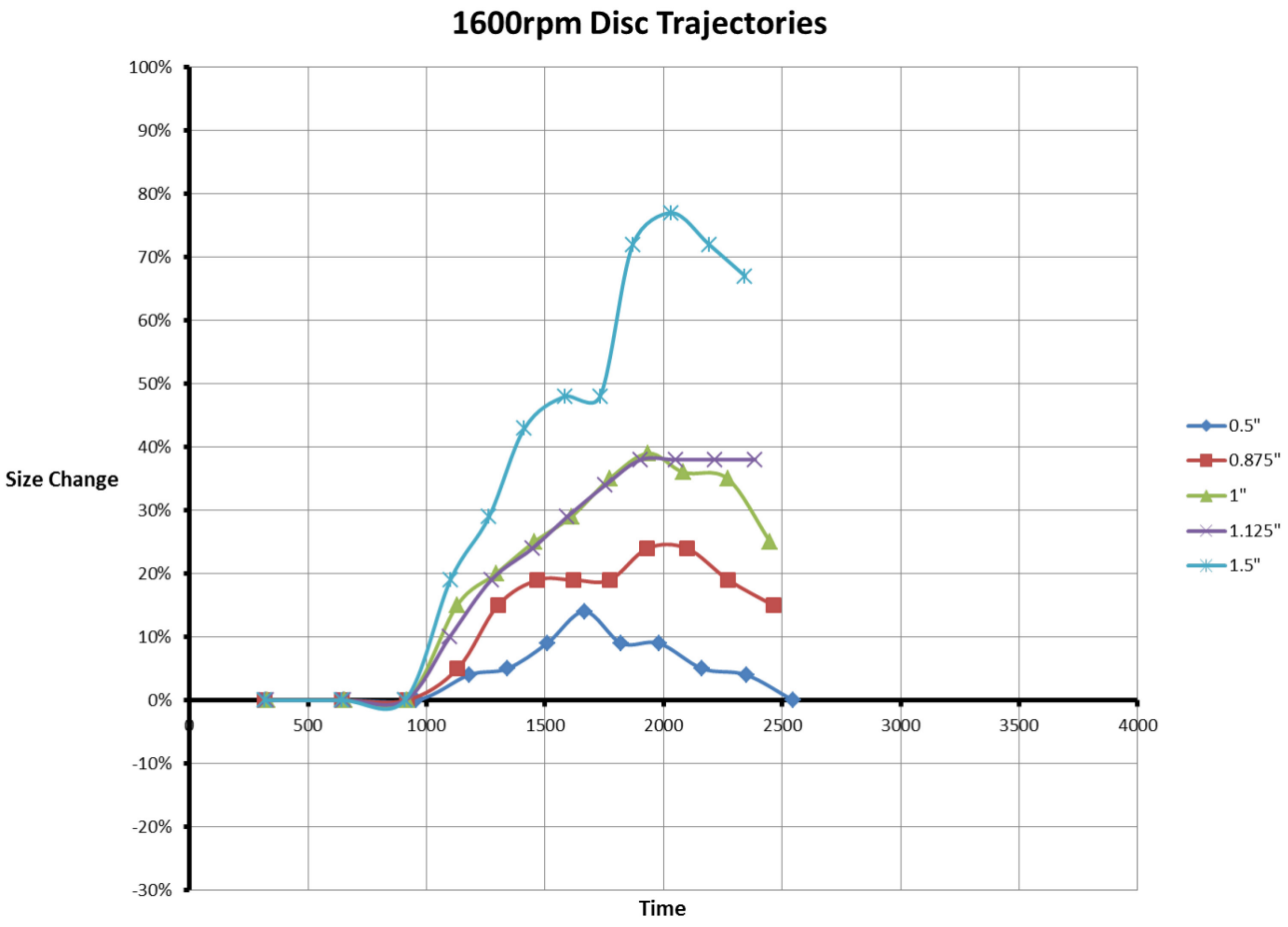

Figure C23. Size change data for 1/8" thick particles in tests conducted with eccentric type ECS at 1600rpm

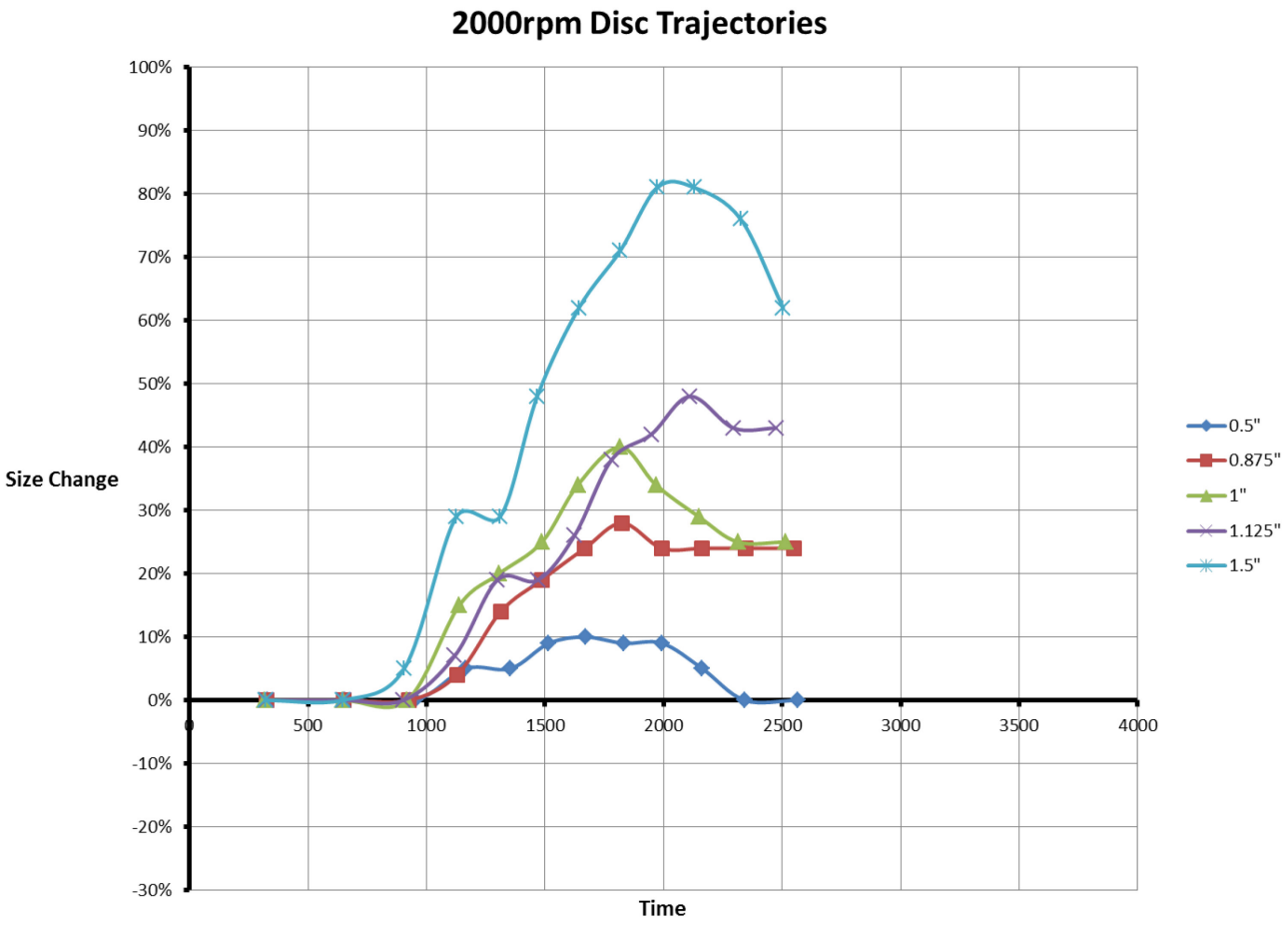

Figure C24. Size change data for 1/8" thick particles in tests conducted with eccentric type ECS at 2000rpm

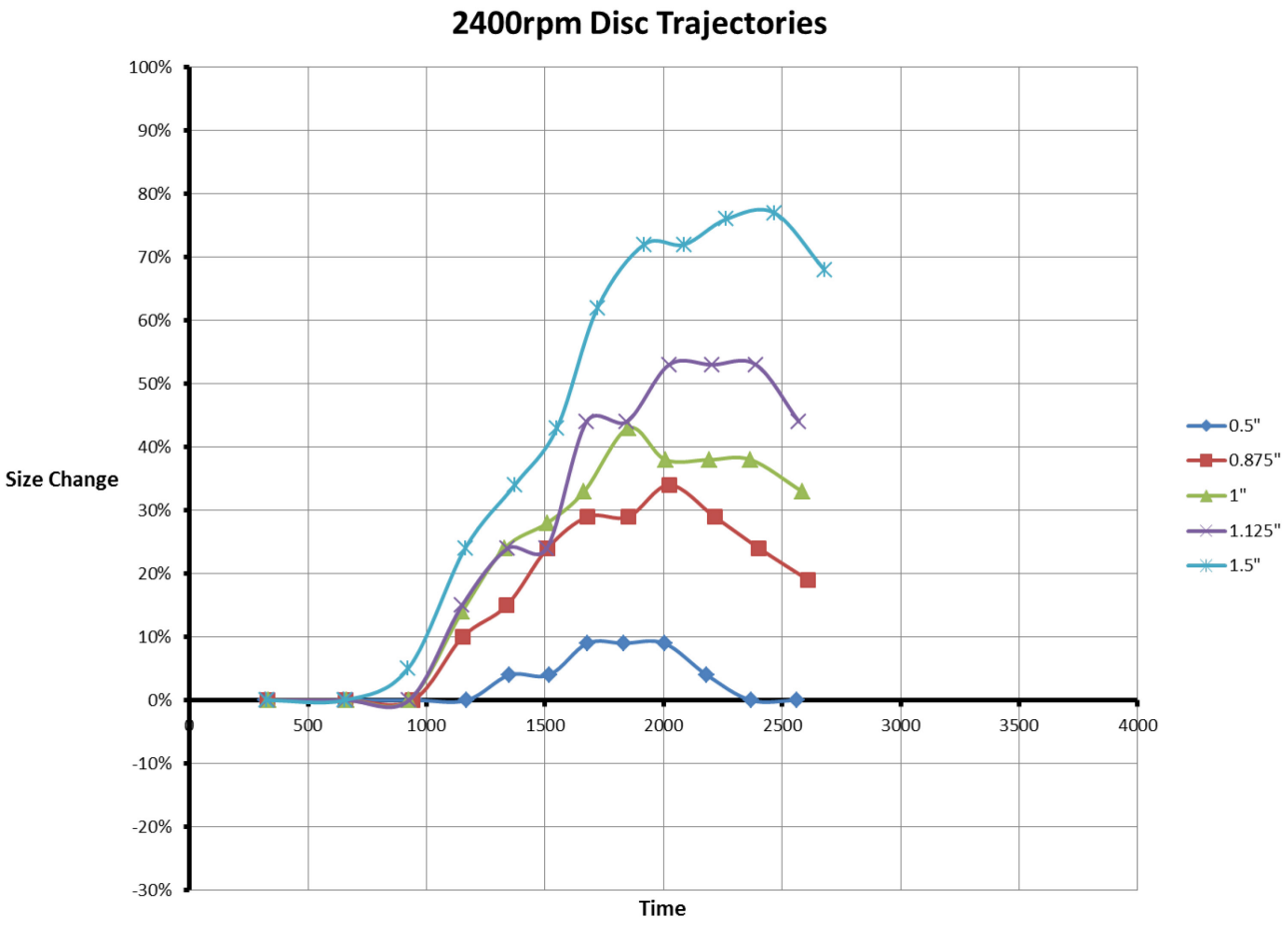

Figure C25. Size change data for 1/8" thick particles in tests conducted with eccentric type ECS at 2400rpm

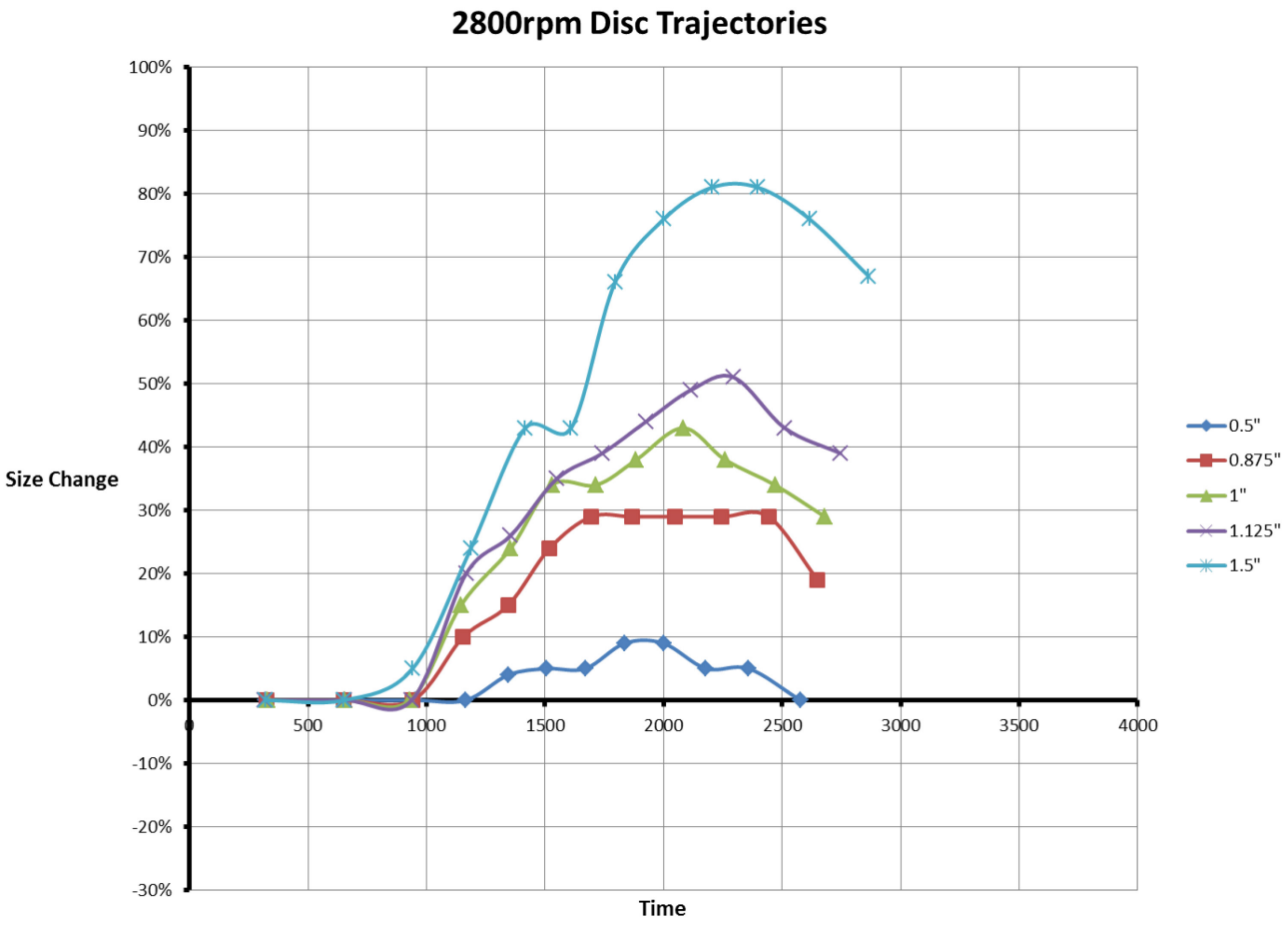

Figure C26. Size change data for 1/8" thick particles in tests conducted with eccentric type ECS at 2800rpm

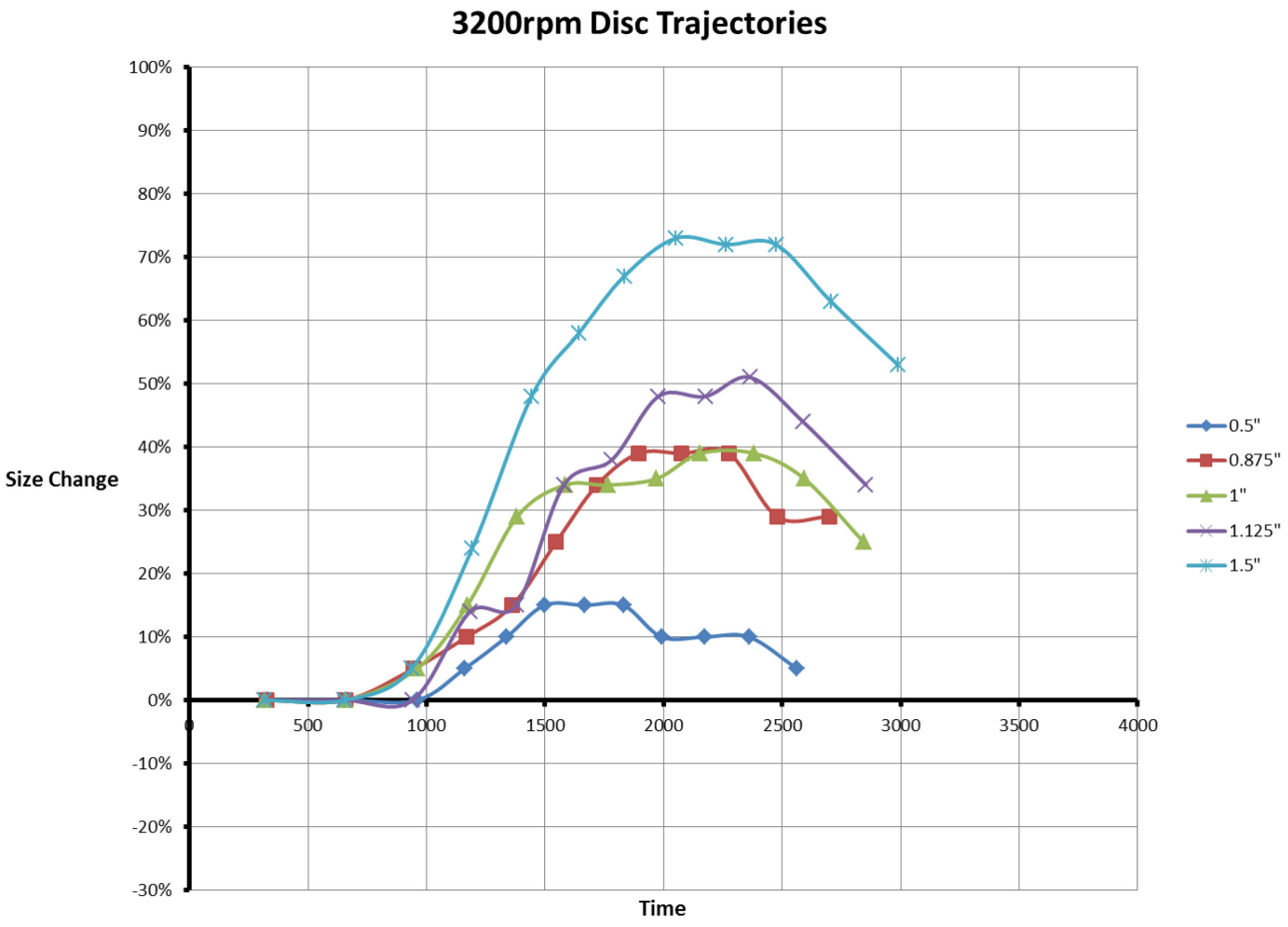

Figure C27. Size change data for 1/8" thick particles in tests conducted with eccentric type ECS at 3200rpm

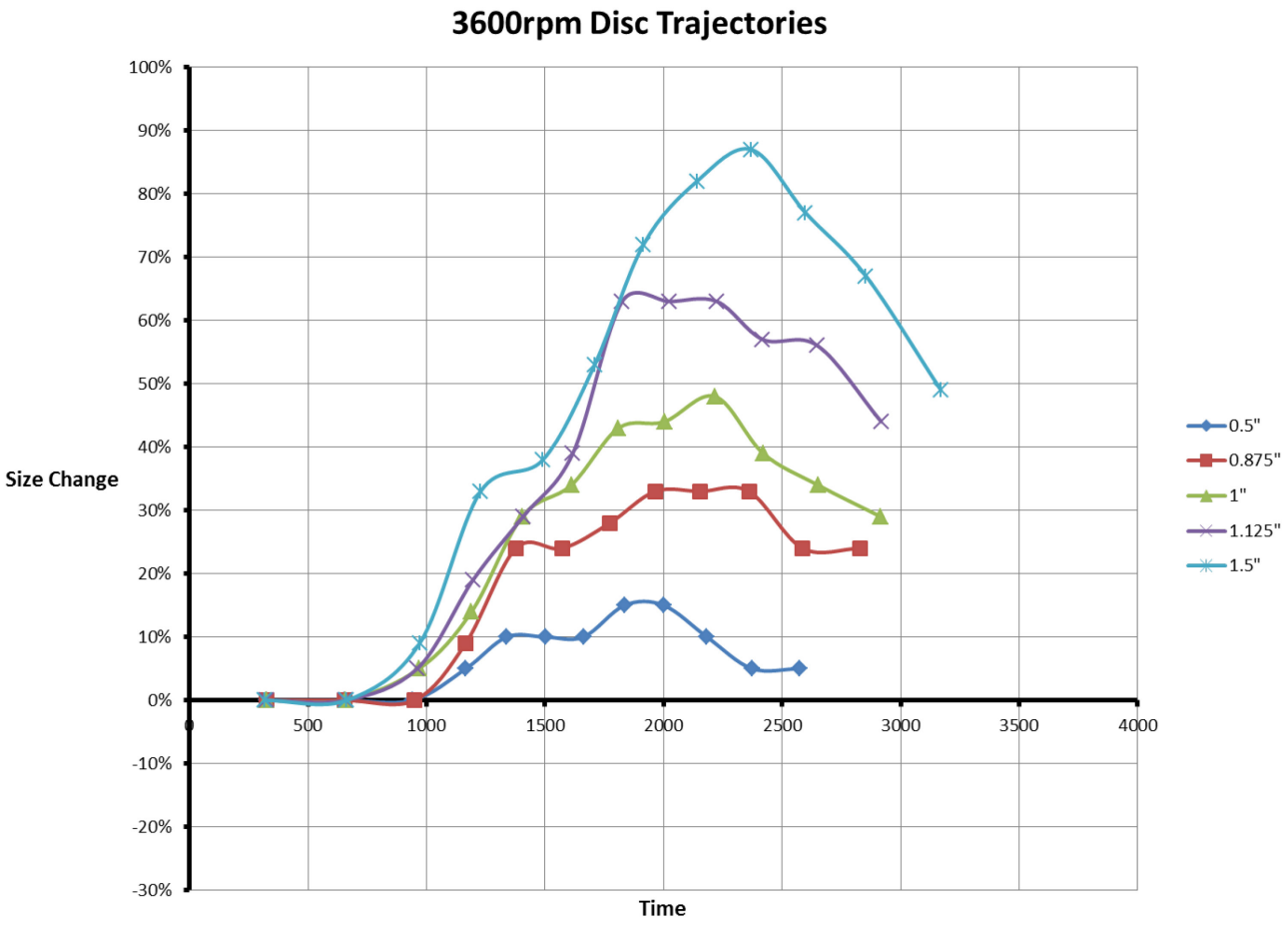

Figure C28. Size change data for 1/8" thick particles in tests conducted with eccentric type ECS at 3600rpm

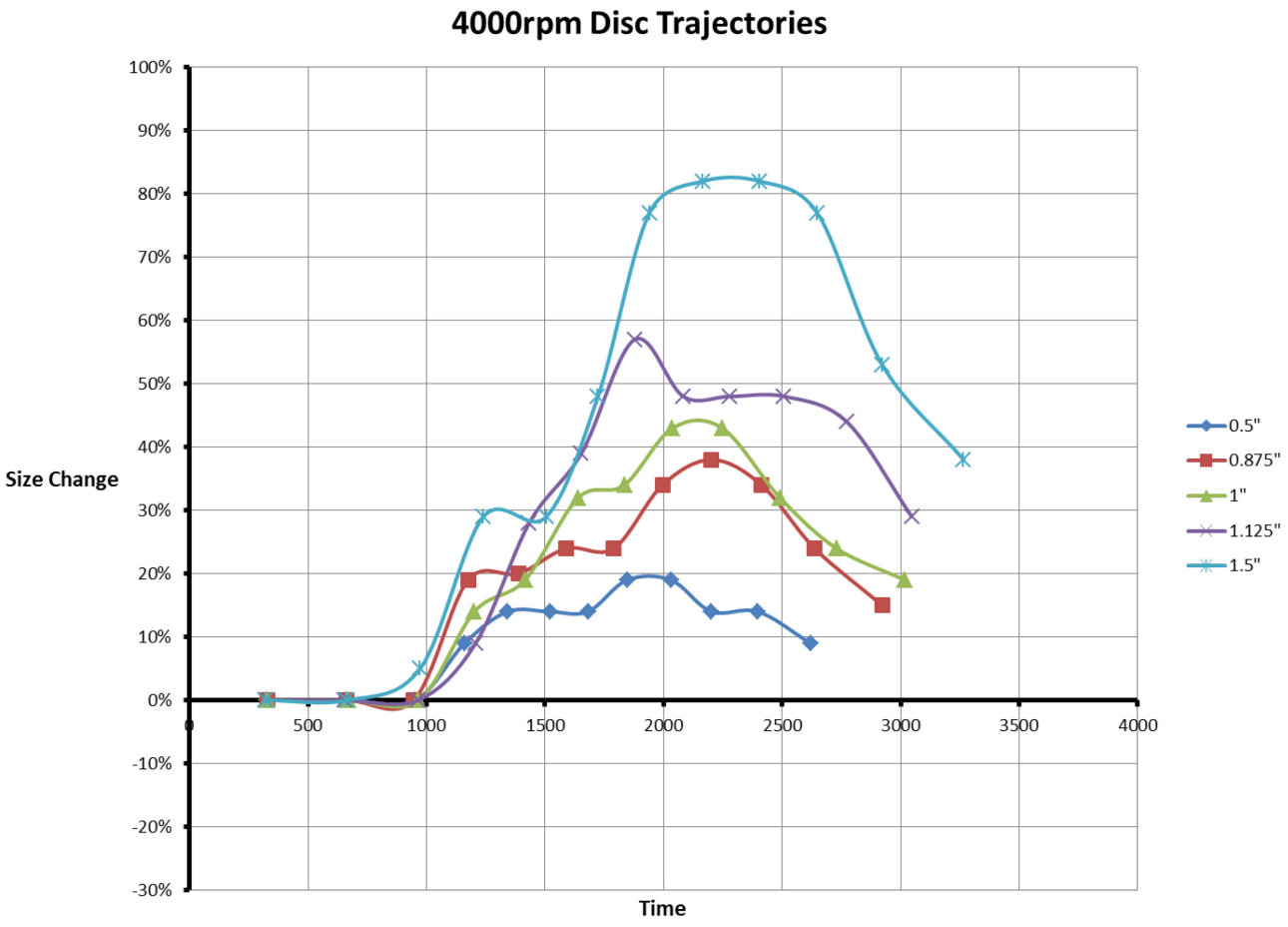

Figure C29. Size change data for 1/8" thick particles in tests conducted with eccentric type ECS at 4000rpm

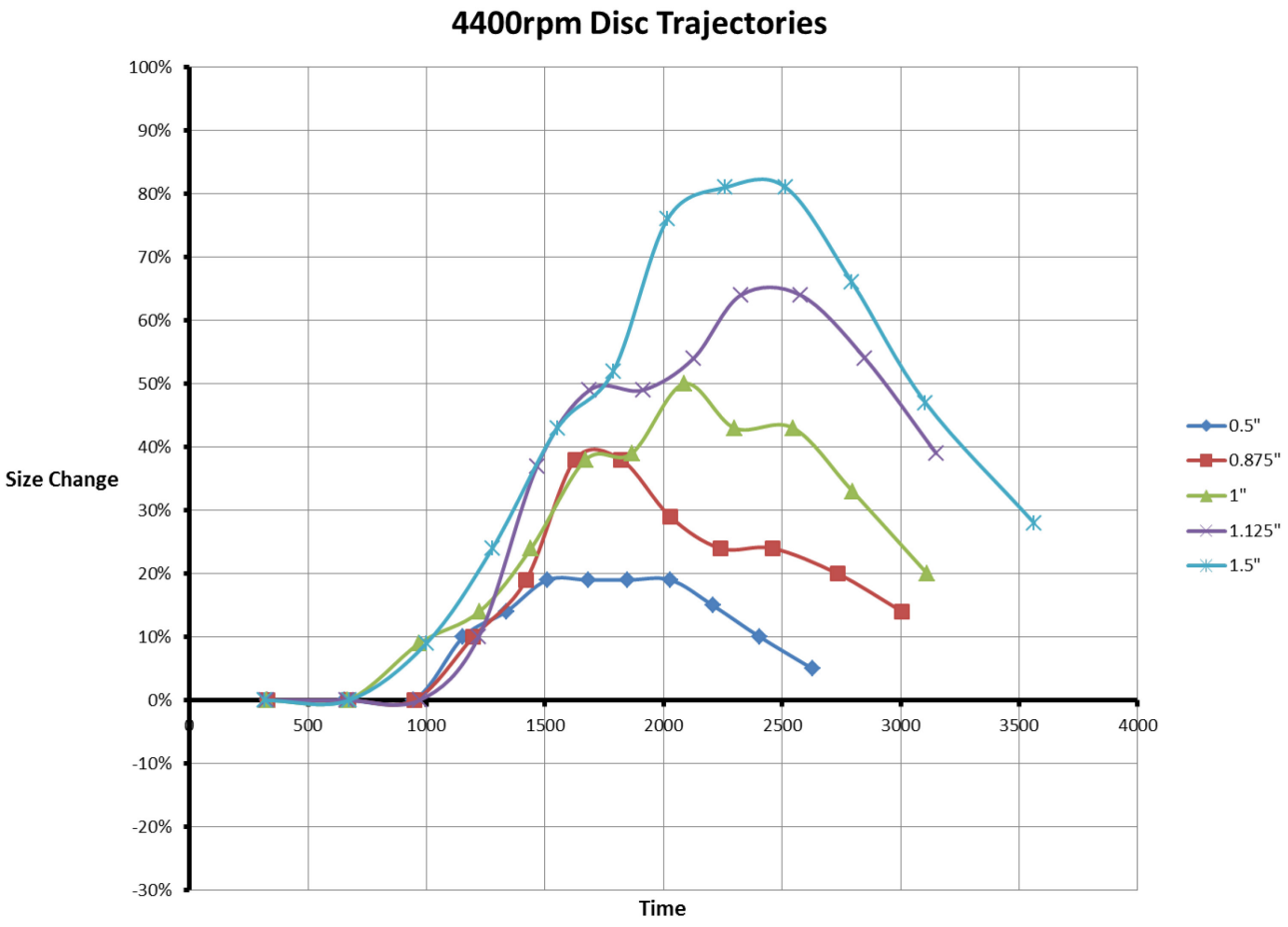

Figure C30. Size change data for 1/8" thick particles in tests conducted with eccentric type ECS at 4400rpm

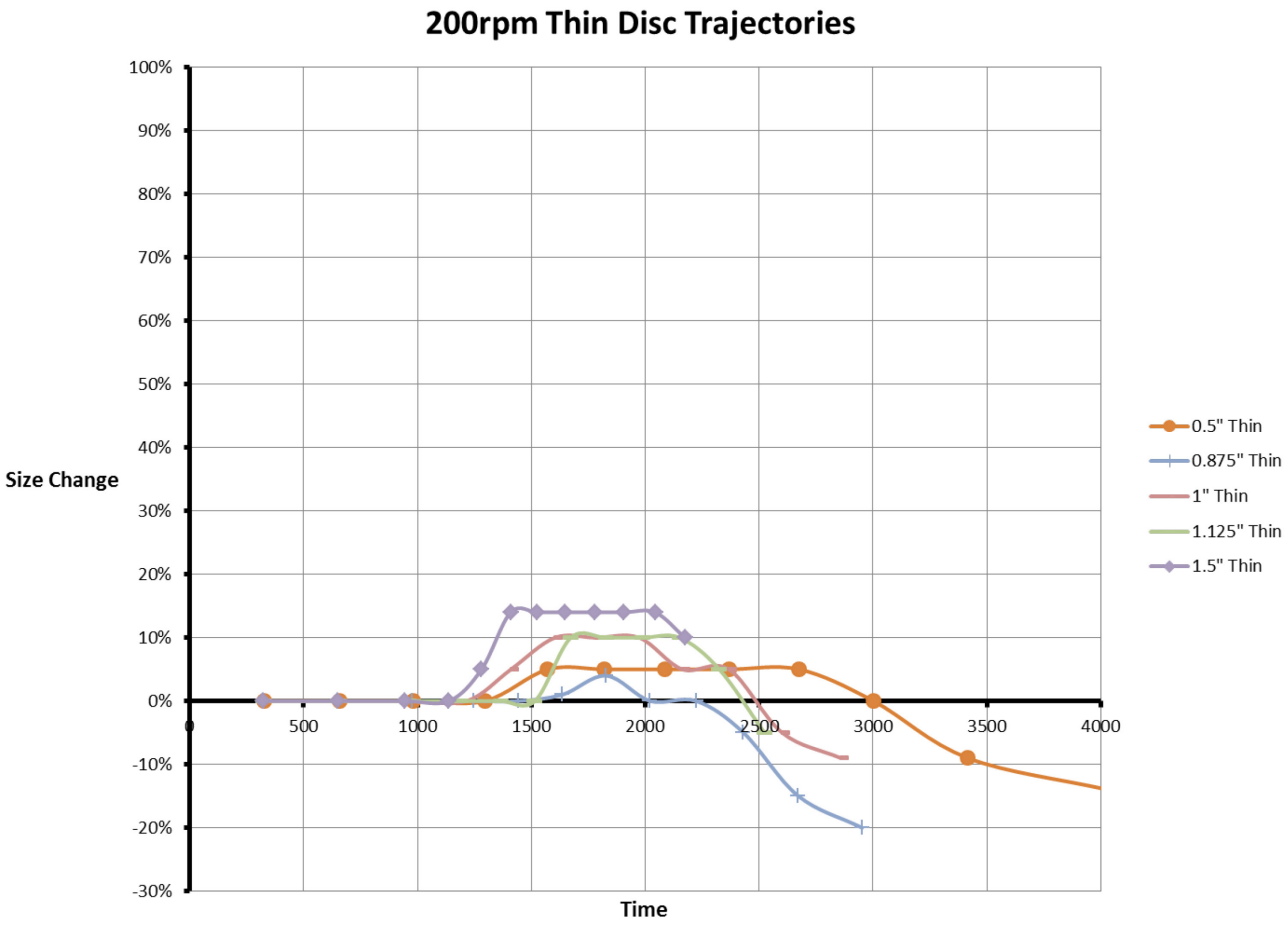

Figure C31. Size change data for 1/16" thick particles in tests conducted with eccentric type ECS at 200rpm

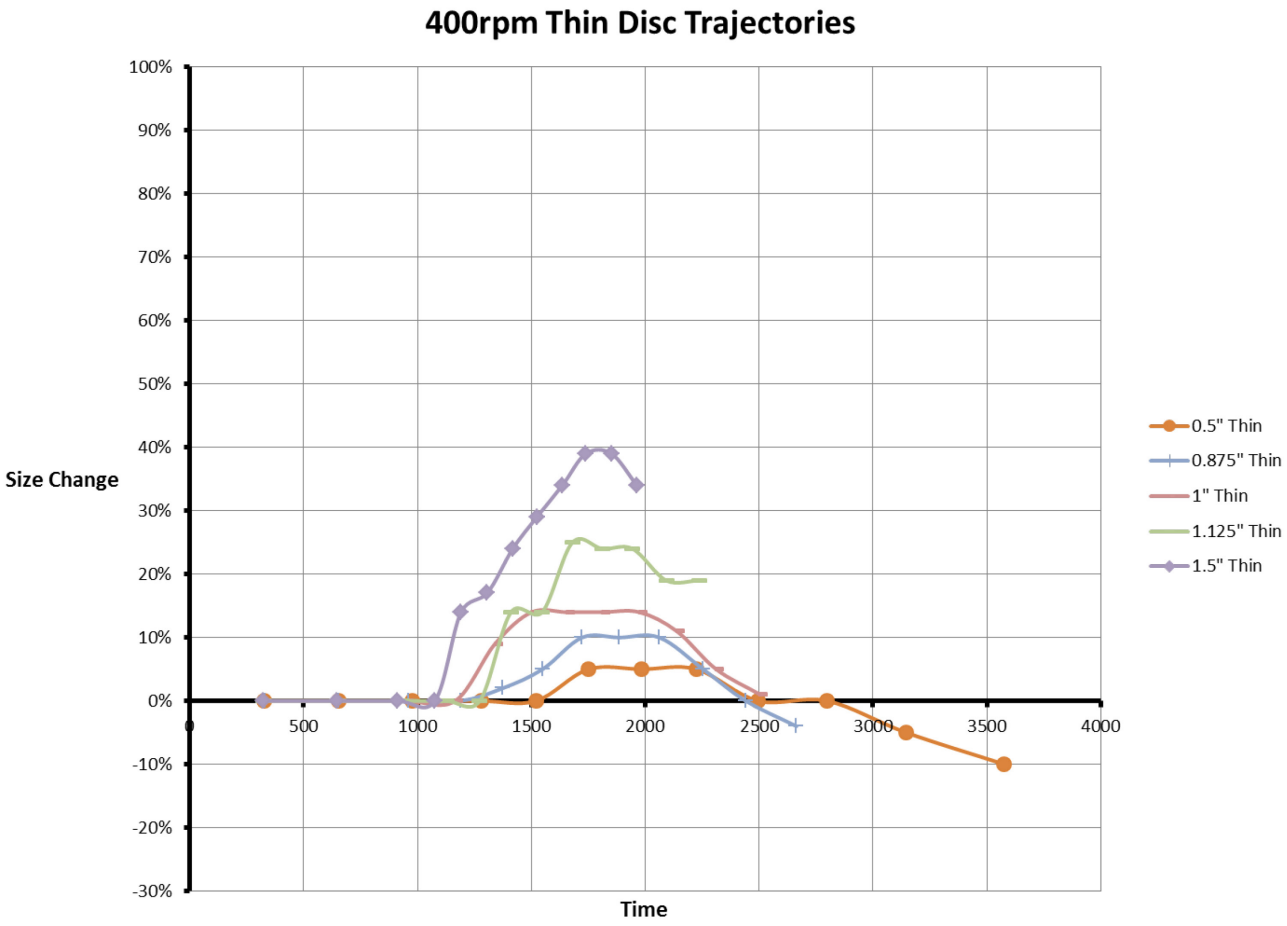

Figure C32. Size change data for 1/16" thick particles in tests conducted with eccentric type ECS at 400rpm

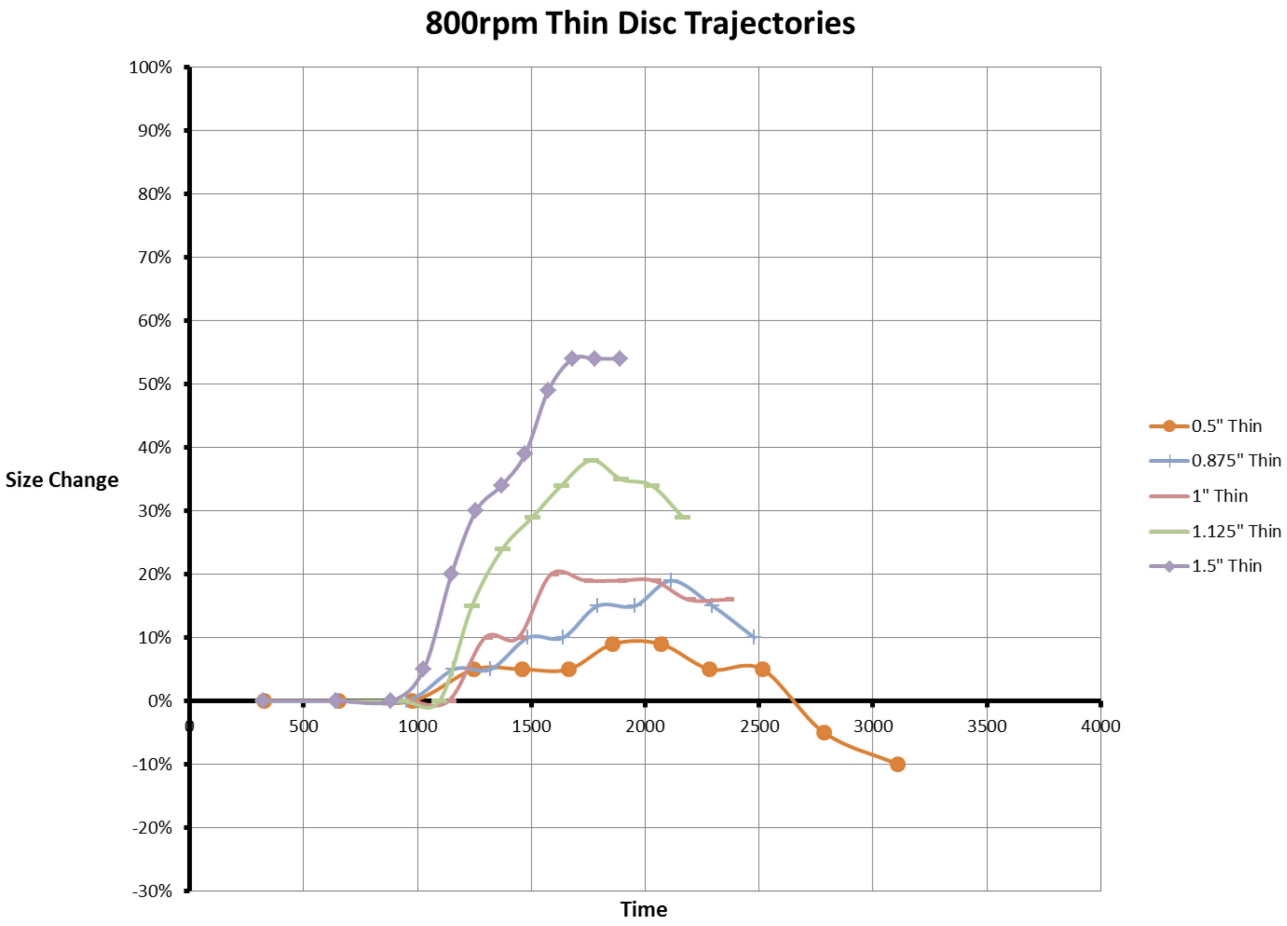

Figure C33. Size change data for 1/16" thick particles in tests conducted with eccentric type ECS at 800rpm

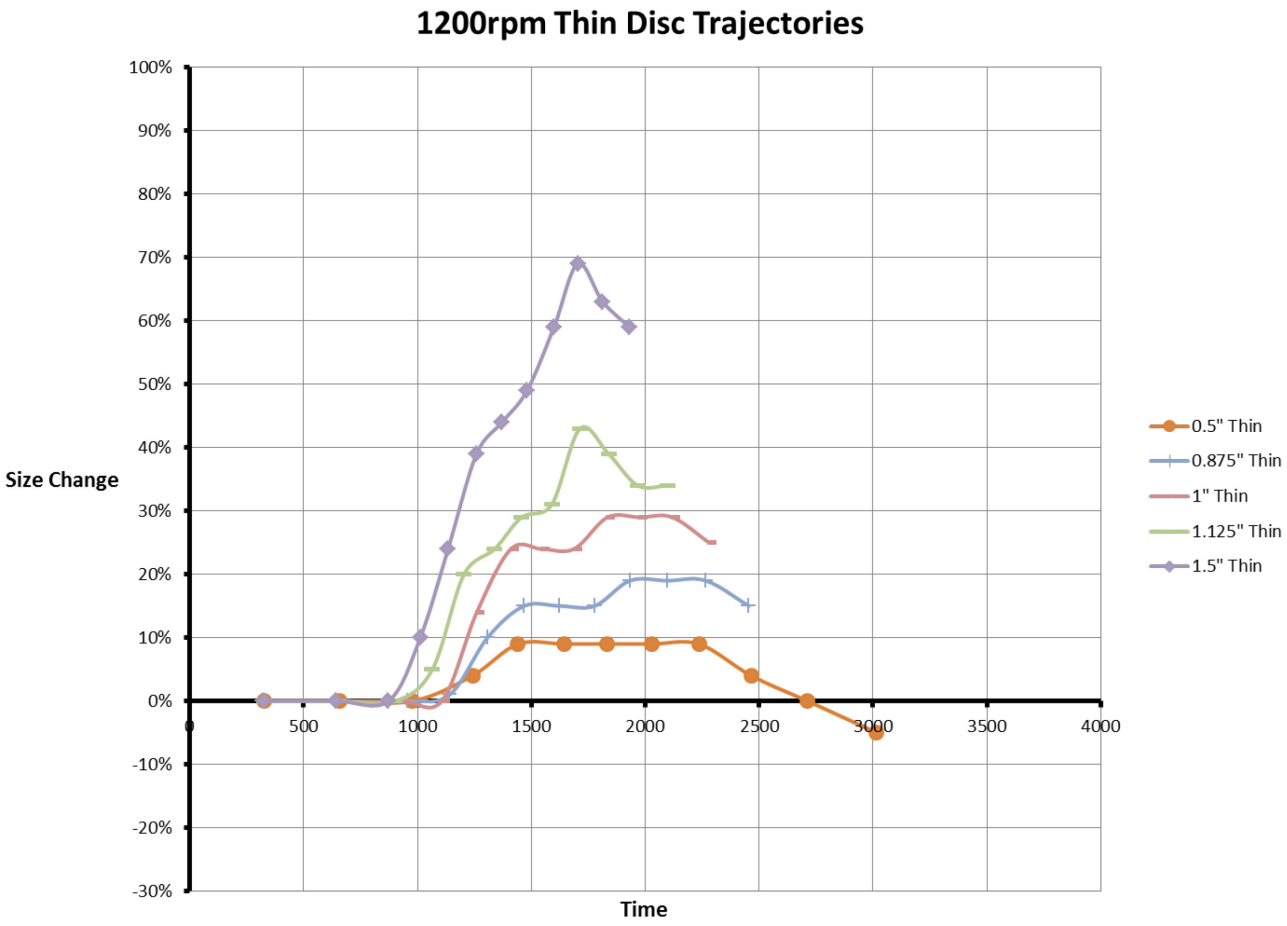

Figure C34. Size change data for 1/16" thick particles in tests conducted with eccentric type ECS at 1200rpm

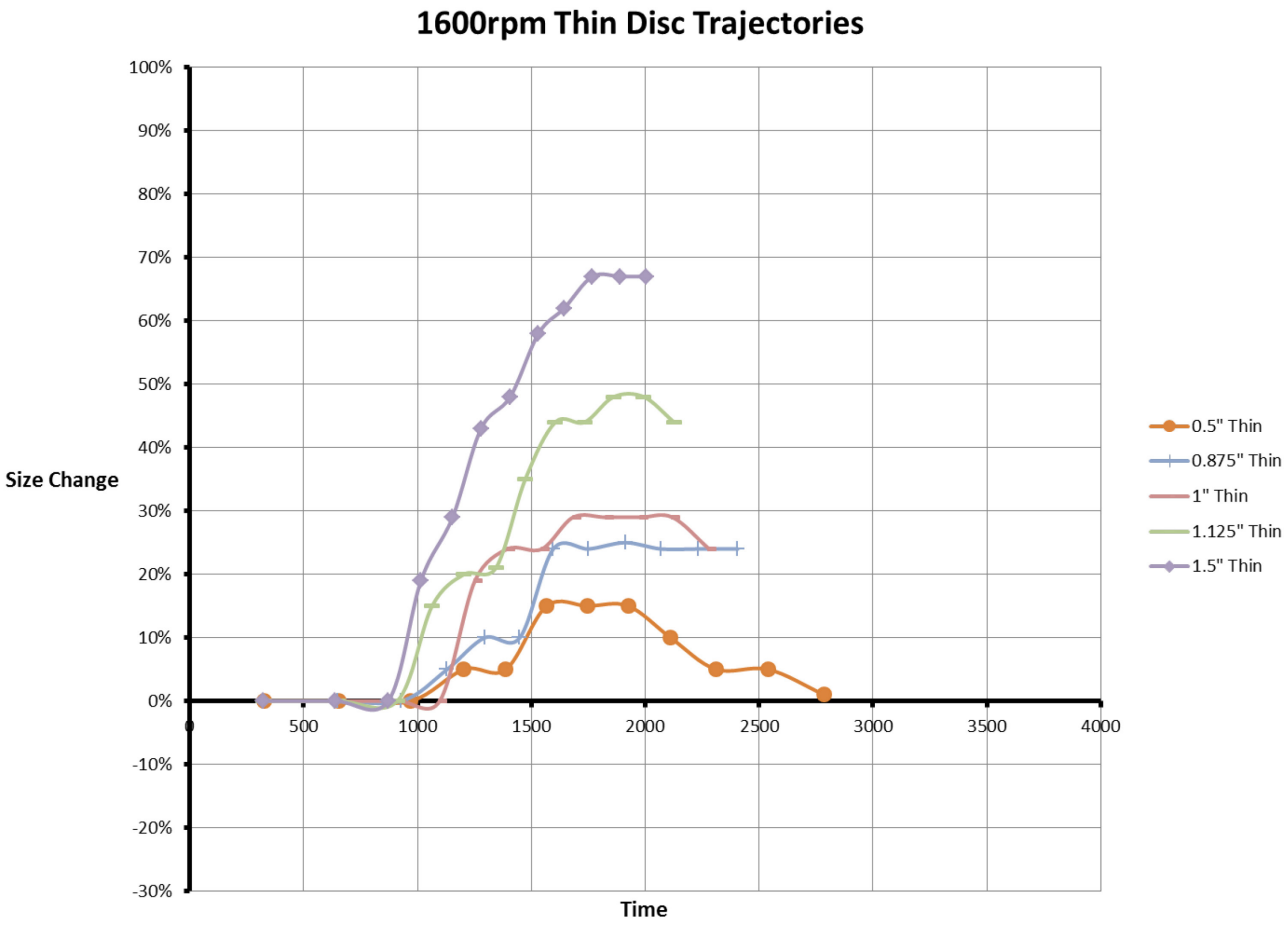

Figure C35. Size change data for 1/16" thick particles in tests conducted with eccentric type ECS at 1600rpm

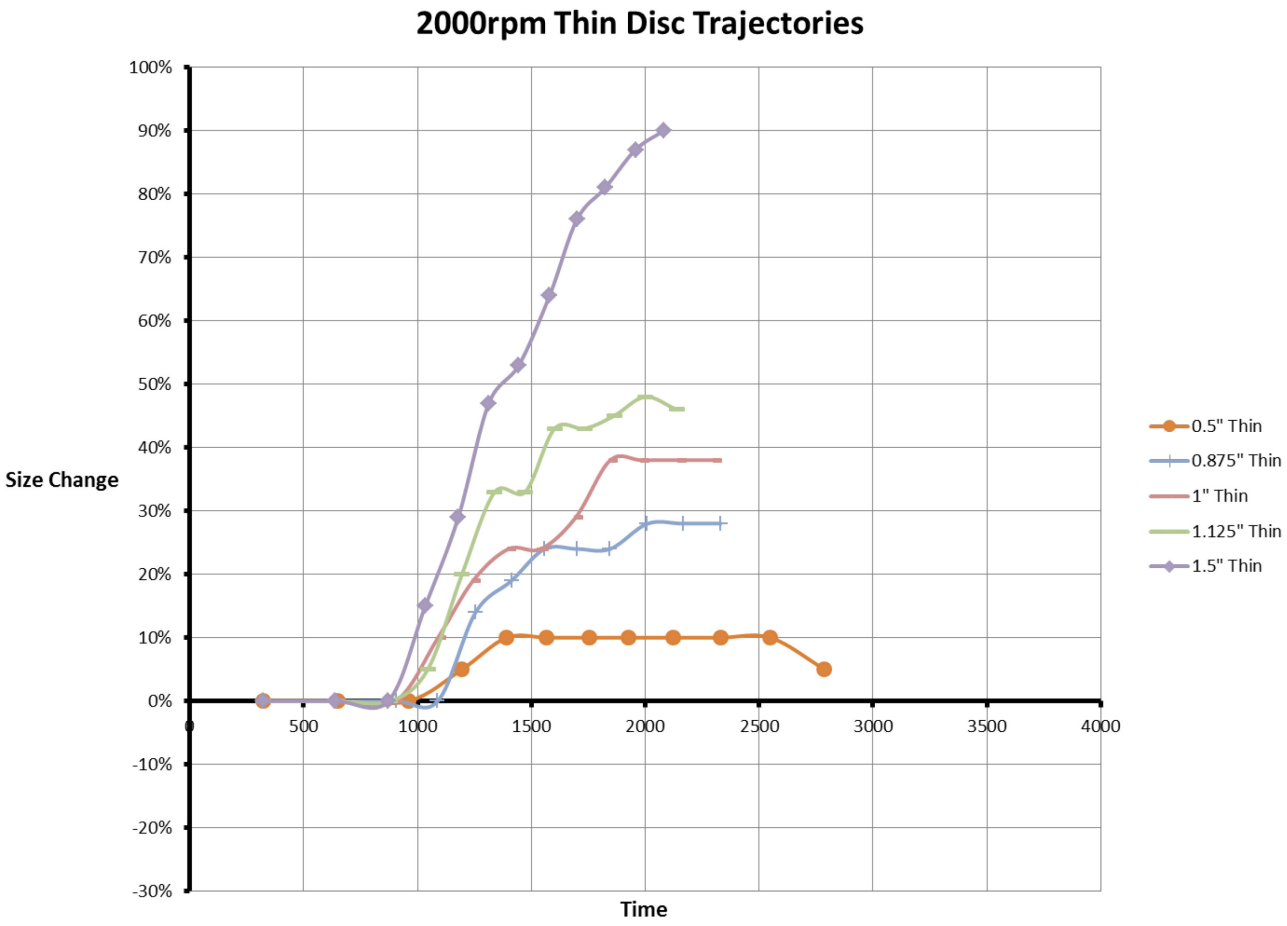

Figure C36. Size change data for 1/16" thick particles in tests conducted with eccentric type ECS at 2000rpm

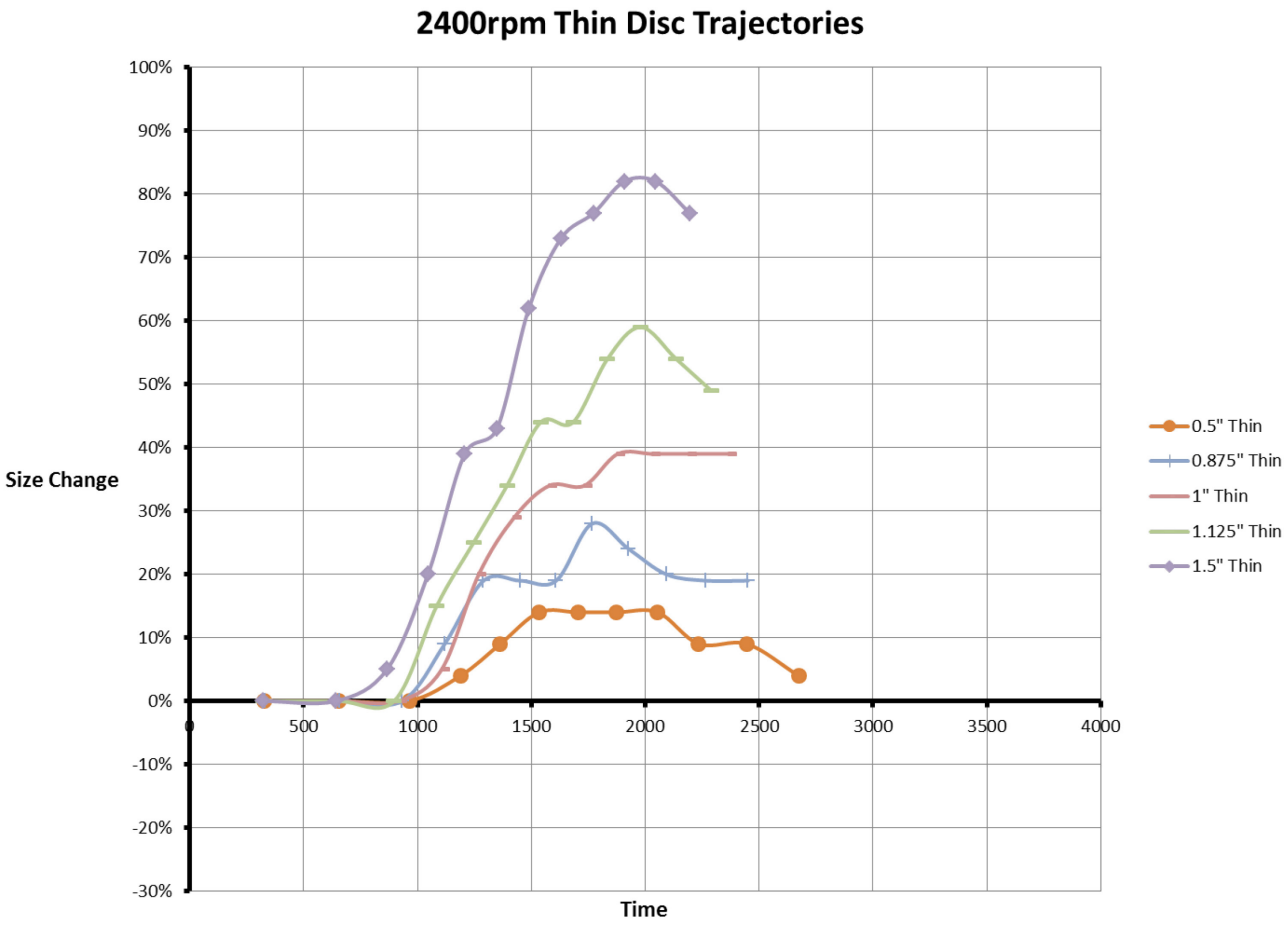

Figure C37. Size change data for 1/16" thick particles in tests conducted with eccentric type ECS at 2400rpm

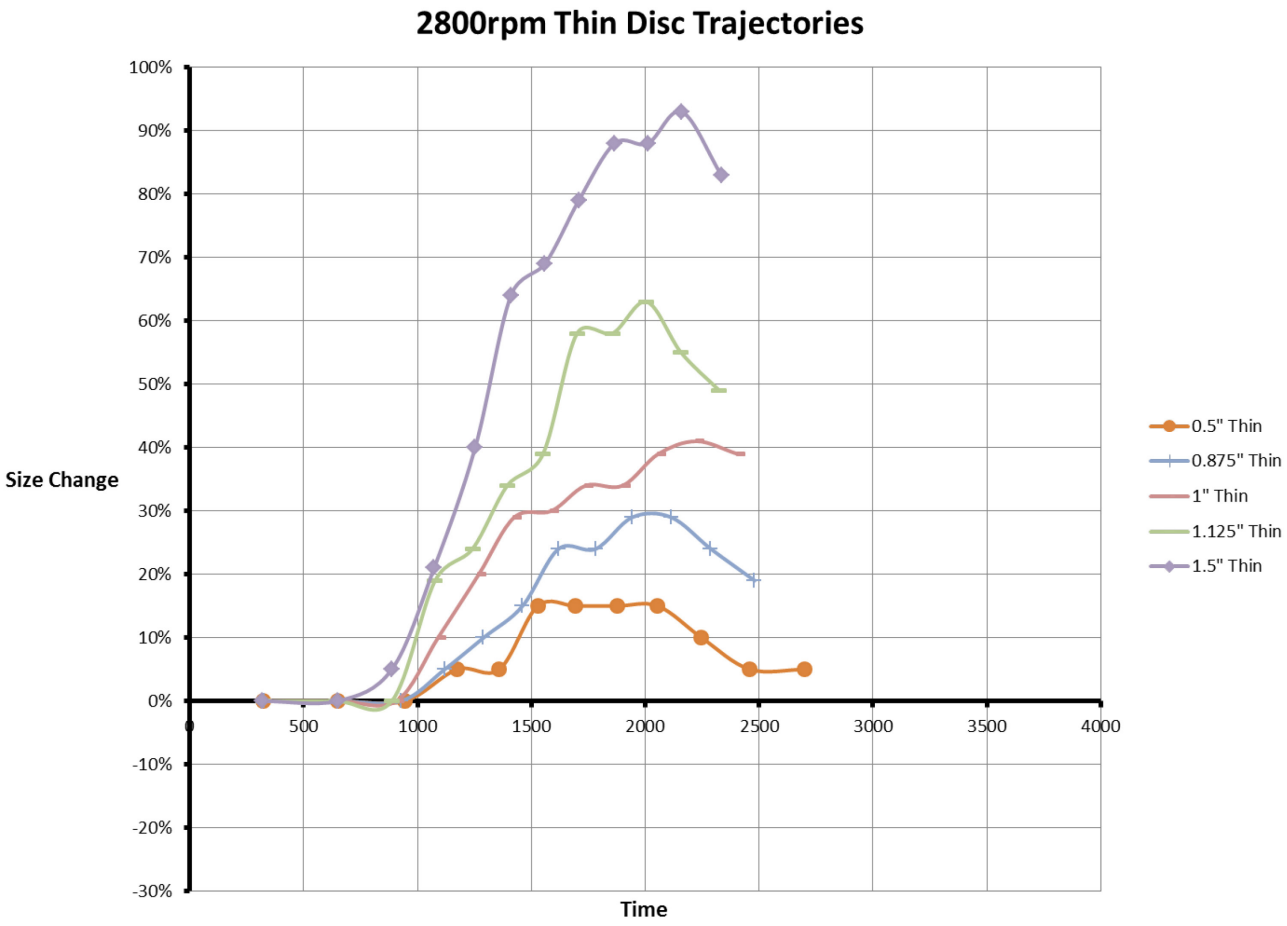

Figure C38. Size change data for 1/16" thick particles in tests conducted with eccentric type ECS at 2800rpm

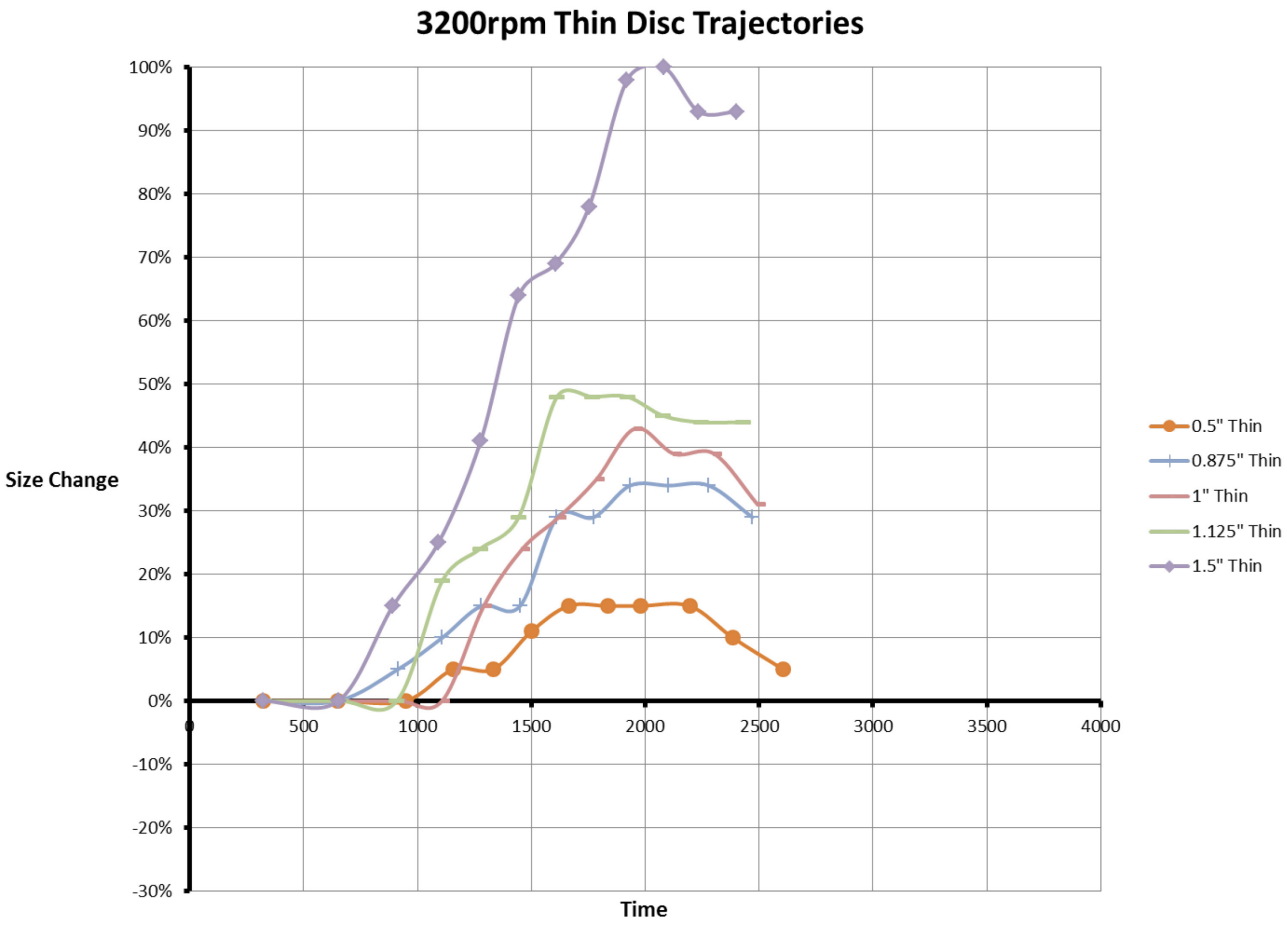

Figure C39. Size change data for 1/16" thick particles in tests conducted with eccentric type ECS at 3200rpm

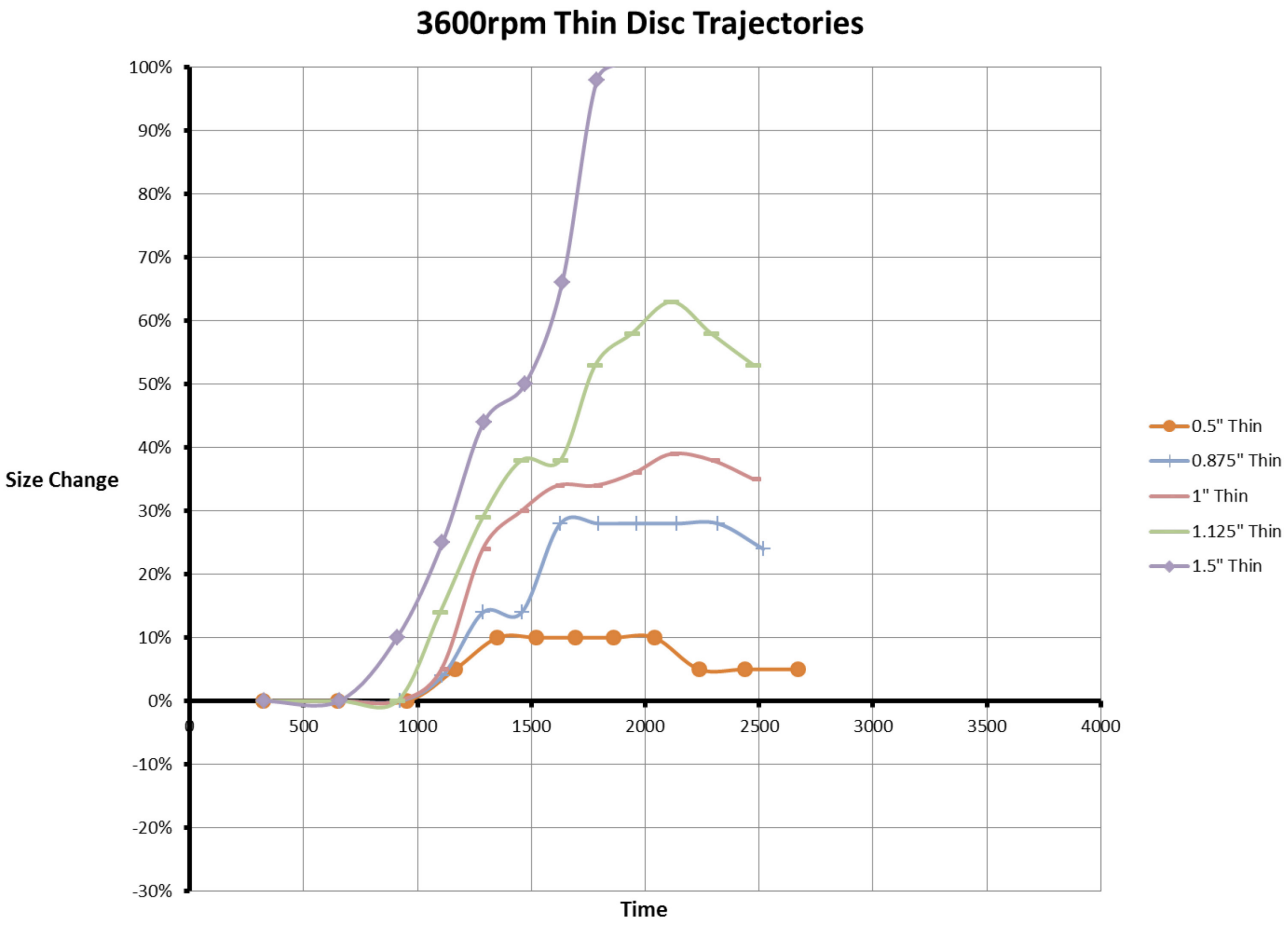

Figure C40. Size change data for 1/16" thick particles in tests conducted with eccentric type ECS at 3600rpm

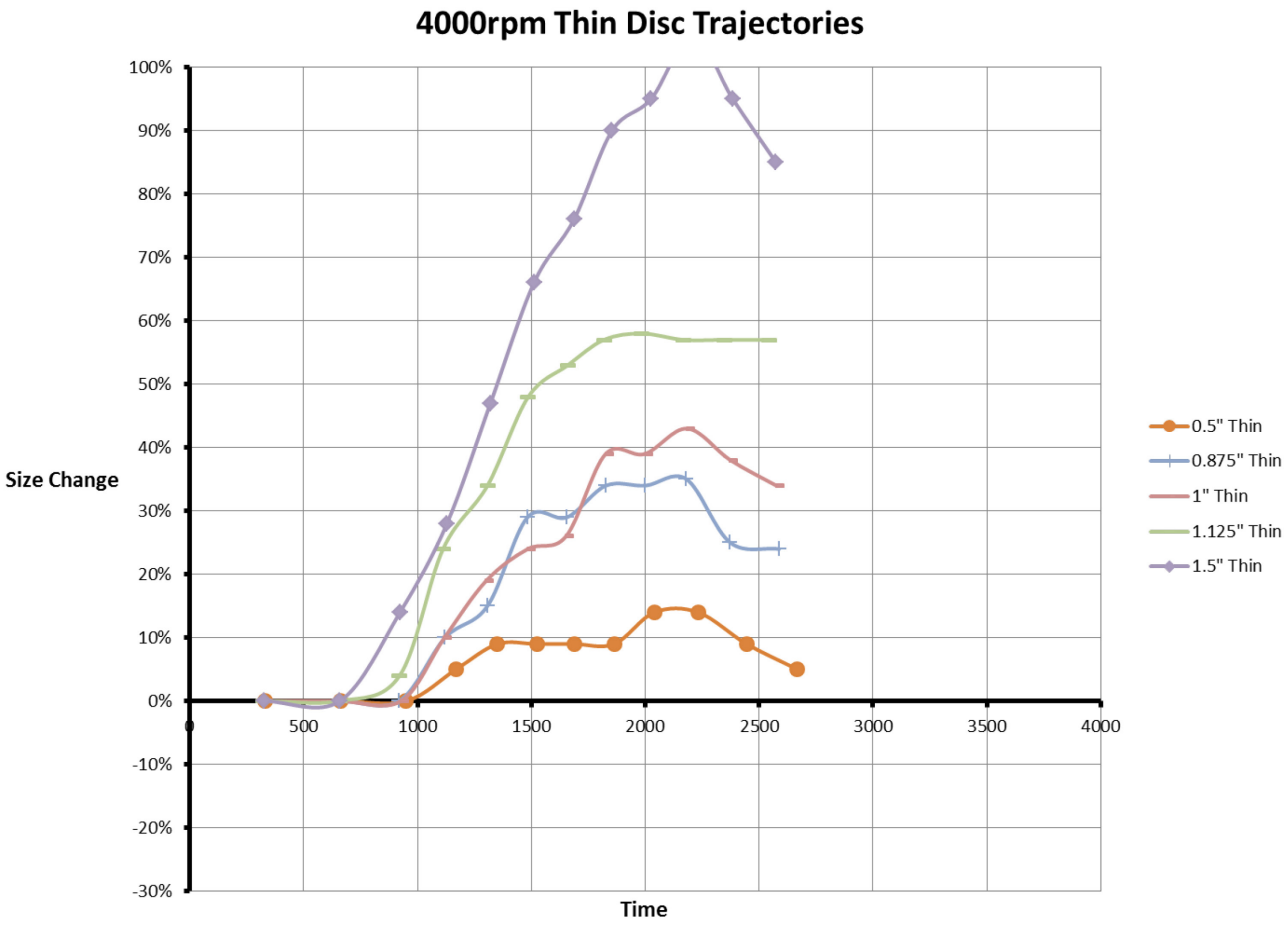

Figure C41. Size change data for 1/16" thick particles in tests conducted with eccentric type ECS at 4000rpm

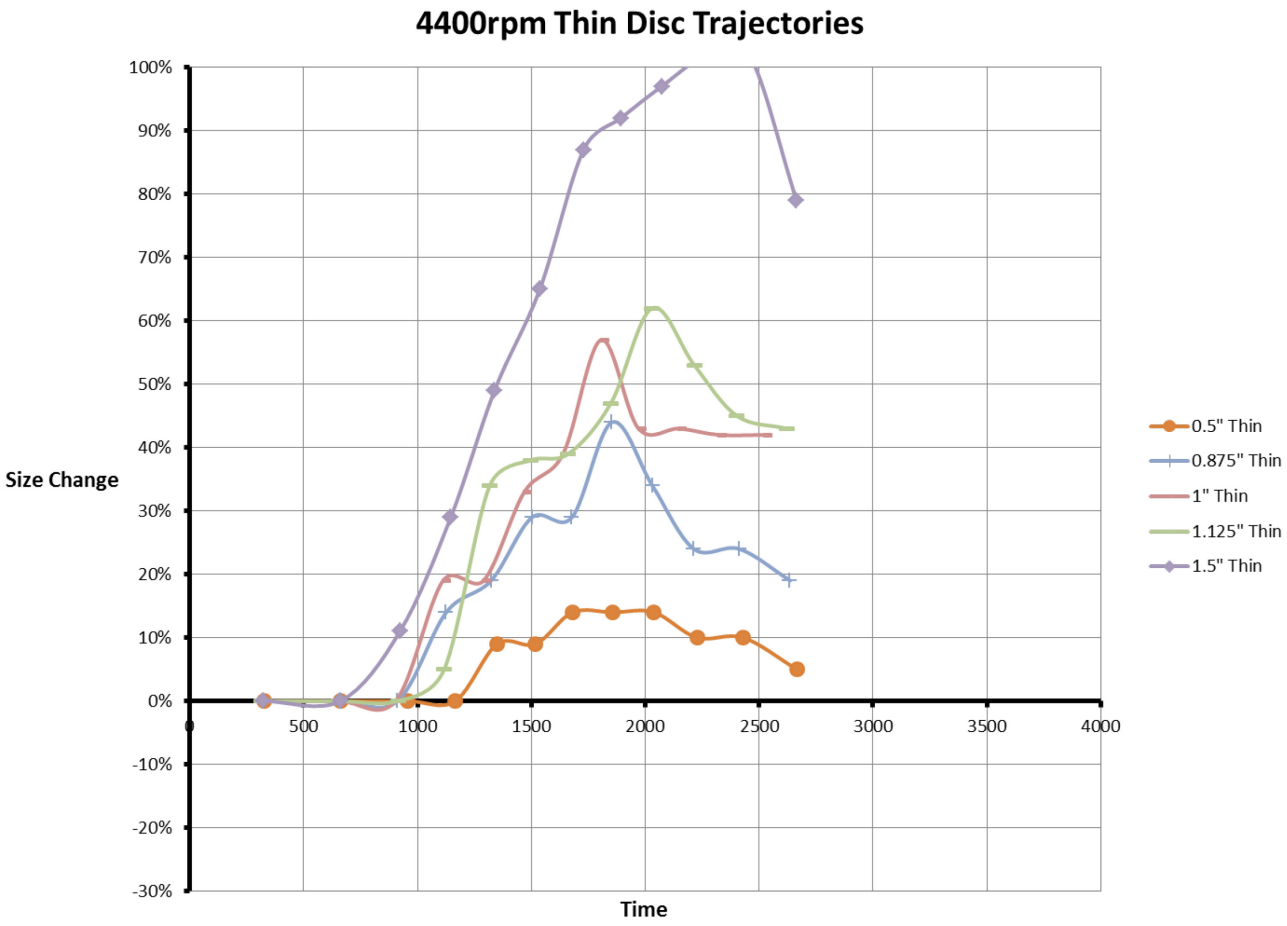

Figure C42. Size change data for 1/16" thick particles in tests conducted with eccentric type ECS at 4400rpm